4

Bench Scale

The investigation of the governing flow and transport processes and the quantification of relevant parameters of fractured porous rocks are often limited by the question as to what extent the parameters measured in the laboratory are applicable to other investigation scales. In order to investigate the effects of scale on pneumatic tomographical investigation techniques for flow and transport in fractured porous rock, cylindrical samples and laboratory block samples are recovered from the field and new experimental techniques are developed.

To bridge the gap between the experimental studies conducted on the core scale as described in Chapt. 3 and on the field block scale (Chapt. 5), on the one hand, cylindrical fractured sandstone cores with a diameter of 0.3 m are collected. To increase the support volume for the estimation of effective parameters without losing the geometrical boundary conditions with respect to the 0.1 m samples. On the other hand, larger sandstone blocks with sample volumes of ca. 0.2 and 0.7 m^3 are selected; these account for the geometrical boundary conditions of the field block scale but still allowing for laboratory experiments under fully controlled boundary conditions.

The description of the experimental studies conducted on the cylindrical samples and on the block samples including their preparartion are described separately for each sample size:

1. cylinders with a diameter of 0.3 m, and
2. laboratory blocks with a size of $90 \times 90 \times 80 \, \text{cm}^3$ and $60 \times 60 \times 60 \, \text{cm}^3$.

4.1 Preparation of Fracture Porous Bench Scale Samples for Conducting Flow and Transport Experiments

C.I. McDermott, C. Leven, B. Sinclair, M. Sauter, P. Dietrich

There are no established techniques for recovering either cylindrical or block shaped bench scale samples. This section is divided into two parts, the first

covering the recovery and preparation of the cylindrical samples, the second the recovery and preparation of the block samples.

The greatest problem with fractured rocks is that during sampling or preparation the fractures, natural planes of weakness, open up and the sample disintegrates before reaching the laboratory (e.g. Alexander *et al.* (1996); Baraka-Lokmane (2002a)). The problem is by no means new as demonstrated by the work of Wichter and Gudehus (1976) in the recovery of large scale fractured samples. More recently, a number of methods involving resin injection (Freig *et al.*, 1998) have been suggested, but the danger that the resin will impregnate the rock mass and alter the characteristics of the material being sampled remains. A further disadvantage is the sometimes complex preparation of the resin itself under difficult field conditions.

4.1.1 Recovery and Preparation of the Cylindrical Bench Scale Samples

In this section, a method for collecting, preparing and describing very closely spaced fractured samples (¡ 20 mm to 60 mm spacing) is presented where no hardening material is required. This method is used to recover ten relatively undisturbed extremely closely to very closely fractured samples as well as three samples where the fracturing is more discrete. All of the samples are cylindrical with a smooth top and bottom, have a diameter of 30 cm and a length of 30 to 40 cm. From the samples retrieved, five contain clay filled fractures with some open fractures, five contain sand filled fractures, and three samples contain open fracture systems. An example of each of the three types of sample is presented in Fig. 4.1. The samples are ideal for a number of different laboratory applications, including the triaxial investigation of the strength of the fracture network and, in this case, pneumatic tomographical investigation of the flow and transport parameters.
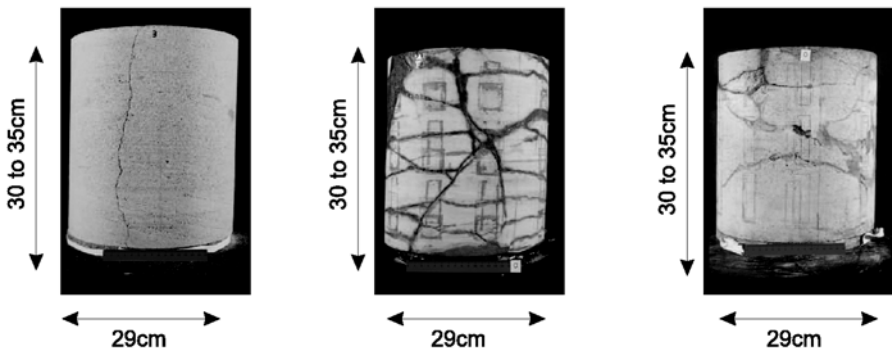

Fig. 4.1. Samples with open (a), sand-filled (b) and clay-filled (c) fracture systems (McDermott *et al.*, 2003b).

4.1.1.1 Sample Size

The selection of the size of the sample is very important. Samples must be large enough so that the fracture network can be investigated, but not too large so that handling in the field or laboratory becomes impossible with conventional techniques. A sample diameter of 30 cm and a length of 30 cm and 40 cm are chosen to fulfil the sampling, field and laboratory requirements. Samples of this size weigh approximately 40 kg and can generally be handled without mechanical assistance. A larger diameter of 40 cm and length of 40 to 50 cm, although technically feasible and containing a much larger selection of the fracture network, would lead to samples in excess of 100 kg, rendering handling difficult.
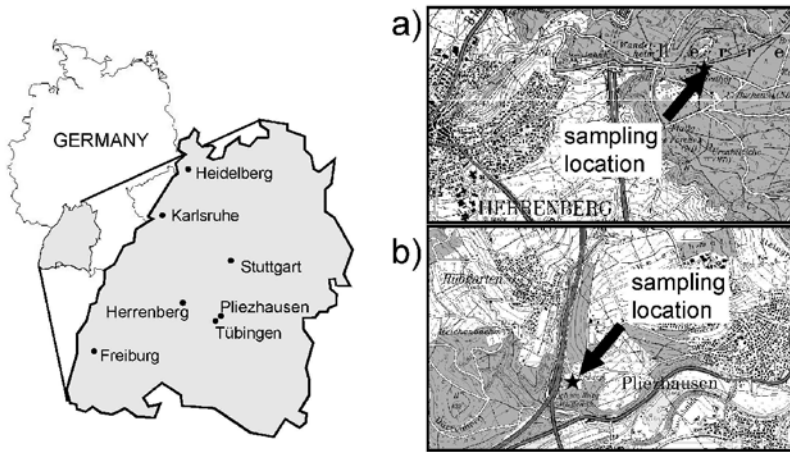
4.1.1.2 Sampling Location

The sampling locations are chosen on the basis of the experimental requirements and, to some degree, the access to the site. Two different sampling locations, illustrated in Fig. 4.2, are chosen, one in an active quarry (*Pliezhausen*) and one in the vicinity of an abandoned quarry (*Herrenberg*). The criteria for selecting the sampling material are primarily geological, those for the selection of the location are logistic. The quarry faces provide an excellent outcrop and hence an overview of the material to be sampled. In the case of the location *Pliezhausen*, all the samples are taken from material that is freshly exposed. In the case of the sampling location *Herrenberg*, it is necessary to expose a new surface behind the quarry face, as the face itself is a protected area. Samples are taken some five to ten meters behind the face edge of the quarry, and the ground reinstated once work is completed.

All the samples are taken from the upper Triassic *Stubensandstein* formation, a fractured arkose sandstone. In *Pliezhausen* five samples are taken from the forth *Stubensandstein* (Hornung, 1998) containing two types of fracture systems, a dominant closely spaced fracture system predominantly clay filled and a secondary widely spaced open fracture system with a apertures of approximately 1 mm. Three further samples are taken in *Pliezhausen* from the third *Stubensandstein* (Hornung, 1998), containing a number of discrete and interlinked open fractures. Five samples are collected from the second *Stubensandstein* (Hornung, 1998) in the vicinity of *Herrenberg*, containing fractures which are extremely closely spaced and sand filled.

4.1.1.3 Sampling Considerations, Sample Removal and Preparation

The sampling system is a point-sampling system one, and is designed as far as possible to fulfil the following criteria:

1. Random location and hence flexibility regarding the location of sampling,

Fig. 4.2. Location of recovery of cylindrical samples: (a) Sampling location *Herrenberg* and (b) *Pliezhausen* (after McDermott *et al.* (2003b)).

2. preservation of in-situ conditions,
3. repeatability,
4. efficiency,
5. fulfilment of later experimental requirements:
   - samples to contain a fracture network, not just discrete individual fractures,
   - samples to be geometrically cylindrical with smooth surfaces, a diameter of 30 cm and a length of 30 to 40 cm.

There are Four main technical problems:

- *drilling of the sample:* the main consideration is how to ensure that there is no washout of the fractures caused by drilling flux;
- *sample recovery:* maintaining the sample and fracture network;
- *preparation of the sample for experimental use:* maintaining the undisturbed nature of the sample and fracture system;
- *sample description:* deriving a three-dimensional impression of the fracture network.

It is clear that some sort of support mechanism for maintaining the stability of the sample is necessary due to the closeness of the fractures to one another. This support mechanism can not be removed from the fractured sample until immediately prior to the experimental investigation. It has to be applied directly after drilling and left in place during the recovery, preparation and description of the sample.

In principle, the support mechanism chosen is a transparent plastic sheath, heated and inserted into the drilling, thereby encompassing the sam-

ple. The sheath then cools and contracts around the sample, exerting a limited stabilizing pressure on the sample.

In practice, the sheath comprises 3 mm thick PVC plastic that has to be cut and glued together in such a manner that its internal radius is some 5 mm less than the external radius of the drilled sample. To form the sheath, the ends of the PVC sheet are bevelled and a low-viscosity adhesive with high initial surface tension is used to join the two ends of the plastic (Fig. 4.3). After the ends of the PVC sheet are joined, the properties of the adhesive allows injection of the adhesive into areas of the joint where bonding has not occurred, ensuring an almost perfect joint. In the field, the sheath is warmed in a water bath to a temperature of over 70°C, whereupon it expands to a circumference slightly larger than the drilled sample.
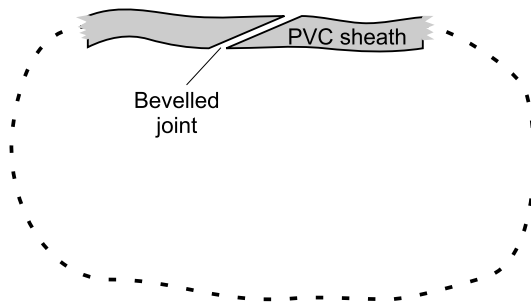

Fig. 4.3. Joining of the PVC sheet to form the protective sheath (McDermott *et al.*, 2003b).

The sampling procedure can be divided into five stages; these are described below and illustrated in Fig. 4.4.

Stage 1: Location The area of porous fractured rock to be sampled is selected and prepared in that any extraneous material is removed until a relatively stable and consistent rock surface is uncovered. Should instauration of the sampling area be necessary once work is completed, as in the case of the *Herrenberg* samples, care is taken to ensure that the extraneous material is removed and stored separately in layers for replacement. Excavated material is stored on a sheet thus protecting the ground surface. The cleared area must have a width of at least 1m to allow for access during sample recovery. The clearance can be undertaken by hand, or by an excavator.

Stage 2: Drilling A portable electric drilling machine, able to drill cores in rock of up to a diameter of 400 mm, is anchored on the prepared surface with the chemical plugs or typical concrete anchoring plugs. The cores are drilled using a water cooled diamond bit with sufficient but not excessive water flux. The pressure of the flush is kept minimal; generally, a head of the order of 1 m is enough to ensure that the drilling barrel is lubricated and that the material that has been loosened as a result of the drill bit action is washed

out. The drill flush is applied to the top of the sample and the cuttings (sand washed out) are drawn out on the outside of the drill bit (Fig. 4.5). Given the low hydraulic gradient in the drill flush and the approximate hydrostatic conditions within the drill head during drilling, there is very little outwash of the fractures.

Drilling must be precise and requires the drill bit to be stabilized, particularly for the first cut. In practice, this involves stabilizing the drill head with some heavy weight until the first cut has been made and the drilling barrel rotates smoothly. To recover the bench scale samples, a drill barrel with an external diameter of 300 mm and a cut width of 5 mm is used. Once a sample has been drilled to a depth of approximately 50 cm the drill barrel is removed and the sample, with a diameter of 290 mm, is left in place. During removal of the drill barrel, care is taken to ensure no suction effect is generated inside the barrel. In practice, this means ensuring that the barrel is disconnected from the drill, leaving the opening where the drill flush enters the barrel free, and the drill barrel is removed by hand.

Stage 3: Protection A pre-cut, transparent, 3mm-thick PVC cylindrical membrane is then inserted into the 5mm cut left by the drill (Fig. 4.6). This membrane, prepared before the sampling, has an internal circumference some 5mm less than the external radius of the drilled sample. The membrane is heated in a water bath to a temperature of 70°C to 90°C, causing it to expand, so that it fits over the sample. Once in place the membrane cools and returns to its original size, exerting a stabilizing pressure on the sample and isolating the sample from the surrounding rock.

Stage 4: Removal After the required number of samples has been drilled and protected, the material surrounding the samples is removed with great care by hand or mechanically to at least the depth of the samples. Once the samples are fully exposed, the PVC membrane is pressed radially onto the sample with the use of metal supporting rings. These rings are in a number of positions along the sample, including the top and bottom, thus providing further stability. Care is taken at this stage to avoid applying excess radial pressure to sensitive areas of the sample, such as soft weathered fracture zones. The exposed top of the sample is covered with a thin plastic sheet, followed by a hardening foam which moulds itself to the sample top. Once the foam has obtained some stability, the upper surface is covered with a pre-cut wooden lid, which is fixed in position using tape, and the protective sheath cut flush to the lid. (Fig. 4.7)

After the foam has hardened the sample can be removed from the host rock, using the natural fracture system. This provides a plane of weakness across which the sample can be broken away from the rock. Should the sample be firmly attached to the host rock, a chisel is used to fracture the material artificially at a predetermined position. Finally, the sample is lifted from its position, placed upside down on its lid, and further wrapped with waterproof plastic to ensure that the field moisture content is maintained as far as

possible. In addition, if further support and protection are considered neces-
sary, it can easily be done at this stage.

Stage 5: Cutting to fit cell For later use in the experimentation cell the sam-
ples must be cylindrical and have smooth bottom and top surfaces (McDer-
mott *et al.*, 1998). To achieve this, the samples are cut with a large circular
saw, leaving samples with a length at least as large as the diameter of the
sample (Fig. 4.8). Prior to cutting, the samples are further supported using
metal rings ensuring that minimum damage occurs during cutting. The ex-
tra supporting rings are positioned as close to the proposed cutting surfaces
as possible. This exerts a radial pressure inwards at the cutting position and
reduces the danger that the blade used for cutting will remove any mate-
rial from the sample. Once cut, the samples are immediately repacked and
protected before transport to the laboratory. Material cut from the samples is
retained for other tests, e.g. determination of porosity, specific gravity, etc.

4.1.1.4 Repair

In a few instances, small parts of the samples are lost during the cutting pro-
cess. As a cylindrical sample is necessary for the later experimental proce-
dure, the missing material is replaced with a moulded plastic element, en-
suring that the geometry of the sample is maintained.

4.1.1.5 Description of the Fracture System

The fracture description of the samples is very important for the future ex-
perimental investigation and for the development of modeling techniques to
analyze the results. To describe the fractures and other important character-
istics of the samples, a transparent plastic sheet is wrapped around the sam-
ples and significant features on the sample surfaces are drawn onto the plas-
tic. Recording the fracture profile may be carried out whilst the PVC sheath
is protecting the cylindrical samples or, if the sample is considered stable
enough, without protection. The orientation of the samples is recorded in the
field so that the direction north is given. The fracture record of the sample
is then digitized, allowing a three-dimensional reconstruction of the fracture
network from the surface traces. Where possible, the opening widths of the
fractures are recorded for use in discrete modeling approaches. An example
of the digitized records is presented in Fig. 4.9. The later experimental inves-
tigation techniques are then linked to the location of the fractures within the
sample.

4.1.2 Recovery and Preparation of the Block Samples

In the literature,only a few successful attempts to retrieve large scale labo-
ratory samples are reported, including a granite block by Vandergraaf *et al.*

(1997) and a welded tuff block by Tidwell and Wilson (1997). The former was prepared to investigate one fracture plane and latter for examining flow along natural bedding planes. However, as far as the authors are aware, no highly fractured porous sandstone blocks have been recovered because of the risk of sample disintegration due to its weakened nature and logistic problems.

4.1.2.1 Site Location

The two block samples are chosen on the basis of the following criteria:

- $90 \times 90 \times 80 \, cm^3$-block: closely fractured with significant fracture apertures,
- $60 \times 60 \times 60 \, cm^3$-block: homogeneously distributed fissures with small apertures.

They are taken from the third *Stubensandstein*-formation (Hornung, 1998) adjacent to the test site used for the investigation of a large scale in-situ field block 5 in an active quarry (Fig. 4.10).

4.1.2.2 Sample Removal

Several large scale blocks ($2 \, m \times 1.5 \, m \times 2 \, m$) are removed by a quarrying company from the third *Stubensandstein* formation. These blocks are ideal for experiments and for developing the experimental techniques.

Once the blocks are selected, it is necessary to cut them to get regular sides for easier experimental and modeling work. However, because of the risk of disintegration, it is only possible to cut the $90 \times 90 \times 80 \, cm^3$-block with two parallel faces. The instability of the block due to its fractured nature prevented further cuts leaving dimensions of $90 \times 90 \times 80 \, cm^3$.

Because the $60 \times 60 \times 60 \, cm^3$-block is much more compact, it was possible to cut it to an exact cubical shape with side lengths of 60 cm.

Once cut, the block samples are placed in a heated room for thorough drying. A special extraction system has also been constructed to expedite the drying process (Fig. 4.11).

4.1.2.3 Sample Description

This section describes the physical characteristics of the matrix and the fracture network of the block samples.

Sandstone matrix

Common laboratory experiments (e.g. helium pycnometer and gas permeameter) are used to determine the physical parameters of the porous sandstone matrix of the blocks. Typical values for the third *Stubensandstein*-formation are summarized in Table 4.1.

Table 4.1. Typical parameters of the upper *Stubensandstein* formation ("km4os3").

Specific gravity	ca. 2.7	g/cm^3
Porosity	10 - 25	%
Hydraulic conductivity	$5 \cdot 10^{-8}$ - $1.5 \cdot 10^{-5}$	m s^{-1}
CaCO$_3$ content	ca. 7	%
C$_{org}$ content	ca. 0.4	%
Saturation from humid air	ca. 12	%
Dominant grain sizes:		
clay	ca. 1 - 5	μm
quartz	ca. 100 - 500	μm
Dominant pore size	ca. 0.1 - 1	μm
Macro pores ($> 1\,\mu$m)	ca. 20	%
Cement of matrix	kaolinit	

The sandstone matrix of both blocks can be described as a hard closely bedded laminated fine to medium sandstone. From a macroscopic point of view, the $90 \times 90 \times 80\,\text{cm}^3$-block comprises a more or less homogeneous matrix while the $60 \times 60 \times 60\,\text{cm}^3$-block shows several zones of more coarsely and more finely grained sandstone respectively (cf. Figs. 4.12 and 4.13).

Fracture network

To describe the fractures, any significant morphological profile and other important characteristics of the sample, a transparent polyethylene sheet was placed on the block samples and the surface features are drawn onto the sheet. The fracture record of the sample is then digitized, allowing for a three-dimensional reconstruction of the fracture network from the surface traces. The fracture apertures are also gauged using a caliper square and the type of filling is recorded (open, sand, clay-filled). An example of the digitized records of fracturing combined with a surface image of the block is presented in Fig. 4.12 for the $90 \times 90 \times 80\,\text{cm}^3$-block and in Fig. 4.13 for the $60 \times 60 \times 60\,\text{cm}^3$-block.

The fracture network of the $90 \times 90 \times 80\,\text{cm}^3$-block is dominated by a main fracture that intersects sides *I* and *III* at a right angle and has apertures up to 4 mm (in Fig. 4.12 marked with "fracture 1"). Another dominant fracture lies nearly horizontally (marked as "fracture 2") within the $90 \times 90 \times 80\,\text{cm}^3$-block.

The $60 \times 60 \times 60\,\text{cm}^3$-block comprises only one vertical fracture with an aperture of up to 1.75 mm. As is also evident from Fig. 4.13, further fissures are parallel to the bedding and are open to some extent and mostly clay-filled.

4.1.2.4 Sealing and Further Preparation of the Block Samples

For the two blocks, two different sealing techniques are applied, both based on epoxy resin. The sealing procedure is described for each block individually in the following sections.

Sealing the $90 \times 90 \times 80\,cm^3$-Block

The sealing jacket for the $90 \times 90 \times 80\,cm^3$-block is composed of a resin which had to be poured or painted onto the sample. The top side of the block is prepared and levelled to a flat surface in the field using hand tools. Before the block faces are coated with resin, a thin coating of silicon is applied to all visible fractures, ensuring that an impregnation of the fracture system is prevented. The resin is then poured onto the surface of the block in four or five successive coats until a minimum thickness of 5 mm is reached.

Once the upper surface of the block hardened, the block is rotated and placed upon a specially designed mobile platform (Fig. 4.14). Prior to rotation, the block is reinforced on all sides with metal tension bands, exerting an inward force on the block faces to stabilize any planes of weakness.

The following method is developed for rotating the block without causing any further fracturing: To turn the block, weighing some 1600 kg, and place it on the mobile platform, a front-loading fork-lift truck with tiltable prongs is used. This procedure is illustrated in Fig. 4.15. The block is attached to the prongs, using three material tension bands capable of withstanding 4 tonnes of tensile force. Once attached, the block is lifted and the prongs of the fork lift titled 90° so that the weight of the block is taken by the material bands. The block is then placed on a pallet and the material bands released. The procedure is repeated and the block placed on the mobile platform. Finally, the remaining block faces are coated with four to five coats of epoxy resin until again a minimum thickness of 5 mm is reached.

The technique developed to allow access to the block sample involves drilling holes in the resin coat and a thread cut directly into the resin. However, it is found that drilling dust is forced into the sandstone matrix and fractures. This can not be extracted and leads to the local sealing of the matrix and fractures (Fig. 4.16). In addition, dust coming out of the matrix and fractures over a period of time and entering the airtight connections renders them useless.

To solve this problem, a hole saw is used to extract a core of the same surface area as the required port area from the resin coat. The process of ensuring extraction of the resin coat rather than drilling ensures that the dust sealing described above is prevented. The resulting hole in the resin coat is then sealed with a plastic plug into which a thread is turned so that an airtight connection can be attached to this plug. The plug is inserted into the drilled hole but not allowed to rest on the sandstone, thus ensuring that there is a small air pocket between the sample surface and the plug. This

air pocket ensures that later injection through the airtight connection is dispersed over the whole port area and not restricted to specific points. Before the airtight connection is attached, a thread is cut in the underside of the connection to which a filter plug is attached. This ensures that any loose dust generated during the drilling of the port or existing in the matrix of the block sample does not interfere with the operation of the airtight connection. The airtight connection is then mounted in the plastic plug and sealed using a sealing paste in the thread. In Fig. 4.17 the construction of the ports is shown; Fig.From Fig. 4.18 the exact location of the ports with respect to their position on the blcok surface can be seen.

However, it is found that the fractures running close and parallel to the surface of the block provide a large plane of action for the force resulting from the internal pressure on the block, attempting to push the resin from the block. During a test phase, a pressure of approximately 1.2 bar was applied to the block and led to failure of the base of the block. The entire base had to be prepared again and loose material removed. In order to counteract this force across the fracture planes and provide the resin with some support, it was necessary to install a number of supporting anchors normal to the fracture planes where this problem could arise.

Sealing the $60 \times 60 \times 60 \, cm^3$-Block

To circumvent problems resulting from insufficient coating support, a multi-layer approach is used for the sealing of the $60 \times 60 \times 60 \, cm^3$-block sample, as described in the following. However, because this procedure requires the successive and repeated rotation of the block sample, the procedure is only applicable for sample sizes for which common lifting gear can be used.

To rotate the block sample, the same principle is applied as described for the $90 \times 90 \times 80 \, cm^3$-block, except that a small lift is used.

Sealing the block sample comprises the following steps:

1. Attaching ports allowing access to the block faces (Fig. 4.20 (a): In contrast to the preparation of the $90 \times 90 \times 80 \, cm^3$-block, ports are attached to the block faces prior to sealing. For this purpose, special cylindrical aluminium plugs are constructed with an air pocket towards the block faces (Fig. 4.19). These plugs are attached with a sealing paste. Attaching the ports prior to sealing has the advantage that
   - the problem of drilling dust can be avoided, and
   - the ports are stabilized by the resin coat applied in the following steps.

2. Sealing fissure traces: as described for the $90 \times 90 \times 80 \, cm^3$-block, the traces of the fissures on the block faces are sealed with a thin coat of silicon, preventing impregnation along fissure planes.

3. First resin coating (Fig. 4.20 (b)): in the first resin-coating step, two layers of a thick epoxy resin with low viscosity are painted onto the block faces, giving the surface an airtight seal.

4. Contact coating: in this second resin-coating step, a thin layer of fiber-glass scraps suspended in highly viscous epoxy resin is applied. Because of the high specific surface area of the fiberglass scraps, this layer will ensure that the resin coat and the subsequent coats of fiberglass matting will adhere.

5. Coat of fiberglass matting (Fig. 4.20 (c)): In the next steps, the block is covered with two to three layers of fiberglass matting. Each layer has to be soaked in the highly viscous epoxy resin used in the step before. It is important to note that the individual mats should overlap the adjacent block faces by at least one third to ensure a high stability. The layers of fiberglass matting will make the block stable, allowing high pressurization.

6. Fiberglass plasticine coat (Fig. 4.20 (d)): in the final step, all the block faces are coated with a very thick fiberglass plasticine with an extremely low viscosity. This coat can be several centimeters thick and provides additional stability and also acts as a safety coating.

It is important to note that all steps that include the application of epoxy resin have to be carried out before the individual resin coatings harden, which usually takes - depending on the type of resin - approx. 30 to 60 minutes. To apply all the individual coats, the successive and repeated rotation of the block sample is necessary.

Because of this coating, pressures of more than 2 bars could be applied to the $60 \times 60 \times 60 \, cm^3$-block sample. Higher pressures are believed to be possible. However, it is also important to consider laboratory safety when working with pressurization above atmospheric pressure.

Controlling the hermetic seal

After the blocks were encased , it was necessary to prove they are hermetically sealed. This is done by pre-pressurizing the blocks to 0.5 to 1.0 bar above atmospheric pressure. Once the system has stabilized the air supply is cut off and the pressure in the blocks monitored using a manometer attached to one or more ports (Fig. 4.21 (a) and (b)).

If the pressure is found to fall with time, it can be assumed that the resin jacket or one of the connections are leaking. At times, it is necessary to submerge the block in water to find the leaks. This is done by rolling it onto a waterproof plastic sheet, then constructing a bath around it using flexible plastic walls (Fig. 4.21 (c)). The bath is then filled with water to cover the block (Fig. 4.21 (d)).
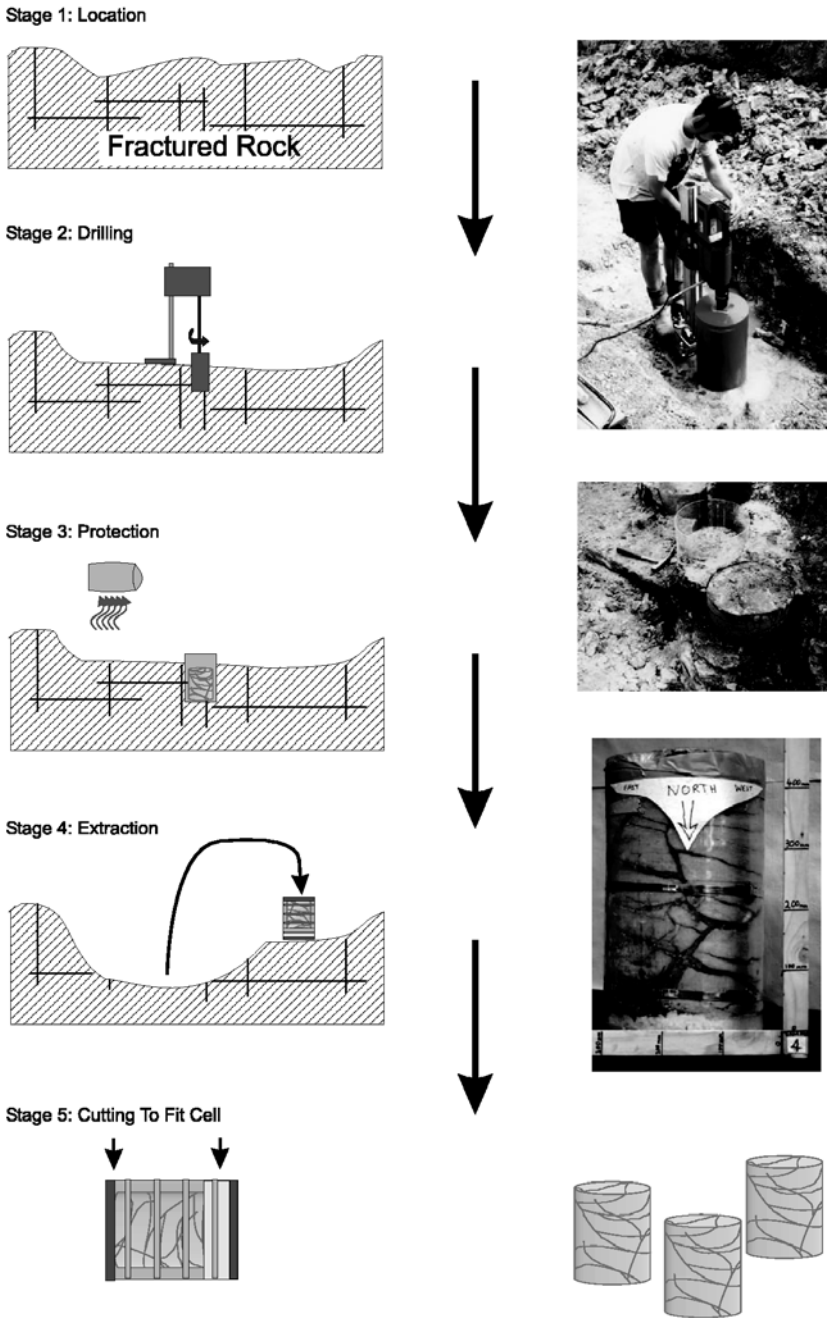
Fig. 4.4. Overview of the steps for sample recovery and preparation (after McDermott *et al.* (2003b)).
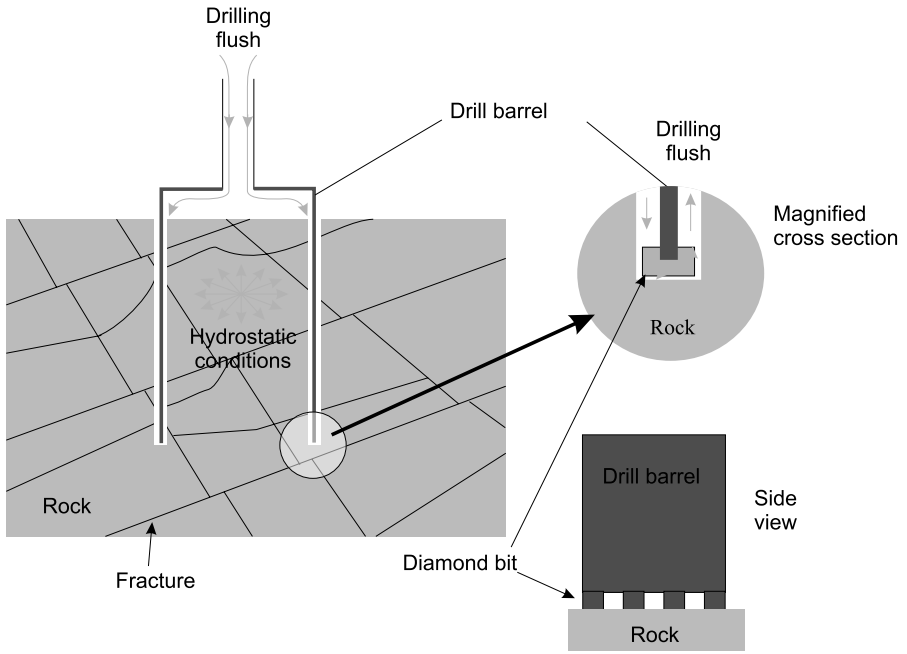
Fig. 4.5. Drilling and flush during the taking of a cylindrical sample (McDermott *et al.*, 2003b).
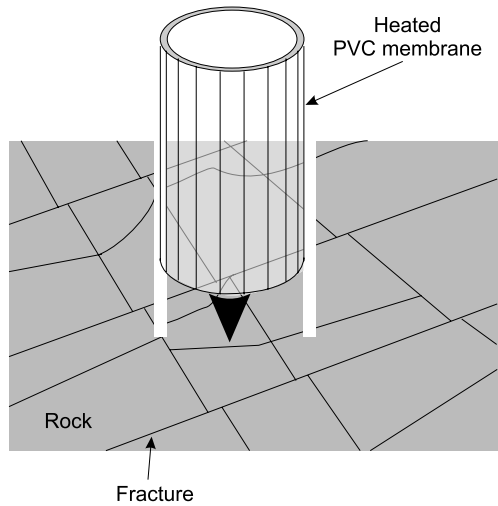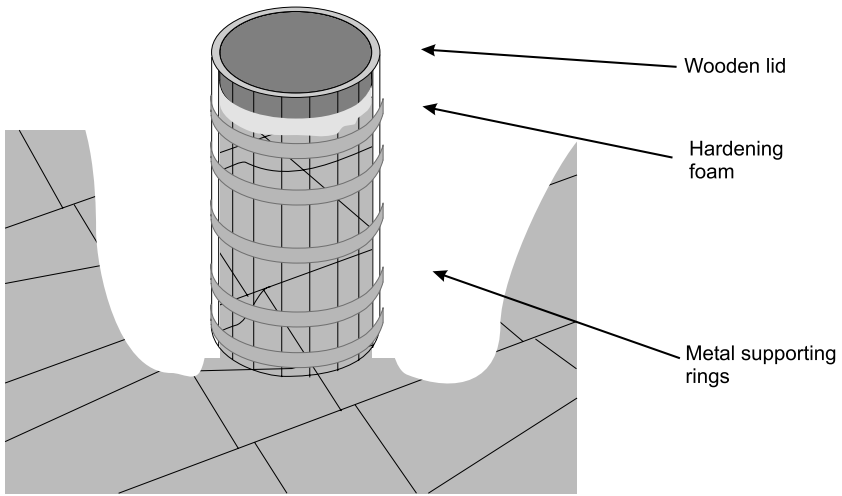

Fig. 4.6. Protection of cylindrical sample with a heated PVC membrane before the removal (McDermott *et al.*, 2003b).

Fig. 4.7. Protection, support and preparation of a cylindrical sample for extraction. The top surface of the sample is protected, then hardening foam is squirted on the top of the sample, a wooden lid is then pressed onto the foam. Once the foam has hardened the sheath is trimmed and taped to the wooden lid. Then the surrounding material is removed and the sample is further supported with metal rings (after McDermott *et al.* (2003b)).

Prior to cutting the samples are further supported
with metal rings adjacent to the indeded cut positions.
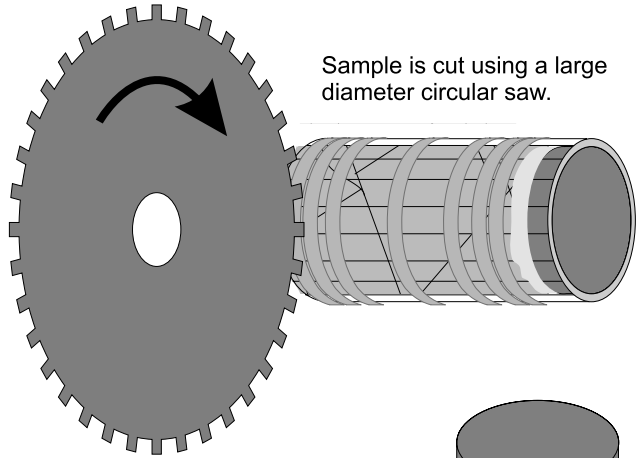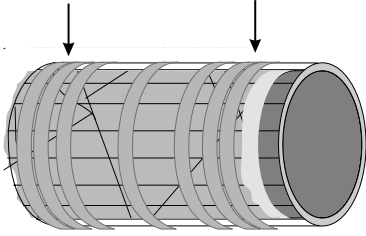
Sample is cut using a large
diameter circular saw.

Once cut the ends of the sample
are protected with plastic and
a second wooden lid, of
slightly larger radius than sample,
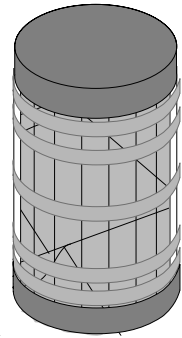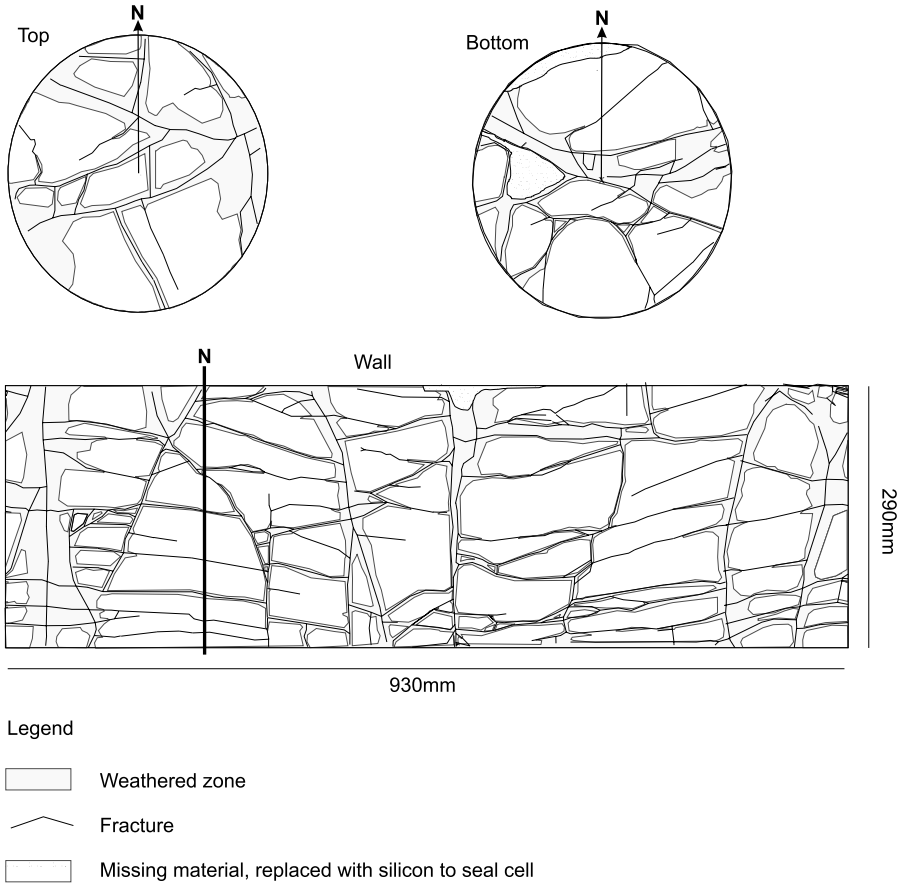flush with the protecting sheaf.

Fig. 4.8. Preparation of the cylindrical sample for laboratory investigation (McDermott *et al.*, 2003b).

Top

Bottom

Wall

290mm

930mm

Legend

Weathered zone

Fracture

Missing material, replaced with silicon to seal cell

Fig. 4.9. Digitized record of a sample investigated. Example of the nature of fracturing in a sample investigated (height of sample 290 mm, diameter of sample 286 mm) (McDermott *et al.*, 2003b).
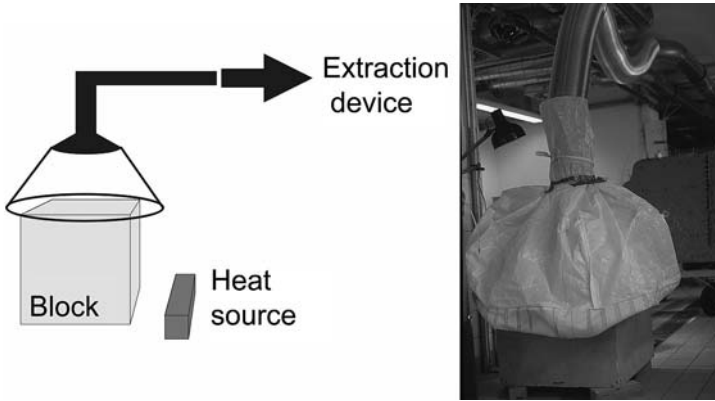

Fig. 4.10. Location of recovery of block sample.

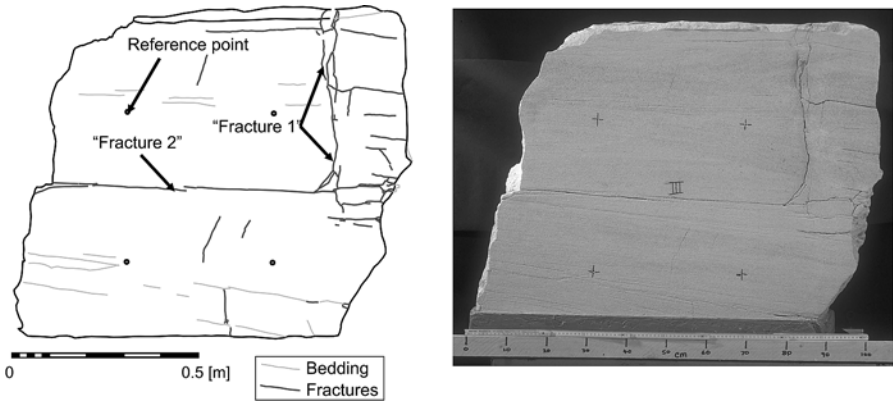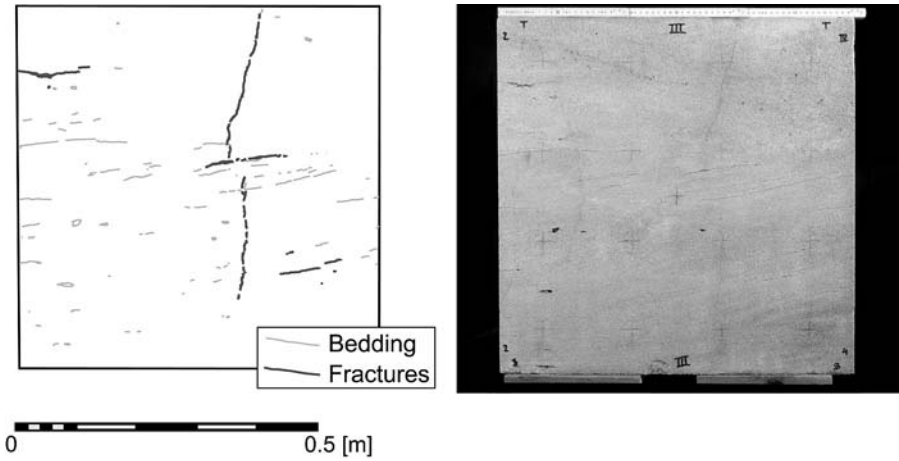**Fig. 4.11.** Extraction system for drying the block sample.

Fig. 4.12. Recording and digitizing the fracture and other important characteristics of the $90 \times 90 \times 80\,cm^3$-block. "Fracture 1" and "fracture 2" indicate the locations of dominant fractures within the block sample.

Fig. 4.13. Recording and digitizing the fracture and other important characteristics of the $60 \times 60 \times 60\,\mathrm{cm}^3$-block.

Fig. 4.14. $90 \times 90 \times 80\,\mathrm{cm}^3$-block: Block sample on mobile platform.
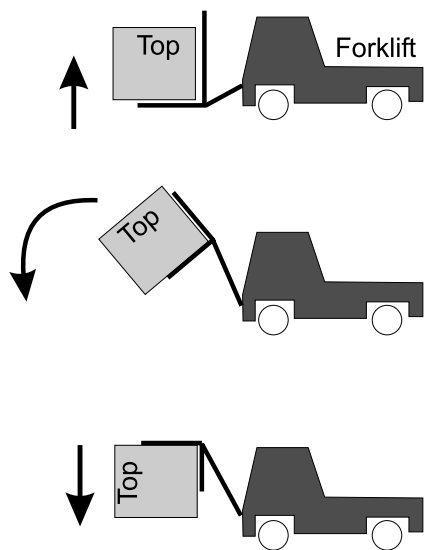
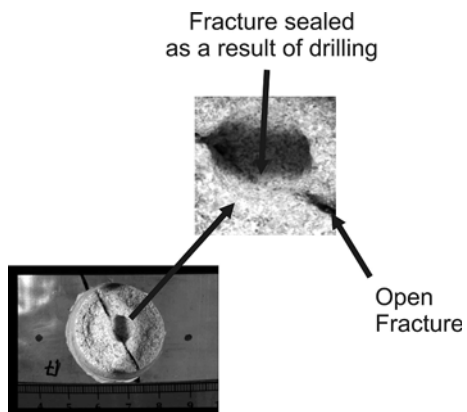**Fig. 4.15.** Rotation of block sample.

Fig. 4.16. Local sealing of matrix and fractures as a result of drilling.
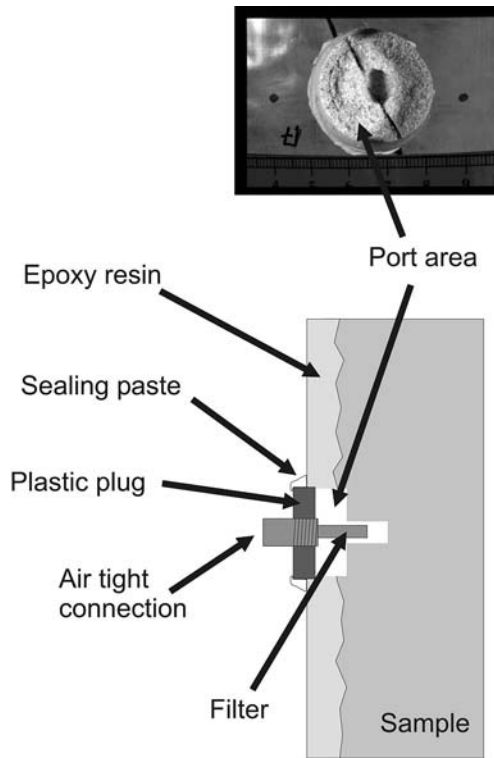
Fig. 4.17. Construction of the ports.
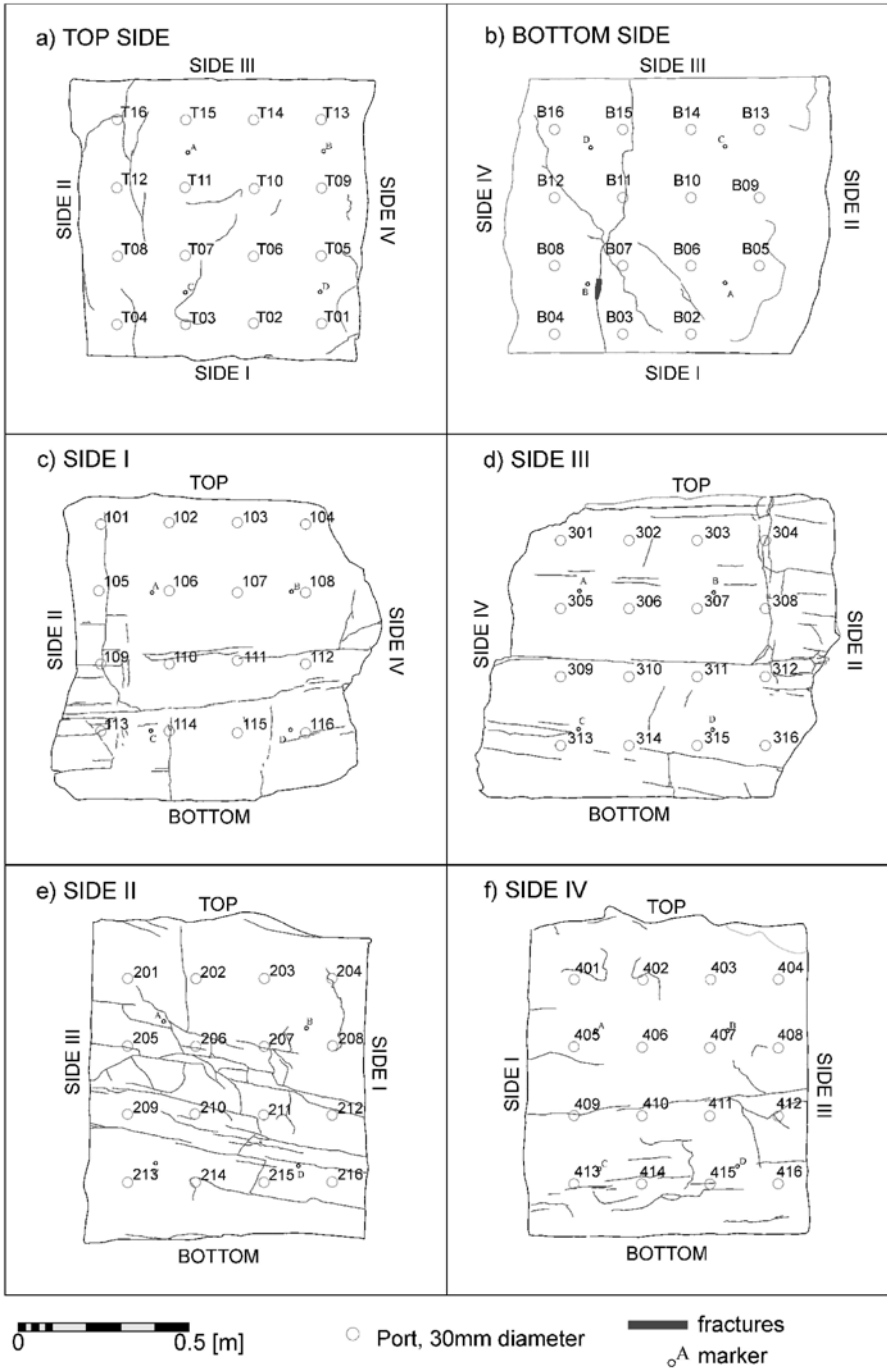
Fig. 4.18. Surface profiles and location of ports at the $90 \times 90 \times 80$ cm^3-block.
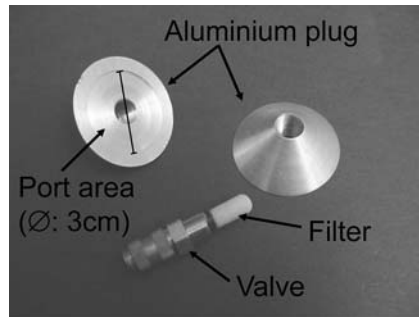
Fig. 4.19. Aluminium plugs used as port connections to the $60 \times 60 \times 60 \, \text{cm}^3$-block.
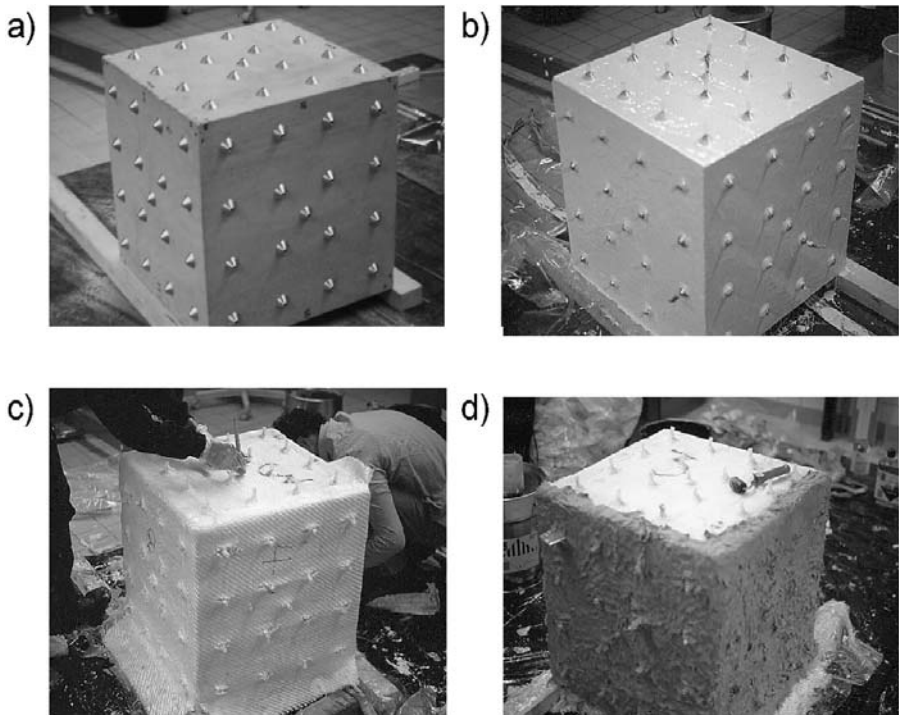
Fig. 4.20. Preparation of the $60 \times 60 \times 60 \, \text{cm}^3$-block. (a) Block with attached aluminium plugs. (b) Block with first resin coating. (c) Block with glass fiber mat coating. (d) Block with glass fiber plasticine coat.

a) Pressurizing the block sample

Block Sample

500 mbar
Input
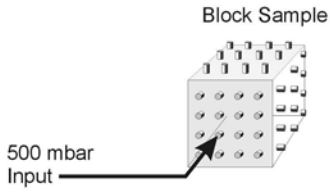
c) Water bath for submerging blocks

b) Monitoring the pressure in the
block to determine whether sealing leaks
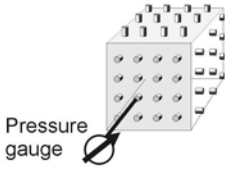
Pressure
gauge

d) Submerged block
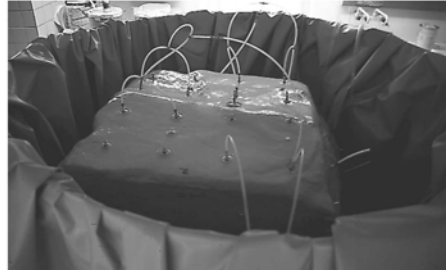
Fig. 4.21. Method for ensuring the hermetic sealing of the block. (a) Pressurizing the block sample. (b) Monitoring the pressure in the block to determine whether leaks are present. (c) Constructed water bath for submerging blocks and checking for leaks. (d) Partly submerged block.

4.2 Flow and Transport Experiments Conducted on Laboratory Cylinders

C.I. McDermott, M. Sauter, R. Liedl, G. Teutsch

In this section a flexible experimental technique allowing the experimental tomographical investigations of large scale laboratory samples (30 cm diameter x circa 35 cm length) is presented. The samples contain fracture networks and the experimental procedure is designed to allow for the measurement of discrete and integ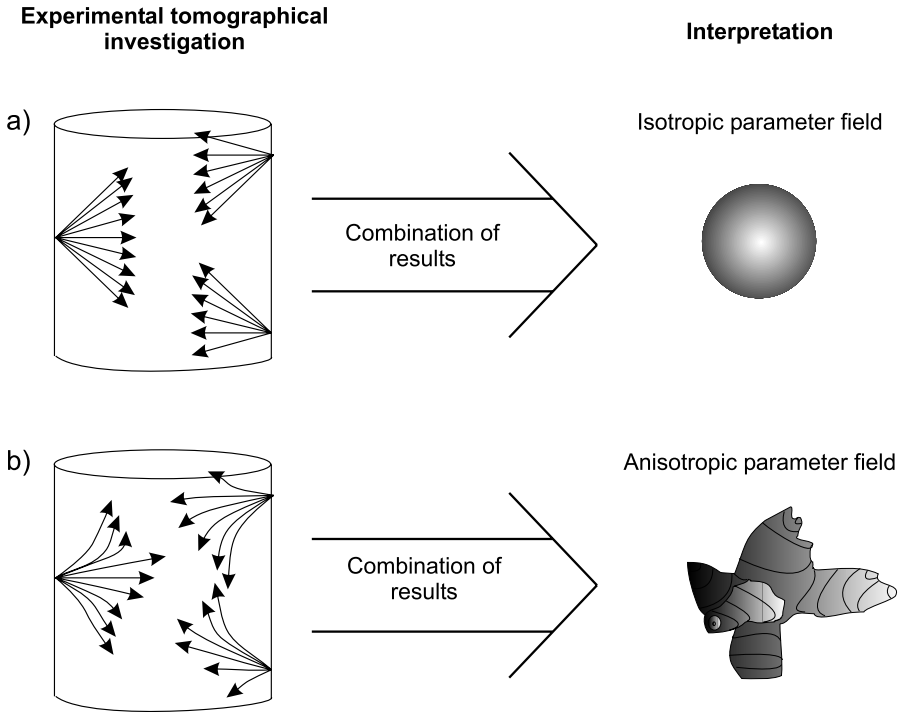ral signals of the constituent elements within the samples, i.e. matrix, individual fractures, fracture matrix interaction, and fracture network response. The signals can easily be evaluated in terms of the geometry of the system and scale of measurement.

4.2.1 Application and Method

In practical experimental terms, when the tomographical investigation concept is applied, it is necessary to make numerous point-to-point, or surface-to-surface measurements of flow and transport across a sample. Several point-to-point measurements are illustrated in 4.22a for a homogeneous isotropic sample and in 4.22b for an anisotropic sample. The results of the measurements are combined, using an appropriate model to produce a parameter field representing the processes causing the signal measured. Here, we concentrate on the experimental procedure and apply a simplified model to present the types of results available from the equipment developed.

To allow such a large number of measurements to be collected, gas flow techniques were applied, enabling the rapid measurement of flow (pressure and flow rate) and transport (tracer concentration) signals. Using gas flow techniques means it is not necessary to saturate the samples prior to the investigation, and very small flow rates could easily be measured rapidly with a high degree of accuracy. In contrast, a direct hydraulic tomographical investigation of such fractured porous samples has proved to be technically very difficult and time consuming (Hagemann, 2001) principally due to the problem of saturation. The saturation of the samples investigated was assumed to remain constant throughout the experimentation, allowing the comparison of the results. The conversion of gas flow parameters to hydraulic parameters has been investigated in detail by Jaritz (1999) for one-dimensional flow systems. In the current experimental cell, flow is anisotropic and multidimensional. The detailed effects of slip flow (Klinkenberg, 1941) and free molecular flow (Carman, 1956) still need to be considered on the basis of a modelled description of the flow system before a direct transfer of gas parameters to hydraulic parameters can be performed.

The difficulties and techniques for collecting fractured samples large enough so that the fracture network could be tomographically investigated, but small enough to remain manageable in the laboratory is discussed in

Interpretation

a)

Isotropic parameter field

Combination of results

b)

Anisotropic parameter field

Combination of results

Fig. 4.22. Principles behind the tomographical investigation of a fractured sample with isotropic a) and anisotropic b) parameter distribution (after McDermott *et al.* (2003a)).

McDermott *et al.* (2003b). Following the techniques presented in McDermott *et al.* (2003b) the samples collected for the experimental work have a diameter of 30cm and length of between 30 cm and 40 cm (Fig. 4.23). An example of the fracture record for such a sample is presented in Fig. 4.9.

In accordance with the concepts outlined above and the sample geometry, a special experimental cell was developed which allowed access to pre-selected positions along the surface of the sample (ports). Spatially orientated point-to-point measurements of the flow and transport characteristics could then be carried out from port-to-port. Additionally, the experimental cell was designed to adjust for samples differing in length (10 cm to 40 cm) and in diameter (290 mm $\pm$ circa 15 mm) and was able to maintain stable boundary conditions throughout the period of measurement. The principles and concepts behind the design of the cell to fulfil these criteria for reliable flow and transport measurements are presented in Fig. 4.24.

The experimental cell, named the Multi Input Output Jacket (MIOJ) formed the key element in the experimental set-up, the general arrangement of which is illustrated in Fig. 4.25. To investigate the flow and transport pa-
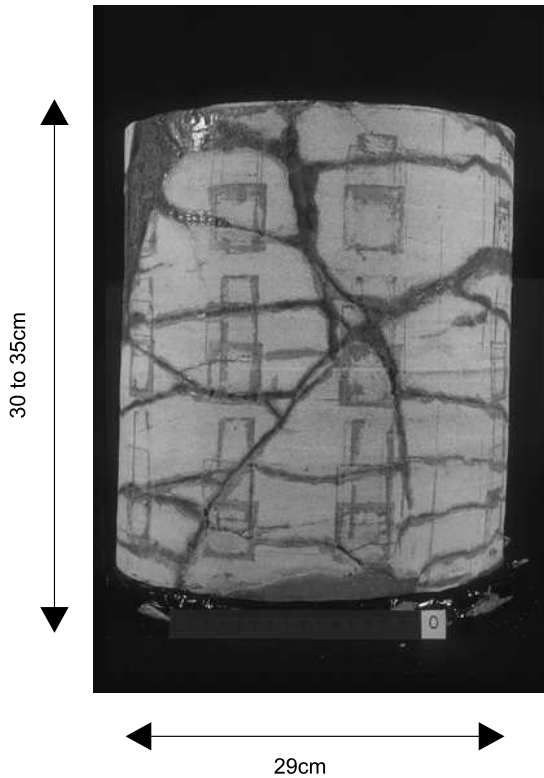
Fig. 4.23. Example of a fractured sample. The visible fractures are filled with sand (McDermott *et al.*, 2003a).

rameters, a stable linear flow field is established across the sample from the input port/ports to the output port/ports. The flow rate across the sample is recorded using a flow meter (a bubble meter is illustrated). Gas tracer is then injected via a flow-through loop (Jaritz, 1999) into the flow field before the input port/ports and the breakthrough of the gas tracer at the output port/ports is recorded using a mass spectrometer. The exact mass of the tracer introduced into the system is known, the location and the time of input, the mass recovered, location and rate of recovery are measured. Further details of the experimental procedure can be found in McDermott (1999).

4.2.2 Technical Details

The Multi Input Output Jacket (MIOJ) consists of two sealing membranes (outer and inner) with predefined open spaces or ports in them, three transparent curved polycarbonate shells (brace shells), two transparent polycarbonate circular plates (top / bottom plates) and a rigid frame. The functionality of the cell is achieved in that the membranes are pressed against the
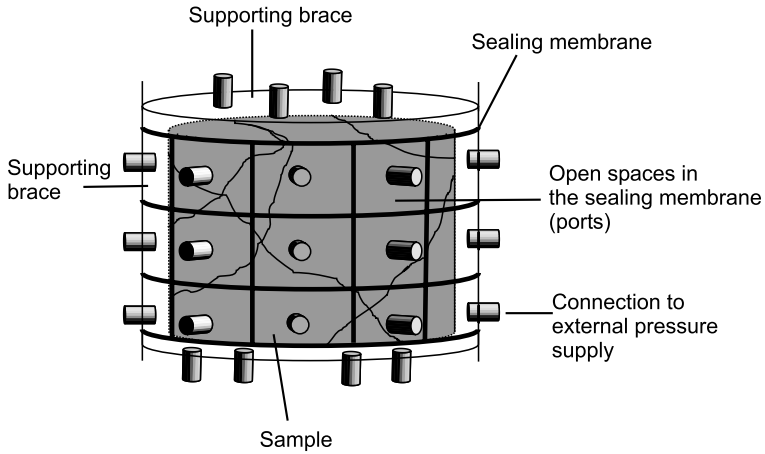
Fig. 4.24. Concepts and principles of the experimental cell enabling tomographic investigation of samples (McDermott *et al.*, 2003a).
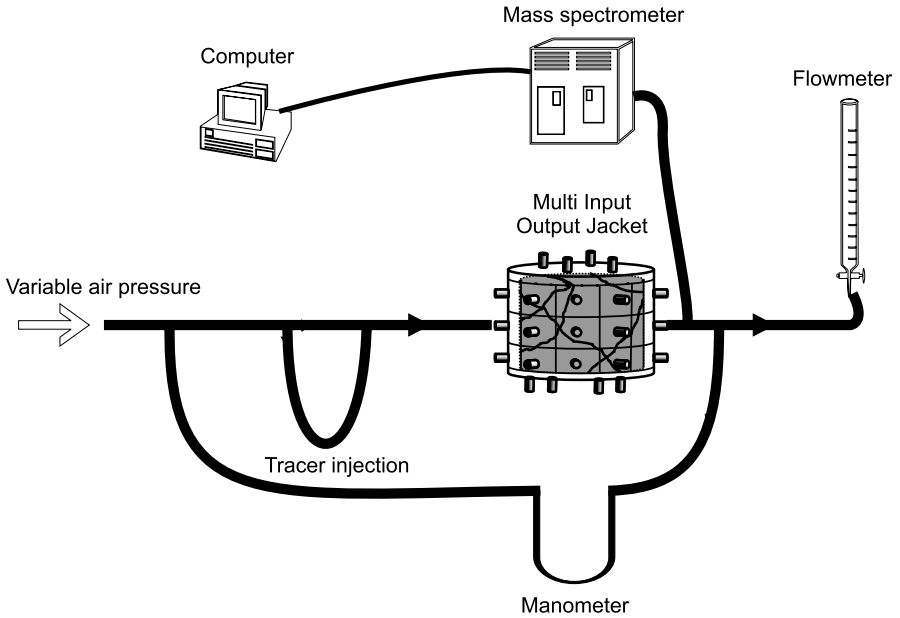
Fig. 4.25. Experimental set-up for investigation of cylindrical samples (McDermott *et al.*, 2003a).

sample with the use of the brace shells and the top and bottom plate, thereby forming a complete cylinder hermetically sealing the sample, Fig. 4.26.

The outer sealing membrane is formed by a soft rubber seal 5mm thick, the inner sealing membrane consists of a self adhesive elastomer 1mm to
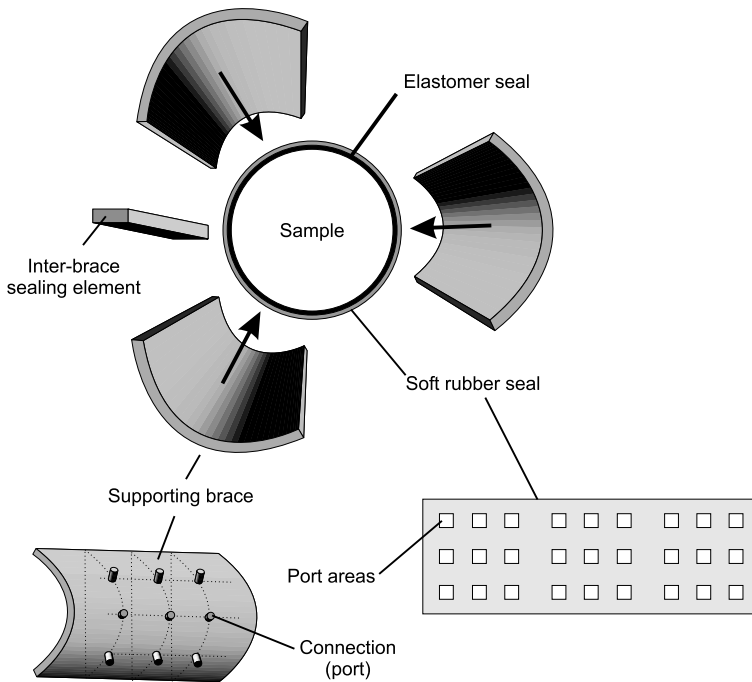
Fig. 4.26. Elements of the Multi Input Output Jacket (MIOJ), (McDermott *et al.*, 2003a).

2 mm thick (Fig. 4.27), stuck to the outer sealing membrane. Under the influence of pressure from the supporting brace, the membrane deforms and adjusts to any unevenness along the surface profile of the sample, thereby sealing any potential leaks. The ports for access to the sample are formed by the spaces in the membranes and each port can be connected to an external pressurized air supply through the connections in the supporting brace (Fig. 4.27).

As the individual brace shells are pressed onto the sealing membrane, the gap between the brace shells is filled with a soft rubber strip of the same material as the outer sealing membrane. The thickness of these inter-brace shell sealing elements can be varied to account for variations in the diameters of the samples.

The supporting brace is held against the sample by four metal bands (Fig. 4.28). These bands are removable and, when screwed together, exert an inward radial force on the brace. The top and bottom braces are pressed against the sample from a rigid frame and a series of screws (Fig. 4.28).

4.2.3 Procedure

Hermetically sealing the sample in the MIOJ and ensuring that flow from port-to-port occurred through the sample and not along the surface of the

Side view of an experimental port

Plan view of an experimental port after confining pressure is applied

Soft rubber sealing membrane

Elastomer sealing membrane

Fracture

Port area

Connection

Sample

Supporting brace

Original size of port prior to application of confining pressure

Ring exerting confining pressure on the supporting brace.
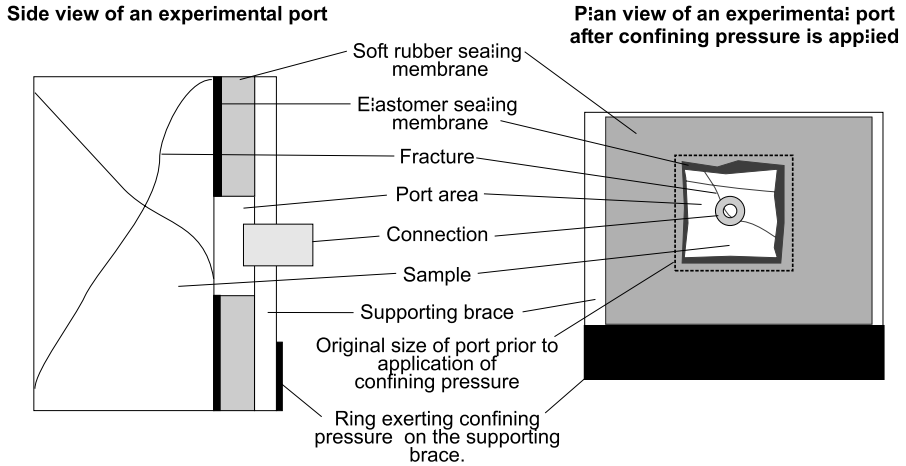
Fig. 4.27. Detailed view of the technique used to isolate port areas on the surface of the sample (McDermott *et al.*, 2003a).

Rigid frame

Top and bottom plate of supporting brace

Metal bands applying radial pressure to the supporting brace

Supporting brace (three wall parts)
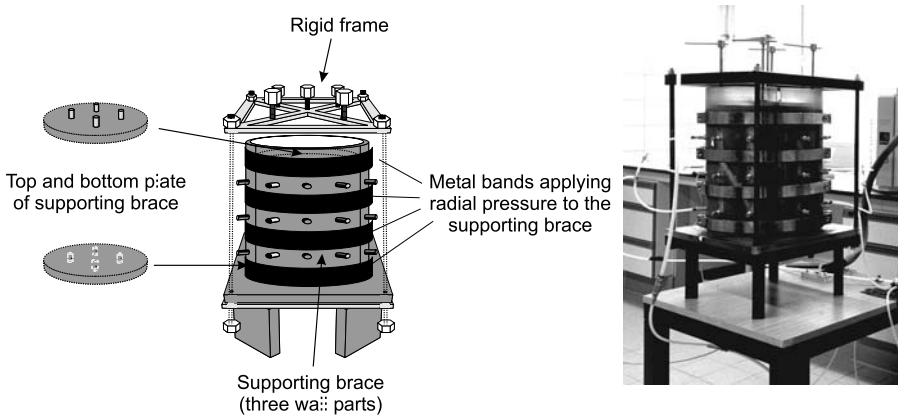
Fig. 4.28. Technical realization of the principle behind the MIOJ (McDermott *et al.*, 2003a).

sample as a result of insufficient contact of the sealing membrane with the surface of the sample (Fig. 4.29) required a lot of care. The techniques employed during the construction of the MIOJ to ensure these conditions included:

- ensuring that the sample was thoroughly cleaned from any fine loose material on the surface;
- any large scale unevenness or missing material from the sample was filled with silicon, thus enabling the sealing membrane of the MIOJ to have a smooth contact with the surface of the sample;

- where the sample had a weak consistency, a thin layer of silicon was placed around the locations of the input and output ports to aid in the sealing of these areas;
- for highly fractured samples, silicon was used to seal all the surface profile of the fractures apart from those areas appearing in ports. The silicon remained only on the surface of the sample and did not enter more than a couple of millimeters into the fracture itself; consequently, the permeability distribution remains practically unaffected. The silicon could be easily removed, allowing re-measurement of the sample using a new geometrical set-up of the ports;
- the outer surface of the sealing membrane was lubricated to ensure an even distribution of the pressure applied by the supporting brace on the sample.
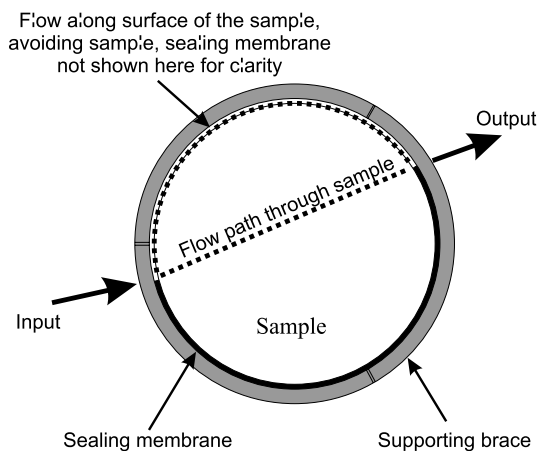
Fig. 4.29. Major flow paths through a cylindrical sample (McDermott *et al.*, 2003a).

Once the sample was sealed in the MIOJ, the apparatus was left for a period of 24 hours to make sure the sealing elastomer (inner sealing membrane) had time to plastically deform and fill any unevenness in the sample profile or block any potential leaks in the system. After this period, the airtightness of the MIOJ (comprising some 30 connections) was tested by ensuring it could maintain a pressure of some 150 mbar. Once it was clear that the system was airtight, stable benchmark flow measurements were made across the sample. After these results had been recorded, the pressure on the supporting brace (both edge and top and bottom) was increased slightly, the benchmark measurements repeated and the results compared. If the rate of flow remained constant, then it was assumed that the flow was through the sample. However, if the flow rate had been reduced by an increase of pressure exerted by the supporting brace, then flow along the surface of the

sample and not through the sample was assumed to be occurring. In such cases, the pressure exerted by the supporting brace was increased until no reduction in the flow rate was observed.

The benchmark measurements were repeated throughout the experimental investigation to ensure consistency of results. Both sealing membranes were deformable under light hand pressure; therefore, the effect of the pressure exerted by the supporting brace to ensure complete sealing of the sample on the fracture aperture due to the stiffness of the fractures was assumed to be negligible.

4.2.4 Flexibility of the MIOJ

Depending on the type of investigation required, different surface areas of the sample can be placed under a predefined pressure system, thus allowing a variety of adjustable boundary conditions in an enclosed system. The flow direction across the sample can easily be varied, and the anisotropy of flow and transport parameters can be determined (Fig. 4.30). The MIOJ is not just limited to point-to-point measurements. Any combination of the ports can be used to measure the flow and transport parameters depending on the geometry of the sealing membrane (Fig. 4.31).

As can be seen from Figs. 4.30 and 4.31, the dependency of the flow on scale effects such as the distance between the input and output ports or the size of the port area on the sample at a bench scale can easily be investigated as well as the effect of individual fractures in a fracture system or the fracture network itself.

Measurement of the flow field characteristics. The variable air pressure supply (Fig. 4.25), provided by a regulator valve, enabled a stable pressure difference to be established across the MIOJ. The flow rate across the sample as a result of this pressure difference was recorded using a flow meter. Experimental measurements indicated a linear relationship between flow and pressure difference with the application of a pressure difference of 150mbar in the fractured system and allowed for the assumption that linear flow conditions were present within the samples.

In practice, it was assumed that the stable flow field was established by maintaining stable boundary conditions for a period of five minutes. For the samples investigated, this period of time was determined experimentally by recording the change of the flow in the system against time from the initial conditions of 150 mbar plus atmospheric pressure in the whole sample to the new boundary conditions, i.e. 150 mbar plus atmospheric pressure on the input port to atmospheric pressure on the output port. Fig. 4.32 shows the change in the flow rate with time for such an experimental set-up for the cases where the matrix is connected to the input port. The steeper curve corresponds to the case where a fracture was directly connected to the output port. For the gentler curve, the matrix was connected to the output port. After five minutes, relative stability in the flow measurements can be seen to have

Connections   **Flow Path**

Top View   Side View
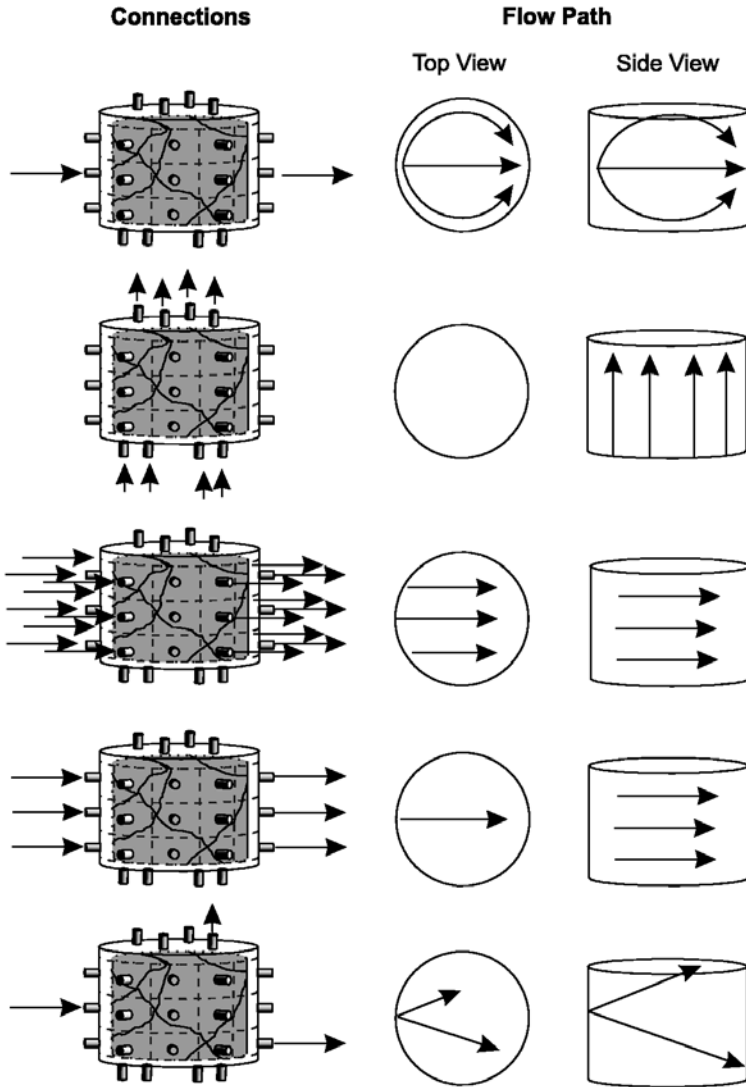
Fig. 4.30. Various configurations of input ports to output ports, allowing the spatial investigation of the flow and transport characteristics (McDermott *et al.*, 2003a).

been achieved. However, true stability in the case of the matrix connection was only achieved after 15 minutes.

Given the large number of measurements necessary to determine the spatially dependent flow and transport parameters, the time of at least 15 minutes per point-to-point experiment required to attain fully stable conditions was not practically possible. For an investigation series comprising several hundred individual point-to-point experiments, the time required
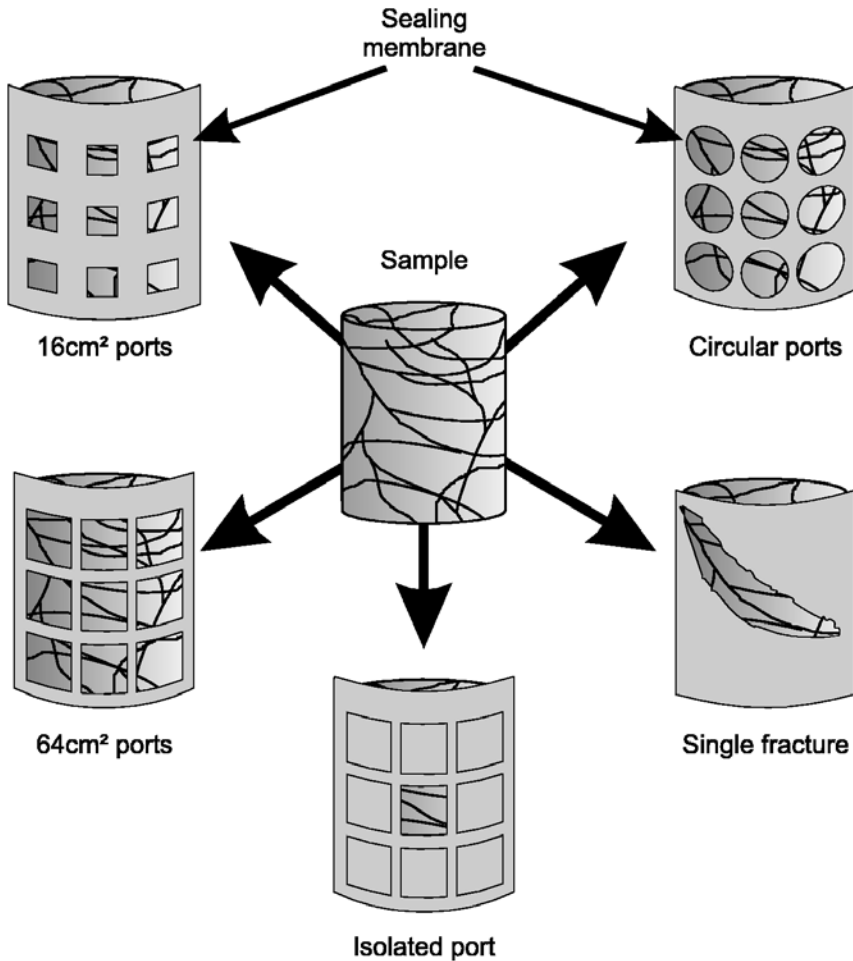
Fig. 4.31. Investigation possibilities of the MIOJ (McDermott *et al.*, 2003a).

for the measurements would have increased by a factor of three, but the accuracy of the results only minimally. Therefore, the error resulting from the possibility of slightly unstable flow conditions existing after five minutes was considered acceptable. Throughout an investigation series the cell was continually tested to prove that it was airtight, i.e. the valves, seals, pipes and any connections were not leaking

Measurement of the transport characteristics. To determine the transport characteristics of the system, it was necessary to undertake tracer tests. Tracer gas (helium) was injected via a flow-through loop into the stable flow field once established across the MIOJ (Fig. 4.25) to provide a Dirac pulse. The breakthrough of the tracer gas was recorded using a mass spectrometer.
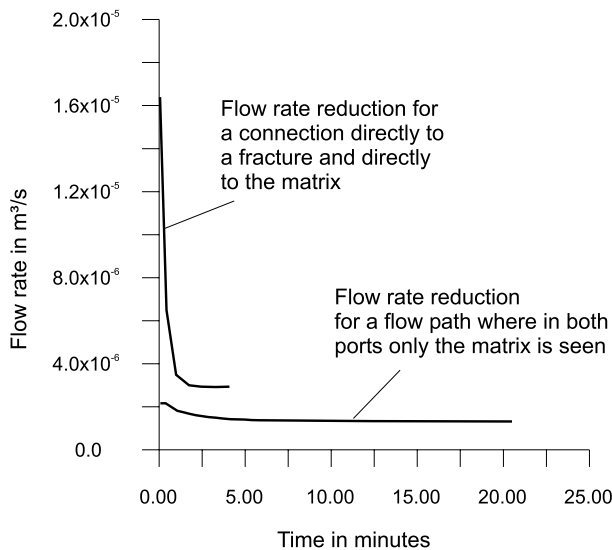
Fig. 4.32. Time taken for stabilization of the flow field in the MIOJ samples (example for sandstone samples with a matrix hydraulic conductivity of approximately $2.7 \cdot 10^{-6} \, \mathrm{m \, s^{-1}}$, where the entire sample was pre-pressurized to 150 mbar, then flow allowed from the output port at 0 mbar), (McDermott *et al.*, 2003a).

This injection technique enables the exact mass of the tracer introduced into the system and the time of input to be determined. If a constant pulse were used, the whole sample would become saturated with the tracer and, prior to further experimentation, the system would have to be flushed for a significant period of time.

To simplify the analysis of the transport information, a non-reactive gas, helium, was chosen as a tracer, thus eliminating the possibility of adsorption, retardation or biological degradation. In addition, the carrier gas used to establish the flow in the samples was air, and therefore the selection of helium was particularly convenient in that practically no helium is found naturally in air.

Examples of data recorded. The following data are available after the completion of every individual experiment:

- rate of flow across the sample,
- area of input and output ports,
- pressure at input port and pressure at output port,
- orientation of the input port to output ports and therefore first estimation of the geometry of the flow field,
- type and quantity of the tracer injected into the system,
- the breakthrough curve of the tracer at every extraction point.

After several experiments, the information available for each sample includes:

- differently scaled spatially dependent information about the flow field parameters;
- differently scaled spatially dependent information about the transport parameters.
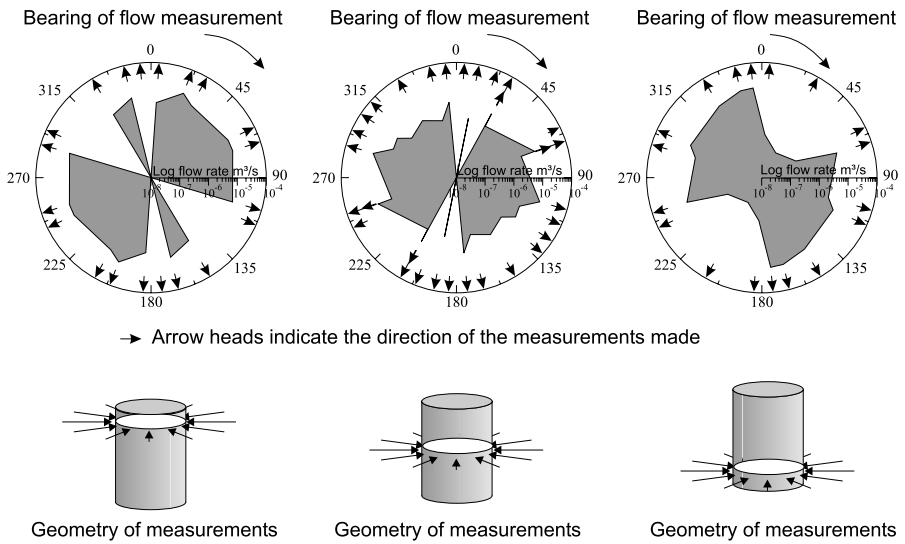
4.2.5 Flow Experiments

An extract example of the flow rate information recorded during experimentation is presented in Table 4.2. Examples of flow rate tensors derived from the experimental results for a highly fractured sandstone sample are presented in Figs. 4.33 and 4.34. In Fig. 4.33, three different levels of the sample are investigated via point-to-point measurements. In Fig. 4.34, the same sample is investigated along the length of the sides by connecting the input and output ports.

Table 4.2. Extract of data recorded in a pneumatic experimental investigation series. The cross section area of the port used is 0.001225 m^2.

Input port number	Output port number	Pressure diff. (mbar)	Volume flow rate (m^3/s)	Direct distance between ports (m)	Bearing deg. to north	Angle to horizontal
3	18	150	1.25E-05	0.285	166.2	0.0
13	2	150	6.74E-06	0.296	3.6	-19.7
15	2	150	5.39E-06	0.296	3.6	19.7
5	16	150	2.03E-06	0.296	148.8	19.7
1	14	150	4.29E-06	0.296	183.6	-19.7
2	13	150	6.70E-06	0.296	183.6	19.7
5	18	150	2.70E-06	0.296	148.8	-19.7
3	14	150	4.96E-06	0.296	183.6	19.7
1	32	150	8.04E-06	0.318	186.8	-51.8
3	10	150	1.94E-05	0.318	201.0	38.9
3	16	150	7.89E-06	0.348	166.2	35.1
1	18	150	9.44E-06	0.348	166.2	-35.1

The effects of scale on the measurement can immediately be seen from these simple diagrams. With the more discrete point-to-point approach (Fig. 4.30), there is a variation of the flow rate dependent on whether a fracture is directly connected to the port used for investigation. Some port-to-port flow rates are several orders of magnitude greater than others. However, with the more integral surface-to-surface approach, an averaging effect occurs leading to the tensor seen in Fig. 4.34.

This effect of moving from the discrete investigation scale to a more integral investigation according to the size of the ports used for investigation

Bearing of flow measurement

Bearing of flow measurement

Bearing of flow measurement

→ Arrow heads indicate the direction of the measurements made

Geometry of measurements   Geometry of measurements   Geometry of measurements

Fig. 4.33. Example of flow rate tensors derived from a highly fractured sample; here, the tomographical investigation proceeds along three separate planes in the sample (McDermott *et al.*, 2003a).

Bearing of flow measurement

Geometry of mesurements
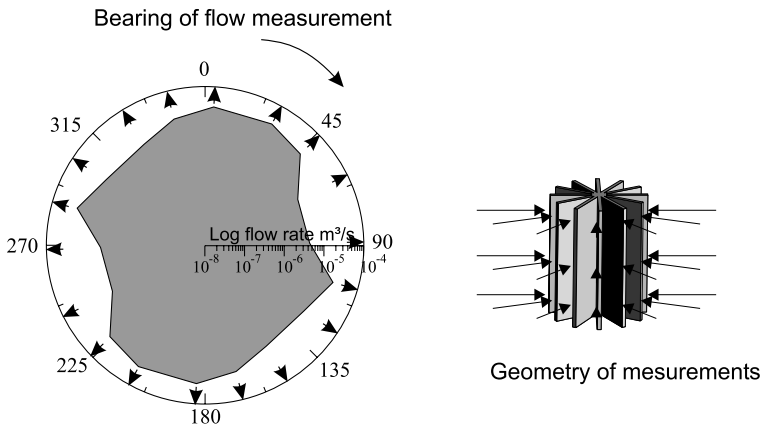
Fig. 4.34. Example of flow rate tensors derived from a highly fractured samples; here, complete side to side measurements are made (McDermott *et al.*, 2003a).

is illustrated in Fig. 4.35. Here, a simple one dimensional DARCYmodel has been used to convert the flow data into apparent hydraulic conductivity to allow the comparison of different scales of measurement. The term "apparent hydraulic conductivity"refers to the fact that this DARCYmodel is a significant simplification of the complex system and provides an apparent hydraulic conductivity. However, the more accurate multiple dimensional anal-

ysis of the flow and transport signals to derive actual hydraulic conductivities (e.g. Vesselinov *et al.* (2001), Leven *et al.* (2000), McDermott *et al.* (1998)) is beyond the scope of the current section. In Fig. 4.35, it can be seen that if the investigation areas are smaller then the distribution in apparent hydraulic conductivity is larger. Likewise, if the areas are larger then the variation is smaller. This illustrates the averaging effect of heterogeneities of a more integral signal in the larger areas to the more discrete signals from the smaller areas.
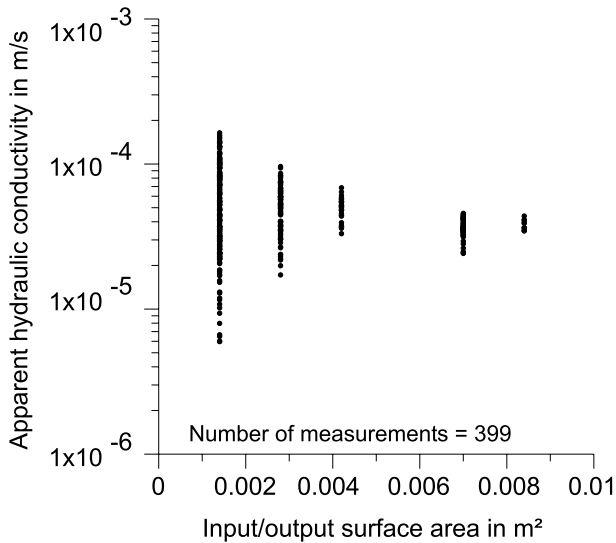
Fig. 4.35. Effect of the surface area on the variation in the apparent hydraulic conductivity (McDermott *et al.*, 2003a).

4.2.6 Transport Experiments

Typical results of transport experiments in the MIOJ are illustrated in Figs. 4.36 and 4.37. In Fig. 4.36, the characteristics are purely dominated by the matrix of the sample, which leads to a signal with a comparatively long tailing and a large arrival time. In contrast, Fig. 4.37 presents a number of different breakthrough curves, illustrating the variation in signal responses found from the MIOJ when a fracture was directly connected either to the input or output ports. Where fracture and matrix are involved in the transport, then interesting double and even triple peaks have been observed. In addition, the fracture network itself may also provide several different channels for flow, leading to different peaks in the breakthrough curve and several different ports may provide a signal from the fracture.
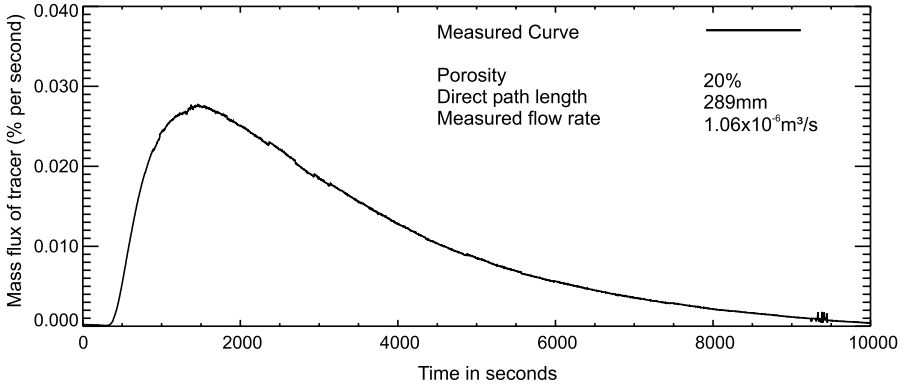
Fig. 4.36. Typical transport result from the MIOJ, dominated by matrix (McDermott *et al.*, 2003a).
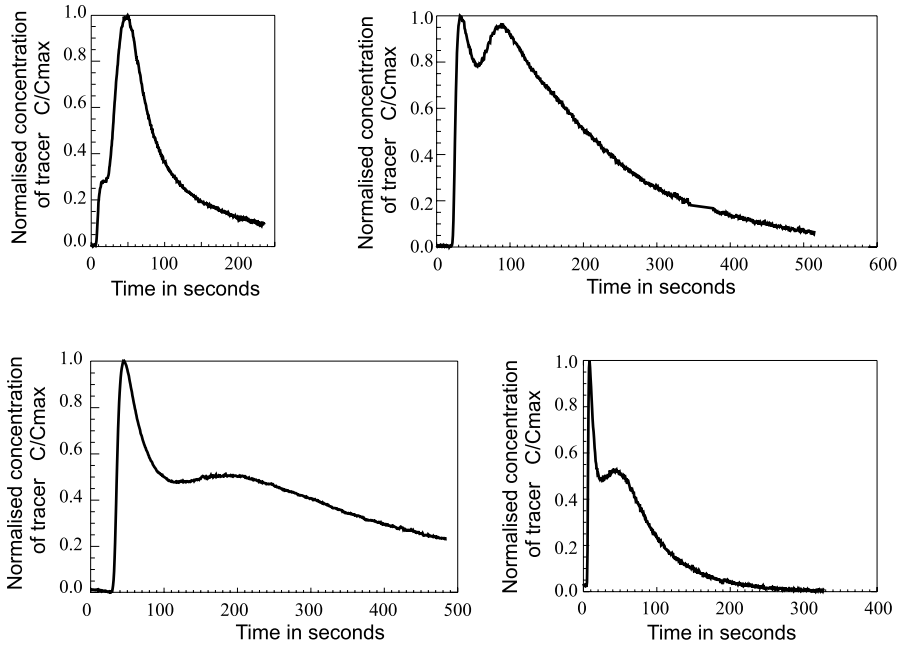
Fig. 4.37. Typical transport results from the MIOJ where fractures are directly connected to at least one of the investigation ports (McDermott *et al.*, 2003a).

4.2.7 Conclusions

The MIOJ provides a flexible innovative approach for the experimental tomographical investigation of fractured porous rock. The experimental method developed provides a wide variety of options for investigating flow and transport in a fracture network. The results gained from experimentation

show that it is possible to use the MIOJ to investigate fractured samples using a discrete and integral approach, to define orientated flow and transport tensors, and to investigate upscaling effects.

4.3 Interpretation of Flow and Transport Experiments Conducted on Laboratory Cylinders

By means of numerical model simulation, the significance of parameters and the relevance of occuring flow and transport processes can be investigated. A comparative analysis of measured and simulated results gives information about the properties of the investigated sample on the one hand, and about the possibilities and limitations of the chosen model concept on the other. In this section, investigation results from simulations conducted on one of the cylindrical bench scale samples discussed in Sects. 4.1.1 and 4.2 are presented. A sample with the dimensions 0.290 mm (height) and 0.286 mm (diameter) and a relatively high fracture density is chosen. The digitized record of the sample is shown in Fig. 4.9.

With the discrete model approach (Sect. 2.4), a sensitivity analysis is conducted (Sect. 4.3.1) in order to identify the significance of the flow and transport parameters involved. The results of this analysis are useful for the calibration of the model to the experimentally measured data (Sect. 4.3.2). The possibilities and limitations of using a discrete and a multi-continuum approach (Sect. 2.5) are investigated by determining equivalent parameters for flow and transport, applying the discrete model, and using them as input for a multi-continuum model (Sects. 4.3.3 and 4.3.4). The results from the two approaches are compared, allowing for an assessment of their feasibility on the current scale.

4.3.1 Sensitivity Analysis

L. Neunhäuserer, M. Süß, R. Helmig

When numerical models are used or the simulation results of such models judged, it is always essential to keep in mind that a model is an approximation and not an exact description (Fig. 2.1) of reality. This has a number of reasons:

- the material properties are approximated using model parameters;
- the exact structure of the domain is not known;
- the real problem is spatially and temporally discretized.

A sensitivity analysis is an important tool for determining the influence that these approximations may have. In this section, an analysis of the influence of the parameters permeability, porosity and dispersivity is presented. The aim of the analysis is to found a basis for the later comparison of measured and simulated tracer-breakthrough curves as presented in Sect. 4.3.2.

4.3.1.1 Model Set-Up

The structure information is recorded digitally in the laboratory and is then used to set up the structural model, which serves as a basis for the generation of the finite volume mesh used for the numerical simulation. Even though this example involves a rather small sample, the detection of the spatial distribution of the fractures is not trivial, but requires a certain amount of approximation.

For the purpose of the analyses presented here, a two-dimensional slice from the top of the core sample is selected. In Fig. 4.38, the two-dimensional structural model and the finite volume mesh are shown.
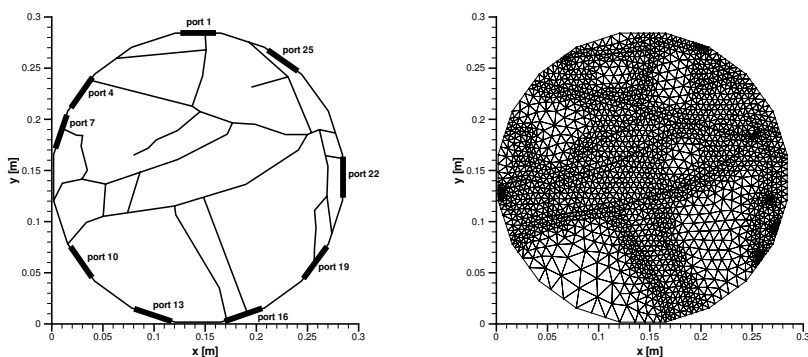
Fig. 4.38. Structural model with location of measurement ports (left) and finite volume mesh (right).

The simulations presented here consist of a steady-state flow calculation for the air-saturated, cylindrical sample and a subsequent transport simulation for a certain number of time steps. The flow field is simulated defining one inflow and one outflow port, where a constant pressure of 116 300 Pa and 101 300 Pa respectively is imposed. All other boundaries are impervious to flow. For the transport simulation, the tracer is injected as a pulse by keeping unit concentration constant until 30 ml of the tracer has entered the domain. The tracer leaves the domain through the outflow port over a free-flow boundary, allowing the concentration to be observed at this point. This set-up is designed in accordance with the actual measurements on the sample.

This set-up is used for sensitivity analysis (Sect. 4.3.1), calibration (Sect. 4.3.2) and determination of equivalent parameters (Sect. 4.3.2).

Measured flow and transport data for several combinations of ports are avaliable. For the comparison of measured and simulated data in this section (Sect. 4.3.1) and also for the calibration of the model as presented in

Sect. 4.3.2, the measurement with input port 1 and output port 10 is cho-
sen (1–10). The tracer-breakthrough curve of this measurement has a double
peak, which is considered typical for fractured porous media. Additionally,
the port combinations (1–4) and (1–16) are considered in Sect. 4.3.2.

4.3.1.2 Permeability

The influence of the permeability on the flow and transport behavior is pre-
sented on the basis of the results of three different simulations. The interest-
ing parameter is the ratio between the fracture and the matrix permeability,
and not the absolute values of these parameters. This ratio is a measure of the
contrast between the two constituents of the system. Here, the fracture per-
meability for all fractures is set to $4.1 \cdot 10^{-10}\,\mathrm{m^2}$, which corresponds to a frac-
ture aperture of 70 μm according to the cubic law. Three different matrix per-
meabilities are applied. Figure 4.39 shows the distribution of the piezometric
head for the three cases. The piezometric-head distributions demonstrate the
increasing significance of the fractures as the permeability ratio k_F/k_M in-
creases. The discharge is $Q_1 = 7.2 \cdot 10^{-5}\,\mathrm{m^3\,s^{-1}}$ (left), $Q_2 = 1.3 \cdot 10^{-5}\,\mathrm{m^3\,s^{-1}}$
(center) and $Q_3 = 0.6 \cdot 10^{-5}\,\mathrm{m^3\,s^{-1}}$ (right). The decreasing discharge, for a
constant discharge area, indicates a decreasing flow velocity in the matrix as
its permeability decreases.
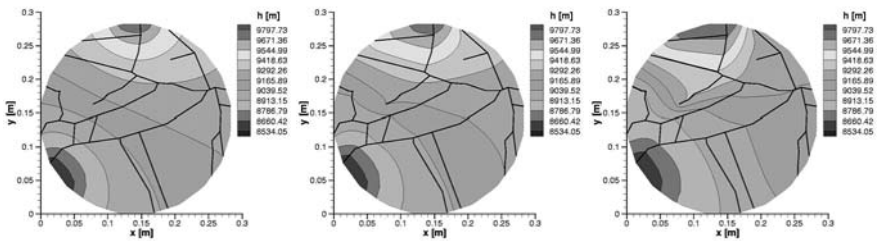
Fig. 4.39. Resulting piezometric-head distributions for $k_M = 3.0 \cdot 10^{-12}\,\mathrm{m^2}$ (left),
$k_M = 3.0 \cdot 10^{-13}\,\mathrm{m^2}$ (center) and $k_M = 3.0 \cdot 10^{-14}\,\mathrm{m^2}$ (right) (port configuration 1–
10).

For the transport calculation, the matrix and the fracture porosity are
fixed at $n_{e,M} = 0.20$ and $n_{e,F} = 0.30$ respectively for all three cases. The
dispersivity in the fracture is set to zero as the parallel-plate concept, i.e. the
fracture aperture is constant, is applied. For the matrix, a dispersivity of
$\alpha_l = \alpha_t = 0.01\,\mathrm{m}$ is assumed. The effective molecular diffusion coefficient is
set to $D_m = 1.0 \cdot 10^{-9}\,\mathrm{m^2\,s^{-1}}$, which is a very low value for air. Figure 4.40
shows the concentration distribution for the three cases at the same point
in time. The corresponding tracer-breakthrough curves are presented in Fig.
4.41.
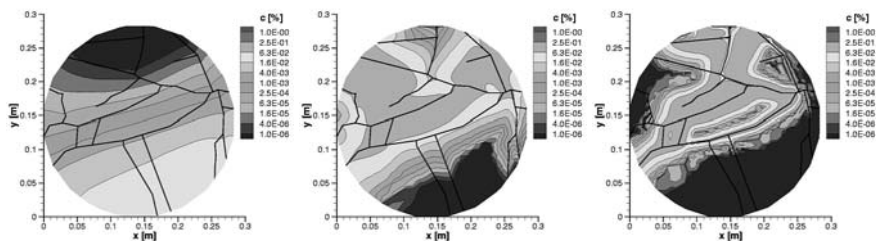
Fig. 4.40. Resulting concentration distributions for $k_M = 3.0 \cdot 10^{-12} \, \text{m}^2$ (left), $k_M = 3.0 \cdot 10^{-13} \, \text{m}^2$ (center) and $k_M = 3.0 \cdot 10^{-14} \, \text{m}^2$ (right) (port configuration 1–10).

For high matrix permeability, the transport process is only slightly influenced by the fractures. The main part of the tracer does not travel significantly more slowly in the matrix than in the fractures towards the output port. This yields an early high peak. The tailing is mainly caused by the asymmetry of the system forcing a portion of the tracer mass to travel a longer distance.

For the intermediate matrix permeability, the transport of the tracer mass in the matrix is significantly slower than for the first case. However, a large part of the mass enters the matrix from the fractures, so that the peak of the tracer-breakthrough curve is substantially lower. The tailing results from the relatively large portion of mass distributed in the total matrix.

Low matrix permeability yields a tracer-breakthrough curve which has an earlier and sharper increase than for the intermediate permeability. The flow and the transport are mainly bundled to the fractures. The double peak of the tracer-breakthrough curve is in this case caused by the two different main flow paths in the fracture system. The tracer mass in the matrix is only removed very slowly, causing a pronounced tailing.

4.3.1.3 Porosity

The influence of the porosity on the flow and transport processes is discussed, using the case with the intermediate matrix permeability. The values of dispersivity and diffusion remain the same as in the previous example. Again, the parameter for the fractures is kept constant, i.e. the fracture porosity is fixed at $n_{e,F} = 0.30$, whereas the matrix porosity $n_{e,M}$ is set to $0.05, 0.15$ or 0.20. Consequently, the right plot in Fig. 4.42 is the same as the center plot in Fig. 4.40.

The change in porosity is reflected in the change of the seepage velocity, i.e. a low porosity yields a high seepage velocity and vice versa. Consequently, the centroid of the tracer-breakthrough curve is shifted to the right for larger porosities as a reaction to the slower advective transport. Addi-
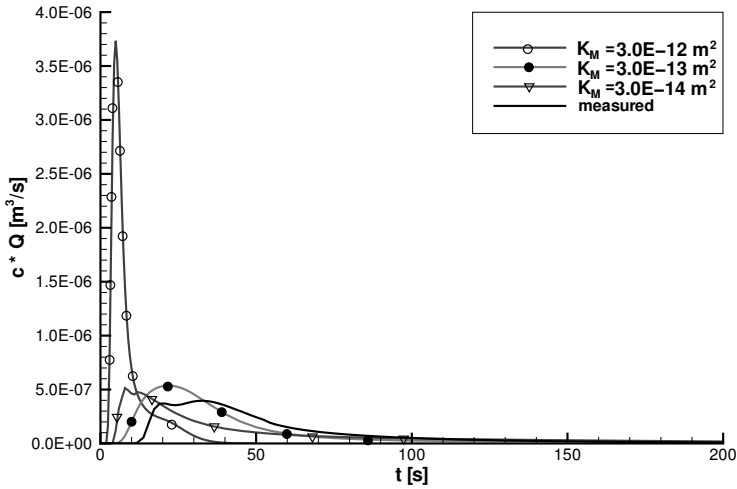
Fig. 4.41. Resulting tracer-breakthrough curves for $k_M = 3.0 \cdot 10^{-12}\,\text{m}^2$, $k_M = 3.0 \cdot 10^{-13}\,\text{m}^2$ and $k_M = 3.0 \cdot 10^{-14}\,\text{m}^2$. The concentration is multiplied by the corresponding discharge in order to achieve comparability.
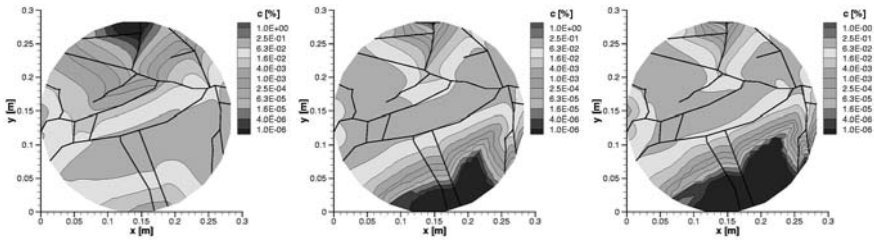
Fig. 4.42. Resulting concentration distributions for $n_{e,F} = 0.05$ (left), $n_{e,F} = 0.15$ (center) and $n_{e,F} = 0.20$ (right) (port configuration 1–10).

tionally, the seepage velocity has an impact on the dispersion term, which increases with decreasing porosity. This yields a smoother concentration front.

Further simulations show that the variation of the fracture porosity, within realistic limits, does not have an essential effect on the processes. This is explained by the small part of the total volume occupied by fractures.

4.3.1.4 Dispersivity

To demonstrate the influence of the dispersivity, again the case with intermediate matrix permeability discussed in Sect. 4.3.1.2 is used as reference. Only the matrix dispersivity is varied. In the first simulation, it is set to
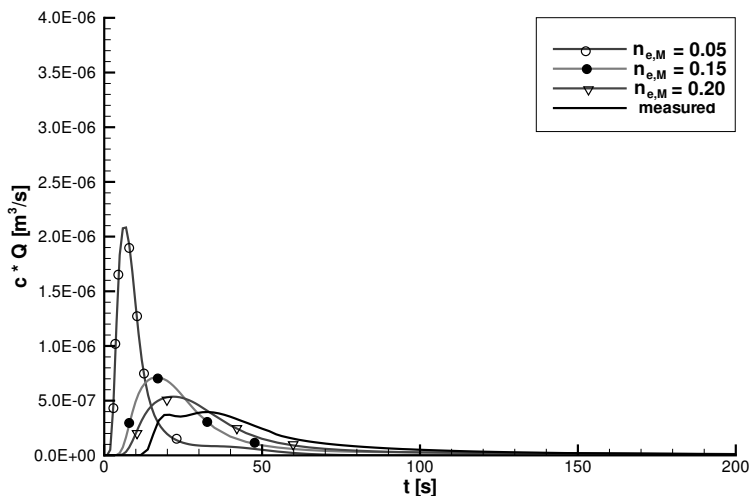
Fig. 4.43. Resulting tracer-breakthrough curves for $n_{e,F} = 0.05$, $n_{e,F} = 0.15$ and $n_{e,F} = 0.20$. The concentration is multiplied by the corresponding discharge in order to achieve comparability.

$\alpha_l = \alpha_t = 0.01$ m, i.e. no change from the reference case. In the second simulation, the value is decreased to $\alpha_l = \alpha_t = 0.001$ m. Figure 4.44 shows the resulting tracer-breakthrough curves.

The decrease of the matrix dispersivity yields a more emphasized advective transport process with a sharper concentration front. The initial arrival occurs earlier and the increase of the tracer-breakthrough curve is faster, due to the smaller portion of the tracer mass entering the matrix from the fractures. Analyzing the concentration distributions for each of the time steps (not presented here) leads to the conclusion that the portion of tracer mass initially entering the matrix and the tracer mass entering the matrix from the fractures is mainly advectively transported through the matrix. This is the main reason for the second peak of the tracer-breakthrough curve. Normally, a portion of tracer mass re-enters the fractures from the matrix because of the steep concentration gradient. Here, however, because of the relatively high permeability of the matrix, the amount that re-enters is negligible.

4.3.1.5 Remarks

In general, it can be stated that a fractured porous system on the considered scale is more sensitive to changes in the matrix parameters (porosity and dispersivity) than to those in the fracture parameters. This is comprehensible, considering the fact that the relative volume of the fractures compared
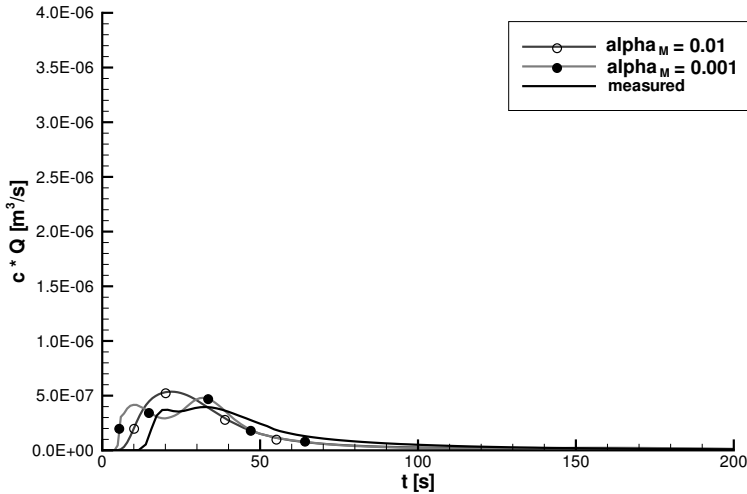
Fig. 4.44. Resulting tracer-breakthrough curves for $\alpha_l = \alpha_t = 0.01$ m and $\alpha_l = \alpha_t = 0.001$ m. The concentration is multiplied by the corresponding discharge in order to achieve comparability.

to that of the matrix is very small. Exceptions from this are parameters describing the geometry of the fractures, i.e. fracture density, fracture distance, fracture length and fracture aperture (determining the fracture permeability). The smaller the scale and the stronger the permeability contrast between fractures and matrix, the more important it is weather a fracture is connected to an in- or outflow boundary or not. The same is valid for the connectivity between the fractures.

4.3.2 Comparison of Measured and Simulated Tracer-Breakthrough Curves

L. Neunhäuserer, M. Süß, R. Helmig

In this section, the calibration of the model aiming at the reproduction of the actually measured tracer-breakthrough curves and the corresponding discharges (Sect. 4.2) is discussed. Calibration is in general performed in order to determine a valid set of model parameters that enables the use of a model for the prediction of flow and/or transport behavior for different boundary conditions. Here, the purpose of the calibration is to understand and learn more about the characteristics of the sample investigated rather than actually achieve a calibrated and verified model. The knowledge gained from the sensitivity analysis (Sect. 4.3.1) is a useful support for the calibration process. The model set-up as described in Sect. 4.3.1.1 is applied. The measured data

from the port configurations (1–4), (1–10) and (1–16) are selected to represent the system.

4.3.2.1 Calibration

Since the flow field mainly determines the transport process, the first step is to find a parameter set that can reproduce the measured discharges. In order to align the simulated results with the measured values, the fracture apertures and the matrix permeability are varied. For such a task, the conclusions drawn in Sect. 4.3.1 are very helpful. Figure 4.45 presents a possible parameter set together with the measured and the simulated discharges. The corresponding piezometric-head distributions are shown in Fig. 4.46.

The transport simulations are performed for a number of parameter sets (see Table 4.3), all on the basis of specifications based on experimental data

	$k\,(\mathrm{m}^2)$	$b\,(\mu\mathrm{m})$
Matrix	$9.3 \cdot 10^{-14}$	–
Frac. type 1	$6.7 \cdot 10^{-10}$	90.0
Frac. type 2	$9.6 \cdot 10^{-11}$	34.0
Frac. type 3	$1.9 \cdot 10^{-10}$	48.0

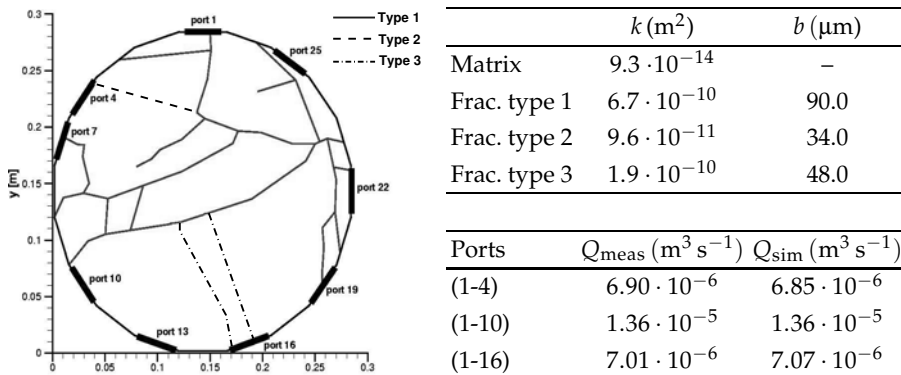| Ports	$Q_{\mathrm{meas}}\,(\mathrm{m}^3\,\mathrm{s}^{-1})$	$Q_{\mathrm{sim}}\,(\mathrm{m}^3\,\mathrm{s}^{-1})$
(1-4)	$6.90 \cdot 10^{-6}$	$6.85 \cdot 10^{-6}$
(1-10)	$1.36 \cdot 10^{-5}$	$1.36 \cdot 10^{-5}$
(1-16)	$7.01 \cdot 10^{-6}$	$7.07 \cdot 10^{-6}$

Fig. 4.45. Structural model with ports (left) and parameter set 1 together with the measured and the simulated discharges (right).
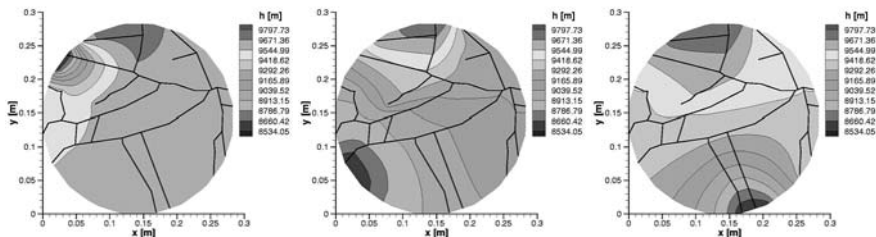

Fig. 4.46. Piezometric-head distribution for parameter set 1 for port configuration 1–4 (left), 1–10 (center) and 1–16 (right).

(Sect. 4.2). The parameters varied are the matrix and the fracture porosities. The corresponding tracer-breakthrough curves for port configuration (1-10) are presented in Fig. 4.47. From this figure, it becomes clear that first, independently of the parameter set, the initial arrival of the tracer occurs too early compared to the measured curve. Second, none of the simulated curves exhibit a double peak. Third, it is pointed out that the curves of parameter set 1-2 and 1-4, only differing in the fracture porosity, can scarcely be distinguished. The lack of sensitivity to this parameter is discussed in Sect. 4.3.1.3.

Table 4.3. Parameter sets for the transport simulation based on flow parameter set 1.

	$n_{e,M}$ (-)	$n_{e,F}$ (-)	$\alpha_{l,M} = \alpha_{t,M}$ (m)	α_F (m)	D_m (m^2 s^{-1})
Parameter set 1-1	0.20	0.30	0.001	0.0	$6.12 \cdot 10^{-5}$
Parameter set 1-2	0.25	0.30	0.001	0.0	$6.12 \cdot 10^{-5}$
Parameter set 1-3	0.30	0.30	0.001	0.0	$6.12 \cdot 10^{-5}$
Parameter set 1-4	0.25	0.35	0.001	0.0	$6.12 \cdot 10^{-5}$
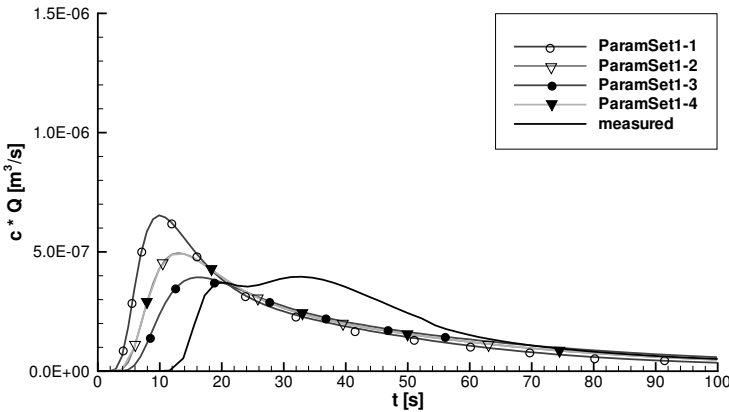
Fig. 4.47. Tracer-breakthrough curves for port configuration (1-10) corresponding to the values listed in Table 4.3. The concentration c is multiplied by the corresponding discharge Q in order to achieve comparability.

In order to fit the initial arrival time of configuration (1-10) better, the fracture aperture of fracture type 1, essential for this port connection, is reduced. As a consequence, the matrix permeability must be increased, in order to maintain the correct discharge. These changes lead to too large a discharge

	$k\,(\mathrm{m}^2)$	$b\,(\mu\mathrm{m})$
Matrix	$1.5 \cdot 10^{-13}$	–
Frac. type 1	$5.9 \cdot 10^{-10}$	84.5
Frac. type 2	$3.3 \cdot 10^{-11}$	20.0
Frac. type 3	$1.2 \cdot 10^{-10}$	38.0

Ports	$Q_{\mathrm{meas}}\,(\mathrm{m}^3\,\mathrm{s}^{-1})$	$Q_{\mathrm{sim}}\,(\mathrm{m}^3\,\mathrm{s}^{-1})$
(1-4)	$6.90 \cdot 10^{-6}$	$8.03 \cdot 10^{-6}$
(1-10)	$1.36 \cdot 10^{-5}$	$1.36 \cdot 10^{-5}$
(1-16)	$7.01 \cdot 10^{-6}$	$7.05 \cdot 10^{-6}$
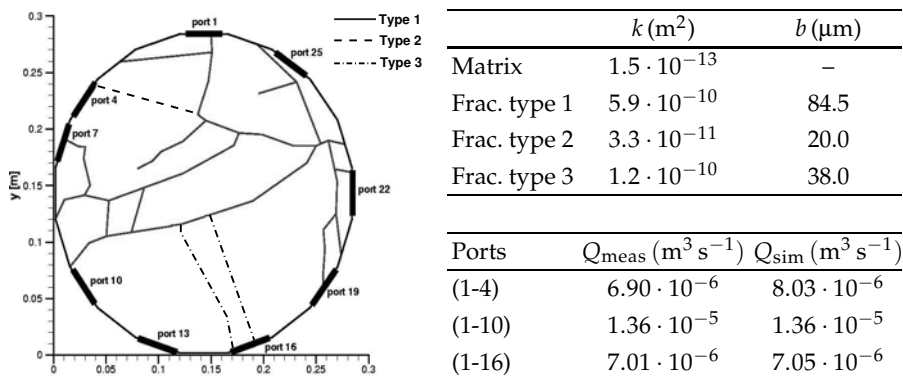
Fig. 4.48. Structural model with ports (left) and parameter set 2 together with the measured and the simulated discharges (right).
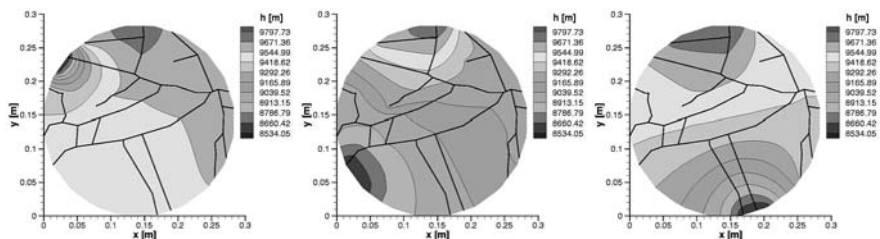

Fig. 4.49. Piezometric-head distribution for parameter set 2 for port configuration 1-4 (left), 1-10 (center) and 1-16 (right).

for port configuration (1-4). To account for this effect, the aperture for fracture type 2 must be set to a diminishingly small value (see Fig. 4.48).

Figure 4.49 shows the piezometric-head distribution for the three port configurations for parameter set 2. Despite the fact that the discharge for port configuration (1-4) could not be satisfactory reproduced, the transport behavior is investigated in order to analyze the influence that parameter changes may have. Table 4.4 summarizes the parameter values used for the transport simulations. The corresponding tracer-breakthrough curves, represented in Fig. 4.50, are divided into two groups according to the values of the matrix dispersivity and the molecular diffusion. These two values affect the shape of the tracer breakthrough curve in the same way.

The first of the two groups (parameter sets 2-1 and 2-2) is characterized by a sharp concentration increase and a high peak. Additionally, the curves in this group have a tendency towards a second local maximum.

Table 4.4. Parameter sets for the transport simulation based on flow parameter set 2.

	$n_{e,M}$ (-)	$n_{e,F}$ (-)	$\alpha_{l,M} = \alpha_{t,M}$ (m)	α_F (m)	D_m (m^2 s^{-1})
Parameter set 2-1	0.20	0.30	0.005	0.0	$1.00 \cdot 10^{-9}$
Parameter set 2-2	0.25	0.30	0.005	0.0	$1.00 \cdot 10^{-9}$
Parameter set 2-3	0.25	0.30	0.001	0.0	$6.12 \cdot 10^{-5}$
Parameter set 2-4	0.30	0.30	0.001	0.0	$6.12 \cdot 10^{-5}$
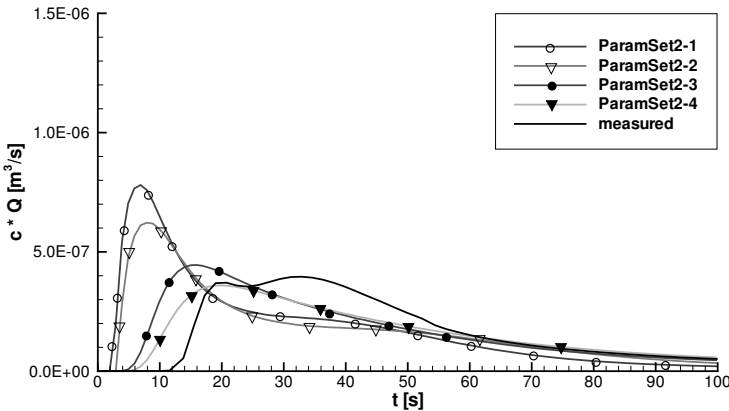
Fig. 4.50. Tracer-breakthrough curves for port configuration (1-10) corresponding to the values listed in Table 4.4. The concentration is multiplied by the corresponding discharge in order to achieve comparability.

The second group (parameter sets 2-3 and 2-4) shows a smoother concentration increase and the peak concentration is significantly lower than the one of the first group. The tailing decreases monotonically without local maxima. Compared to the parameter sets 1-2 and 1-3 (identical transport-parameter values), a later initial arrival time is achieved. However, the peak concentration is lower and the tailing more pronounced than for these sets. This is explained by the changed flow fields, allowing more tracer mass to enter the matrix.

4.3.2.2 Conclusions

The reproduction of the measured discharges proves to be straightforward. However, it must be assumed that multiple parameter sets exist, all satisfying the measured discharges. The assumed permeability distribution must therefore be validated by a transport simulation.

The fracture apertures resulting from the simulations are to be understood as effective model parameters. The fractures are considered to be one-

dimensional elements, in which flow conditions according to POISEUILLE are assumed. The transformation from fracture aperture to fracture permeability is realized by applying the cubic law (Sect. 2.4). The fractures of the sample analyzed here show a width of a few millimeters including the weathered zone and, to a large extent, contain a sandy filling material. A possible way of including this in the model is to discretely model not only the fractures but also the complete weathered zone, using two-dimensional elements with a permeability which is independent of the fracture aperture.

The determination of the transport parameters is not trivial. For the chosen example, port configuration (1–10), parameter values are found that reproduce the measured tracer-breakthrough curve relatively well, i.e. in a similar order of magnitude. An essential deficit of the simulated curves is, however, the lack of the characteristic double peak. Therefore, no unique answer can be given to the question as to the reason for this behavior, either the response to two different dominant flow paths or a double-continuum behavior. Additionally, the initial arrival time is not reached. The reasons for these deficits are multifold:

a) Reasons connected with simulation technique:
   – Due to the fractured structure of the core sample, three-dimensional effects may occur, which cannot be reproduced using a two-dimensional model.
   – The description of the fractures using one-dimensional elements may not be suitable, but a realization of the complete weathered zone might be a better solution. Applying a lower permeability of the fractures would allow a better reproduction of the initial arrival time. In this case, the double peak would be the response to two different dominant flow paths.
b) Reasons connected with measurement technique:
   A renewed and detailed inspection of the experimental set-up used to conduct the measurements revealed that the tracer impulse travels through a piece of tubing before entering the core sample as well as after leaving the sample on the way to the concentration measurement. The time recording starts as the pulse is injected into the tubing. Depending on the distance from the point of injection to the inflow port, a delay of the tracer mass must be expected.

From the experience gained with this sample, it can be concluded that, even though the scale is relatively small and the amount of data is large, it is not a trivial task to set up a numerical model that reproduces the measurements correctly. Consequently, the complexity of this task increases as the problem scale is enlarged. This indicates the great challenge that has to be faced when dealing with strongly heterogeneous porous media and especially with fractured porous media.

For a comprehensive and detailed discussion of the influence on structures, such as for example fractures, on flow and transport behaviour and the interpretation of measured data from such systems, we refer to Süß (2004).

4.3.3 Determination of Equivalent Parameters

L. Neunhäuserer, M. Süß, R. Helmig

Flow and transport processes as well as heterogeneities and material properties on local scales affect the system behavior on larger scales. The realization of a large-scale area, based on detailed small-scale information, in a model is generally not possible, first because the required data density is not achievable and, second because the required computational effort is not reasonable. In order to reduce the degree of detail of the system, physically relevant parameters and processes on different scales are identified and transformed into equivalent parameters. In this way, equivalent parameters enable the consideration of small-scale processes on larger scales, achieving a simplified system description.

For the system set-up discussed in Sect. 4.3.1.1, equivalent parameters are determined, applying the discrete model, for the use in a continuum model (Sect. 4.3.4). Methods for the determination of equivalent parameters are explained in Sects. 2.5.5.1 – 2.5.5.3.

For the reasons discussed in Sect. 4.3.2, it is not possible to determine a satisfying parameter set for the cylindrical bench-scale sample under investigation using a discrete model. It is therefore decided to use a fictive parameter set based on measurements and observations given in 4.2 and to compare the results of the discrete and the continuum model results.

Due to the relatively low fracture density of the sample, the current system does not allow the identification of two different continua, representing the fractures and the matrix. Consequently, equivalent parameters for one single continuum are determined.

The parameter values used for the discrete model runs and the notation of the boundaries are presented in Fig. 4.51. For this example, the fluid chosen is water. At the in- and outflow boundaries, constant hydraulic heads of $h = 11.63$ m and $h = 10.13$ m respectively are imposed. Assuming incompressibility, the choice of fluid does not in principle affect the results. Following the conversion of the obtained hydraulic conductivity tensor to a permeability tensor according to equation (2.11), the same result is achieved for both gas and water.

4.3.3.1 Flow Parameters

The determination of the equivalent hydraulic-conductivity tensor is carried out according to the procedure described in Sect. 2.5.5.1. The result is presented in Fig. 4.52. In the graph (left), the calculated values as well as the
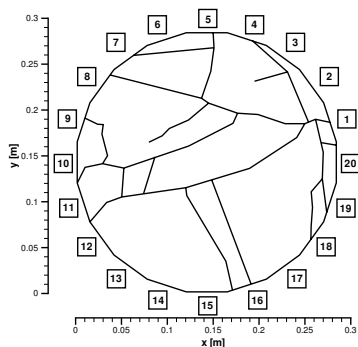
	Fracture	Matrix
Hydr. cond. K (m s^{-1})	$2.5 \cdot 10^{-2}$	$2.5 \cdot 10^{-5}$
Eff. por. n_{e} (-)	0.30	0.20
Disp. α (m)	0.01	0.00
Mol. diff. D_{m} (m^2 s^{-1})	$1.0 \cdot 10^{-9}$	$1.0 \cdot 10^{-9}$

Fig. 4.51. Boundary notation (left) and flow and transport parameters (right).
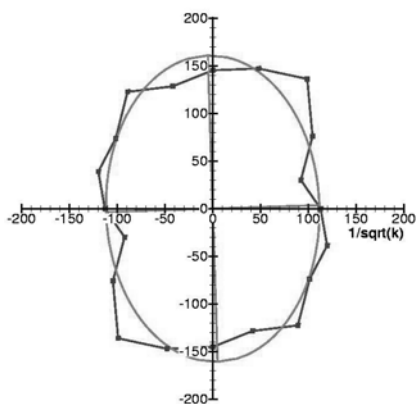
Hydr. cond. $K_{i,j}$, xy-system	
$K_{xx}[ms^{-1}]$	$8.02 \cdot 10^{-5}$
$K_{xy}[ms^{-1}]$	$0.13 \cdot 10^{-5}$
$K_{yy}[ms^{-1}]$	$3.87 \cdot 10^{-5}$
Hydr. cond. $K_{i,j}$, princ. comp. system	
$K_1[ms^{-1}]$	$8.03 \cdot 10^{-5}$
$K_2[ms^{-1}]$	$3.86 \cdot 10^{-5}$
Angle betw. xy- and princ. comp. system	
α_1	1.80382^{o}
α_2	-88.19618^{o}

Fig. 4.52. Left: Hydraulic conductivity tensor with calculated values and fitted ellipse with principal components. Right: Resulting equivalent parameters.

fitted ellipse are plotted as $1/\sqrt{K}$, i.e. the largest hydraulic conductivity is found in the horizontal direction.

In order to assess the influence of the homogenization on the flow behavior and to check the plausibility of the equivalent hydraulic-conductivity tensor, it is implemented in a homogeneous system without fractures but with the same geometry and boundary conditions as the discrete model. The discharges for the ten port configurations are then determined as listed in Table 4.5 together with the corresponding values for the discrete simulations. The relationship between the discrete and the homogeneous discharge values varies slightly around 100%, except for the configurations where the ports are either well connected by fractures or not connected at all.

Table 4.5. Calculated discharges for the discrete and the equivalent homogeneous system.

|	Q_{disc} (m^3 s^{-1})	Q_{hom} (m^3 s^{-1})	Q_{hom}/Q_{disc} (%)
10–20	$2.93 \cdot 10^{-6}$	$2.56 \cdot 10^{-6}$	87.5
9–19	$2.35 \cdot 10^{-6}$	$2.39 \cdot 10^{-6}$	101.8
8–18	$2.37 \cdot 10^{-6}$	$2.10 \cdot 10^{-6}$	88.6
7–17	$1.62 \cdot 10^{-6}$	$1.84 \cdot 10^{-6}$	113.1
6–16	$2.04 \cdot 10^{-6}$	$1.67 \cdot 10^{-6}$	81.7
5–15	$1.77 \cdot 10^{-6}$	$1.62 \cdot 10^{-6}$	91.6
4–14	$1.56 \cdot 10^{-6}$	$1.69 \cdot 10^{-6}$	108.8
3–13	$1.32 \cdot 10^{-6}$	$1.88 \cdot 10^{-6}$	143.0
2–12	$2.24 \cdot 10^{-6}$	$2.16 \cdot 10^{-6}$	96.5
1–11	$3.96 \cdot 10^{-6}$	$2.44 \cdot 10^{-6}$	61.7

4.3.3.2 Transport Parameters

To determinie the equivalent transport parameters, porosity and dispersion tensor (i.e. dispersivities) according to Sects. 2.5.5.2 and 2.5.5.3, a transport calculation is performed for all 10 port configurations, analogously to the flow simulation. At the inflow boundary, unit concentration is imposed until 30 ml tracer have entered the domain. The time is dependent on the discharge as shown in Table 4.6. At the opposite boundary, a free-flow boundary is applied, allowing the concentration to be observed.

Table 4.6. Injection times for the tracer.

	Q_{disc} (m^3 s^{-1})	t (s)		Q_{disc} (m^3 s^{-1})	t (s)
10-20	$2.93 \cdot 10^{-6}$	10.3	5-15	$1.77 \cdot 10^{-6}$	17.0
9-19	$2.35 \cdot 10^{-6}$	12.8	4-14	$1.56 \cdot 10^{-6}$	19.3
8-18	$2.37 \cdot 10^{-6}$	12.7	3-13	$1.32 \cdot 10^{-6}$	22.8
7-17	$1.62 \cdot 10^{-6}$	18.5	2-12	$2.24 \cdot 10^{-6}$	13.4
6-16	$2.04 \cdot 10^{-6}$	14.7	1-11	$3.96 \cdot 10^{-6}$	7.6

Figure 4.53 presents the determined dispersion tensor together with the corresponding values. The mean equivalent effective porosity of the homogeneous system is $\overline{n}_e = 0.202$, which is slightly higher than the matrix porosity of the discrete system. This confirms the conclusion drawn in Sect. 4.3.1.5 that the system has a low sensitivity to the fracture porosity due to the small ratio between fracture and matrix volume. The maximum deviation from the mean value is ± 0.02.

The deviations of the simulated dispersion values from the determined dispersion tensor show a behavior similar to the hydraulic conductivity tensor. The deviations vary positively and negatively for the same directions, only they are more pronounced for the dispersion. This indicates that the transport behavior is significantly more sensitive to the system properties than the flow behavior.
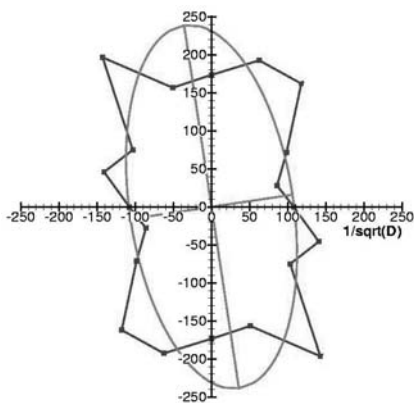
Disp. coeff., xy-system	
D_{xx} (m^2 s^{-1})	$8.52 \cdot 10^{-5}$
D_{xy} (m^2 s^{-1})	$1.02 \cdot 10^{-5}$
D_{yy} (m^2 s^{-1})	$1.87 \cdot 10^{-5}$
Disp. coeff., princ. comp. system	
D_1 (m^2 s^{-1})	$8.67 \cdot 10^{-5}$
D_2 (m^2 s^{-1})	$1.72 \cdot 10^{-5}$
Angle betw. xy- and princ. comp. system	
γ_1	8.6^o
γ_2	-81.4^o
Dispersivities	
α_1 (m)	0.067
α_t (m)	0.013
Mean porosity $\overline{n}_e$ (-)	0.202

Fig. 4.53. Left: Dispersion tensor with calculated values and fitted ellipse with principal components. Right: Resulting equivalent parameters.

4.3.3.3 Summary

Equivalent parameters are determined for hydraulic conductivity, dispersion and porosity, using a fictive data set based on actual data and observations of the chosen cylindrical bench-scale sample. In addition to the results presented above, equivalent parameters are determined for the configurations (5–15), (8–18) and (5–12) (notations are shown in Fig. 4.51), where the last one corresponds to configuration (1–10) in Sects. 4.3.1 and 4.3.2. The flow boundary conditions as well as the transport boundary condition at the outflow boundary remain the same whereas, at the inflow boundary, unit concentration is kept constant throughout the entire simulation. The results are discussed in Sect. 4.3.4.

In Section 4.3.4, the determined equivalent parameters are implemented in a continuum model and the suitability of the multi-continuum approach for simulations on this scale is discussed.

### 4.3.4 Multi-continuum Modeling: Methodology and Approach

T. Vogel, V. Lagendijk, J. Köngeter

Whereas discrete modeling is performed in Sect. 4.3.2 and the effective pa-
rameters are determined in Sect. 4.3.3, this section focuses on the develop-
ment of a multi-continuum model on the cylinder scale. A selection of exper-
imental data and their implementation in the model are presented.

4.3.4.1 Data Preparation

For the various experiments conducted on the cylinder scale (cf. Sect. 4.2),
two types of measurement configurations may be distinguished: first, port-
to-port measurements that allow the detection of local effects, and second,
integral line-to-line measurements, providing information on the averaged
characteristics of the sample.

Taking into account the interface distribution inside the specimen and the
breakthrough curves resulting from the experiments with both a gas and a
tracer, the configurations (port-to-port measurements) situated in the upper
level of the cylinder are selected.
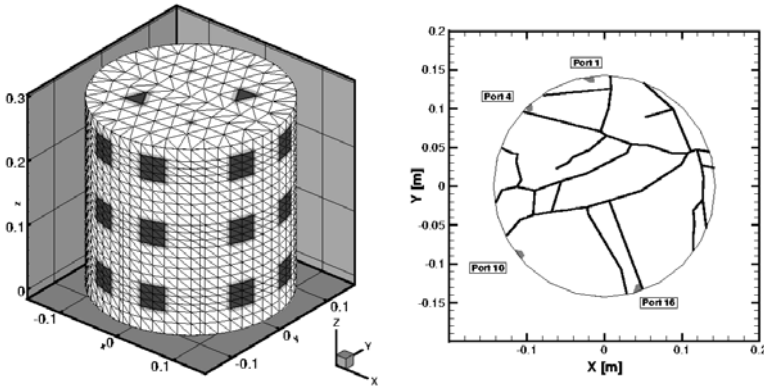
Fig. 4.54. Position of the selected ports; three-dimensional view (left) and view from
the top (right).

Figure 4.54 illustrates the location of the measurement ports as well as
the selected cross-section with the fractures as found on the cylinder surface.
The numerical model is situated at the level of the ports ($z = 0.254\,\text{m}$). The
position of the fractures on the surface of the cylinder shows that, on the
small scale, it is not possible to identify a representative elementary volume
(REV), by means of which the equivalent parameters could be determined
(cf. Sect. 2.5.5).

4.3.4.2 Simulations Concerning the Cylinder

In the following sections, the simulations conducted on the cylinder scale are described and the assumptions are explained.

For the cylinder, the three types of models examined include:

- water with tracer, two-dimensional,
- air with tracer (helium), two-dimensional,
- air with tracer (helium), three-dimensional.

The first series of experiments, *water with tracer*, is an analysis of conceptual character. In the context of this conceptual study, a first approximation of the equivalent parameters for the selected cross-section is determined (cf. Sect. 4.3.3). It has to be pointed out that the equivalent parameters for both flow and transport are identified for the fracture and matrix continua together (not separately). For the analysis of the discrete case, it is not possible to separate the continua as required, since the REV cannot be determined due to the small scale. Therefore, the simulations of the cylinder have a conceptual character. Assuming that the size of the cylinder corresponds to the size of an REV, the multi-continuum simulations are generated for the cylinder. Numerical experiments are conducted with both continuous and temporary infiltration of the tracer.

The method used to obtain the equivalent parameters is presented in Sect. 4.3.3. Figure 4.55 illustrates the discretization and the fractures that can be identified on the top side. It also shows the names of the different sides that are used to identify the different configurations: 5_15 describes a configuration, where side 5 is the input and side 15 the output port. Boundary conditions are applied to the full length of one side (4.5 cm). The cylinder is approximated by a twenty-sided polygon.

The series *Air with tracer (helium), two-dimensional* is performed on the same model as before, but the experimental results are taken into account. A classic single-continuum model, a DPSP model (double-porous, single-permeable) and a DPDP model (double-porous, double-permeable) are set up and different variants are investigated. Boundary conditions are defined according to the experimental design by ports of 35 mm by 35 mm. The location of the ports for certain configurations are presented in Fig. 4.54.

The series *Air with tracer (helium), three-dimensional* is performed by a single-continuum model. The equivalent parameters are determined directly from the experimental results and transferred to the model. The results of the previous two-dimensional studies are taken into account for the parameters of the three-dimensional model. The object of this series is to evaluate the effect of dimensionality. The port configuration is shown in Fig. 4.54 (left).

Figure 4.56 shows the structure of the study. The breakthrough curves presented are used to explain the approach; they do not represent the results. Figure 4.56 suggests that the three different types of model of the cylinder are coupled according to their adaptation. Therefore, an iterative approach is
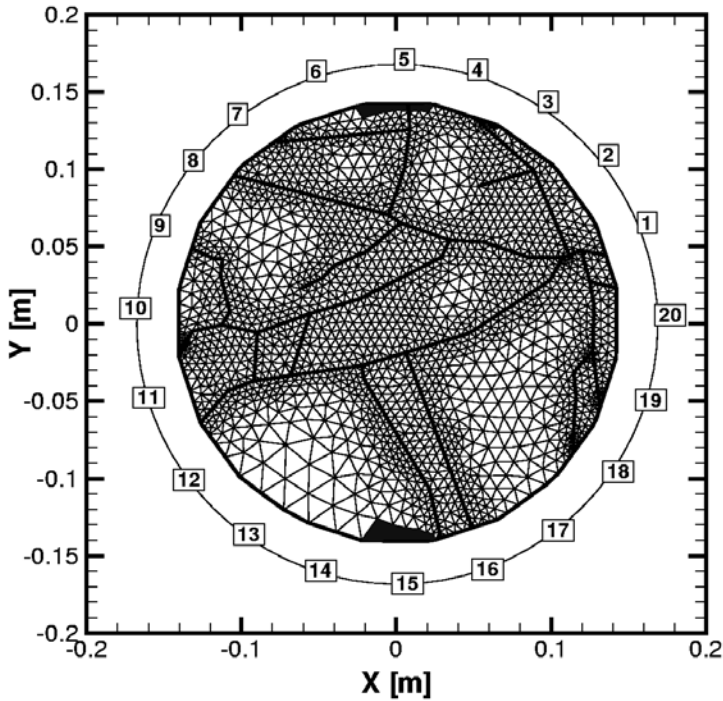
Fig. 4.55. Discretization, side configuration and fracture traces.

chosen. As to the inclusion of the measurements, only data of one configuration (ports 1 and 10) are taken into account at first. The other data are used to evaluate predictional results for the configurations 1_4 and 1_16.

The results of the numerical experiments and the interaction with respect to experimental data and discrete modeling are presented here. Table 4.7 summarizes the characteristic parameters for the double-continuum system of the cylinder. If parameters are varied, the variations are documented in the text.

4.3.4.3 Water with Tracer, Two-Dimensional

The main purpose of this conceptual study is to determine a set of equivalent parameters for multi-continuum modeling. Difficulties arise because neither experimental measurements nor discrete modeling allow the direct separation of the hydraulic components (fracture and matrix). Therefore, equivalent sets of parameters for hydraulic conductivity and dispersivity may only
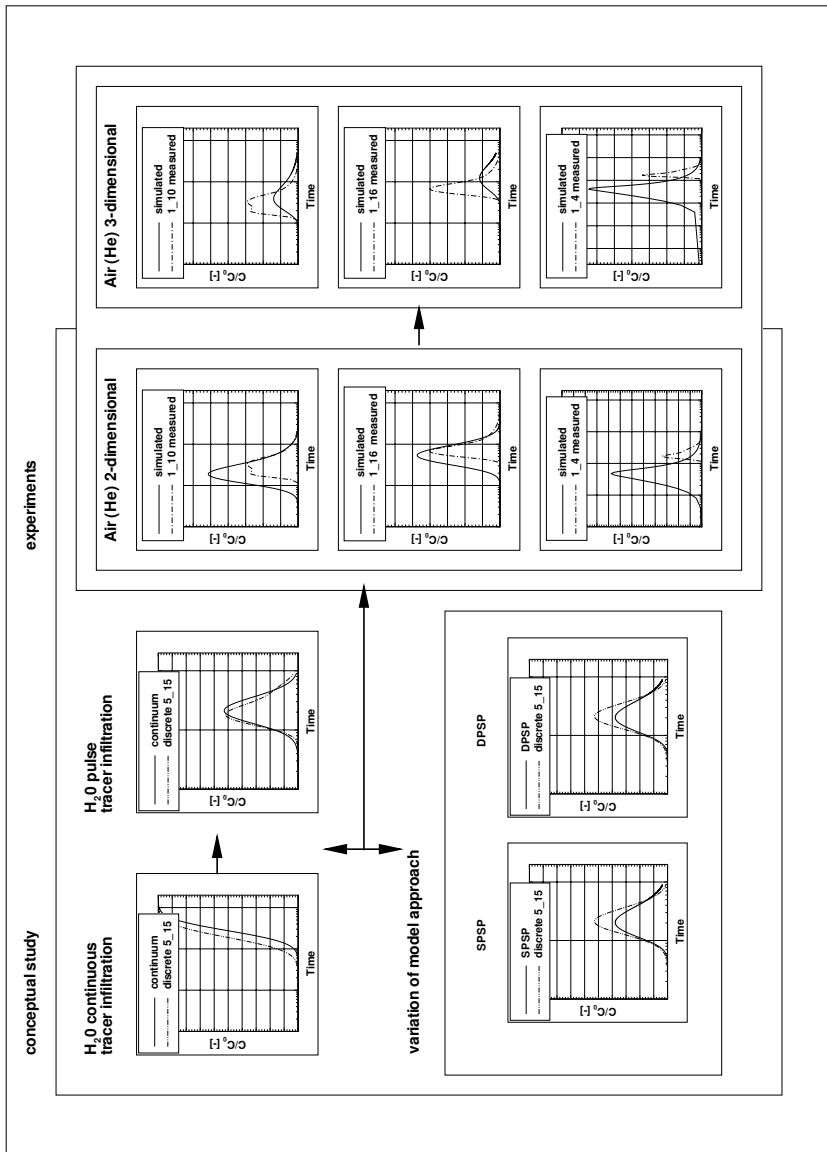
Fig. 4.56. Structure of the cylinder study.

Table 4.7. Characteristic parameters for the double-continuum system of the cylinder.

Equivalent parameters			Fracture	Matrix
Permeability	k_{xx}	(m^2)	$8.02 \cdot 10^{-12}$	$8.02 \cdot 10^{-15}$
	k_{xy}	(m^2)	$1.31 \cdot 10^{-13}$	$1.31 \cdot 10^{-16}$
	k_{yy}	(m^2)	$3.87 \cdot 10^{-12}$	$3.87 \cdot 10^{-15}$
Porosity	n_e	(-)	0.195	0.195
Thickness of the sclice	d_z	(m)	0.05	0.05
Dispersivity				
-longitudinal	α_l	(m)	$4.00 \cdot 10^{-2}$	$4.00 \cdot 10^{-2}$
-transversal horizontal	α_{th}	(m)	$4.00 \cdot 10^{-3}$	$4.00 \cdot 10^{-3}$
Molecular				
Diffusivity coefficient	D_m			
-water		(m^{2}s^{-1})	$4.00 \cdot 10^{-9}$	$4.00 \cdot 10^{-9}$
-gas		(m^{2}s^{-1})	$4.00 \cdot 10^{-6}$	$4.00 \cdot 10^{-6}$
exchange parameters				
Max. penetration depth	s_{max}	(m)	0.08	
Specific surface	Ω_0	(m^{-1})	52.47	
Specific fracture surface	$\Omega_{W,xx}$	(m^{-1})	17.58	
	$\Omega_{W,xy}$	(m^{-1})	0.59	
	$\Omega_{W,yy}$	(m^{-1})	15.82	
Shape factor	ϵ	(-)	2.00	
Exchange coefficient	α_c	(m^2/s)	$1.76 \cdot 10^{-6}$	

be determined for the complete model. As described in Sect. 4.3.3, the directional hydraulic conductivities are determined using a discrete model.
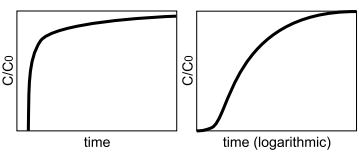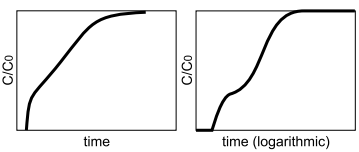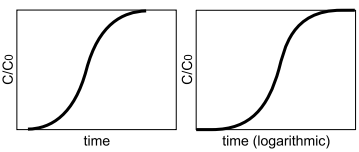
Continuous Tracer Infiltration

In order to identify the type of multi-continuum model, transport simulations with continuous tracer injection are performed. The mobility number N_M (cf. Sect. 2.5.6.1) is defined as the ratio of the equivalent flow velocities of the subordinate component, β, to the superordinate component, α. The mobility number allows for a characterization of the coupled components with respect to the mobility of the fluid in the subordinate component, β, and is therefore decisive for storage or mobility models:

$$N_M = \frac{q_\beta}{q_\alpha} \ . \tag{4.1}$$

To determine the tensor of equivalent hydraulic conductivities, a ratio of $q_\beta/q_\alpha = 0.001$ is assumed. The loss of identity length, L^*, in Table 4.8 represents a characteristic length scale for estimating the transport distance for

which a differentiation between the two components is necessary. A detailed discussion of the characteristic values can be found in Sect. 2.5.5. The importance of the dependency of the model type and the scale is shown, for example, by Teutsch and Sauter (1992).

Table 4.8. Characteristic tracer breakthrough curves for double continuum models (Jansen, 1999).

Shape of the breakthrough curve		Characteristic values	Exchange model
(C/Co vs. time)	(C/Co vs. time (logarithmic))	$N_M \leq 0.001$ and $L^* > 1$	DPSP
(C/Co vs. time)	(C/Co vs. time (logarithmic))	$0.001 \leq N_M \leq 0.5$ and $L^* > 1$	DPDP
(C/Co vs. time)	(C/Co vs. time (logarithmic))	$N_M \geq 0.5$ and $L^* \leq 1$	SPSP

A rough calculation of the loss of identity length shows that the transport distance in the cylinder (maximum of 0.286 m) is less than the loss of the determined identity length. Therefore, a distinction of the continua is not necessary. Despite this calculation, the identification is performed by means of describing the breakthrough curve. Allowing a characterization of the breakthrough curves of configuration 5_15 (Fig. 4.57) by means of Table 4.8, a DPSP model may be determined for the linear projection, whereas a SPSP model may be identified when the logarithmic figure is regarded. However, the identification should be independent of the choice of diagram. It is preferable to place the logarithmic scale on the time axis.

The investigations related to the SPSP model are presented, and the results of the simulations with continuous injection are shown in Figs. 4.57 and 4.58 for different porosities. The other parameters are identical to those summarized in Table 4.7. A good approximation concerning the discrete sim-

ulations is obtained for a porosity of $\bar{n}_e = 0.195$. The calibrated porosity is almost equal to the porosity obtained using the discrete model ($\bar{n}_e = 0.202$).

In the following sections, the breakthrough curves are presented on a linear scale. If, however, a logarithmic scale yields for a better visualization, it is chosen and mentioned explicitly.

Figure 4.59 shows the results for a variation of exchange parameters if a double-porous single-permeable model (DPSP) is used. A transient exchange
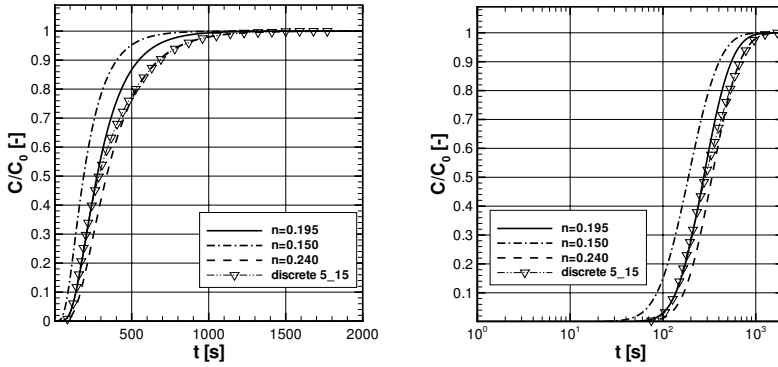

Fig. 4.57. Tracer breakthrough curves for continuous tracer injection; port-to-port connection 5_15; linear time scale (left), logarithmic time scale (right).
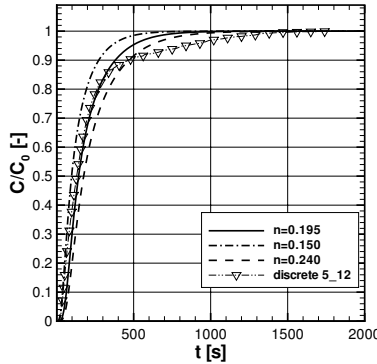

Fig. 4.58. Tracer breakthrough curves for continuous tracer injection; port-to-port connection 5
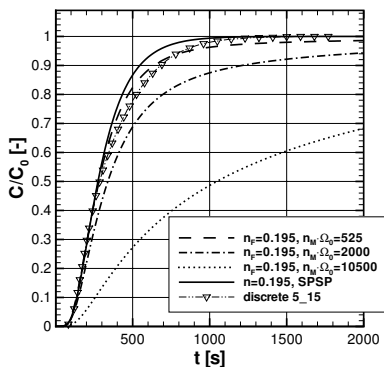
Fig. 4.59. Variation of exchange parameters for the DPSP model.

formulation is applied to the multi-continuum model (cf. Sect. 2.5.3). As a steady-state flow field is assumed for this series of experiments, there is no local fluid exchange between the components. Therefore, only diffusive exchange processes and related parameters must be considered to understand their influence on the exchange between the continua. The initial value of the specific surface Ω_0 is obtained from geometric considerations and is determined to be equal to $52.47\,\mathrm{m}^{-1}$. The estimated matrix porosity is set to 20 %. The influence of the storage medium can clearly be seen in Fig. 4.59. If the specific surface or the matrix porosity is reduced, the intensity of mass transfer between the components is reduced and the results show a good approximation of the discrete simulation for a value of $n_M \cdot \Omega_0 = 525$. This would be comparable to a matrix porosity of 20 % and a specific surface of $10\,\mathrm{m}^{-1}$. The comparison with the single-porous single-permeable model shows that deviations occur only after 200 s. In contrast to the SPSP solution, the DPSP approach falls short of the discrete solution for late time steps. The storage effect of the matrix component is overestimated by the DPSP model. The studies with continuous tracer injection indicate that the SPSP model is the continuum model which is more suitable for the examined cylinder.

Limited Tracer Infiltration

In analogy to the experiments conducted on the cylinder scale, transport analyses with limited tracer injection are made. For these studies, there is a pressure at the input of 116 300 Pa (Dirichlet boundary condition) and, at the outlet, the discharge is set as specified by the discrete model (Neumann boundary condition). The duration of the tracer injection is set in such a way that the total volume injected equals 30 ml.

With the results of the studies with continuous tracer injection in mind, for the following analyses with limited tracer injection the SPSP model is considered first.
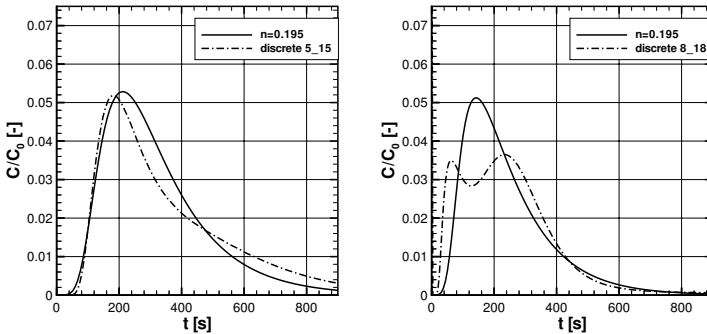
Fig. 4.60. Tracer-breakthrough curves for limited tracer injection; port-to-port connections 5_15 (left) and 8_18 (right).

In Fig. 4.60, the results of the continuum simulation for the configurations 5_15 and 8_18 are compared to the results of the discrete calculations by means of breakthrough curves. For both configurations, the time of the first increase in concentration calculated by the model mimics the one found in the discrete calculations. The maximum of configuration 5_15 nearly coincides with the one of the discrete calculations. The greatest deviations occur in the tailing. In configuration 8_18, the double peak cannot be modeled as determined in the discrete calculations. However, the average of both curves shows a good match.

Configuration 8_18 is presented here because it demonstrates the difficulties encountered in homogenizing the cylinder specimen. Figure 4.61 presents the distribution of the relative concentration calculated by means of the discrete model for three points in time. The first time, $t = 60$ s, is the time at which the first maximum occurs in the breakthrough curve (Fig. 4.60). The point in time $t = 120$ s corresponds to the local minimum, and the next time, $t = 200$ s, lies just before the second maximum of the breakthrough curve. This illustration makes it obvious that the double peak of configuration 8_18 originates from discrete local effects rather than from the interaction of two heterogenous components. Figure 4.62 illustrates the breakthrough curves of configuration 10_20, which contains a continuous fracture connecting the two ports, for both discrete and continuum modeling. As already observed for configuration 5_15, the two curves match very well. Only the time of maximum concentration appears to lag a little in the continuum simulation.
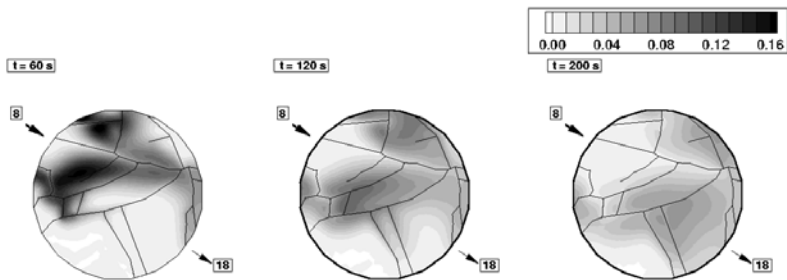
Fig. 4.61. Distribution of relative concentration for limited tracer infiltration; side 8_18.
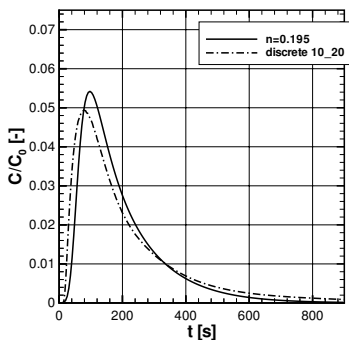
Fig. 4.62. Breakthrough curves for limited tracer infiltration; side: 10_20.

Finally, a DPSP approach with limited tracer injection is compared to the SPSP results presented. The comparison is made exemplarily for configuration 5_15, as illustrated in Fig. 4.63. The parameters required to formulate the component interaction have been chosen according to the results of the studies with continuous tracer injection, i.e. a matrix porosity of 20 % and a specific surface of $10\,\mathrm{m}^{-1}$. The storage effect of the matrix is clearly overestimated in this approach, which results in a reduced maximum of the relative concentration. Due to the high storage effect of the rock matrix, the tailing determined by means of the DPSP approach is longer and goes beyond the range displayed in Fig. 4.63.

Remarks

The studies on *water with tracer* on the cylinder scale demonstrate that homogenization is only possible in some cases. The numerical analysis shows that the SPSP approach gives the best results for the kind of problem with a
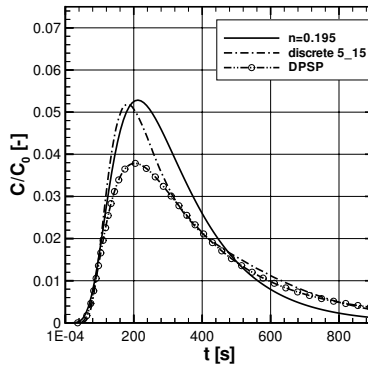
Fig. 4.63. Tracer-breakthrough curves for limited tracer injection; comparison of SPSP and DPSP model; side: 5_15.

two-dimensional model chosen here. It has to be considered, however, that for the superordinate continuum, equivalent parameters taking into account the flow and transport characteristics of the rock matrix are specified. On the present scale, it is impossible to undertake a distinct typing. Further investigations transferring the fracture patterns of the cylinder to a larger area could help determine separate equivalent parameters and thus lead to better continuum modeling.

4.3.4.4 Air with Tracer (Helium), Two-Dimensional

In the following section, the results of the experiments *air with tracer (Helium), two-dimensional* are presented. The model is developed on the basis of the results of the previous section, and the analysis is made by means of a single continuum model. The equivalent parameters are listed in Table 4.7. The molecular diffusion for air as the transport medium is orders of magnitude higher than for water (cf. Table 4.7). The density is assumed to be 1.0 kg m^{-3}, and the dynamic viscosity is $1.814 \cdot 10^{-5}$ m^{2}s^{-1}.

The results are analyzed by means of breakthrough curves. The tracer breakthrough curves determined experimentally all show a recovery rate of less than 90 % after 800 s of measurement (cf. Table 4.9). Therefore, the comparison of the numerical analysis and the experimental results is made by means of an unmodified breakthrough curve and one scaled to 100 % respectively. The amount of tracer that has passed the outlet at $t = 800$ s in the numerical simulations can be retrieved from Table 4.9. For sufficiently long observation periods ($t > 2\,000$ s), the numerical model gives recovery rates of 100 %.

Table 4.9. Recovery rates for the selected configurations after 800 s.

Configuration	Experiment (%)	Model (%)
1_10	73.60	90.99
1_16	80.70	93.44
1_4	66.20	89.60

The selected configurations (cf. Fig. 4.54) are all located on the same level. In analogy to the studies of *water with tracer*, the two-dimensional model is taken as a slice with a thickness of 5 cm situated on the level of the port centers.

The results of the two-dimensional modeling are presented in Figs. 4.64 and 4.65. The single-continuum simulations are carried out with a porosity of 19.5 % and 24.0 %. Qualitatively, the breakthrough curves for the port connections 1_10 and 1_16 correspond well with the curves determined experimentally. As previously observed for configuration 8_18 (cf. Sect. 4.3.4.3), the double peak determined in the experiments for configuration 1_10 cannot be modeled with a single-continuum model. Here as well, the double peak results from local effects (splitting of the transport paths along the fractures) rather than from the interaction of the sub- and superordinate component. For all configurations, the transport signal is detected earlier in the numerical analyses than in the experiments. The largest deviations occur for configuration 1_4. However, it seems to be unrealistic for the distance between ports 1 and 4 that the signal occurs after only 11.5 s. If the curve is displaced, a good qualitative correspondence is reached for this configuration as well.

Remarks

The comparison of the results of the single continuum model for *air with tracer (helium)* with the experiments shows that the transport behavior is qualitatively well reproduced. A comparison of the two-dimensional model with the three-dimensional continuum model (cf. Sect. 4.3.4.5) indicates that the dimensionality has a considerable impact on the results for the geometry studied here. The assumption of the thickness available for the two-dimensional model has a crucial influence on the behavior of the flow and transport of the modeled system.

4.3.4.5 Air with Tracer (Helium), Three-Dimensional

To evaluate the influence of the dimensionality, a three-dimensional model is developed for the studies on *air with tracer (helium)*. The characteristic parameters are listed in Table 4.7. The permeability in the vertical direction k_{zz}
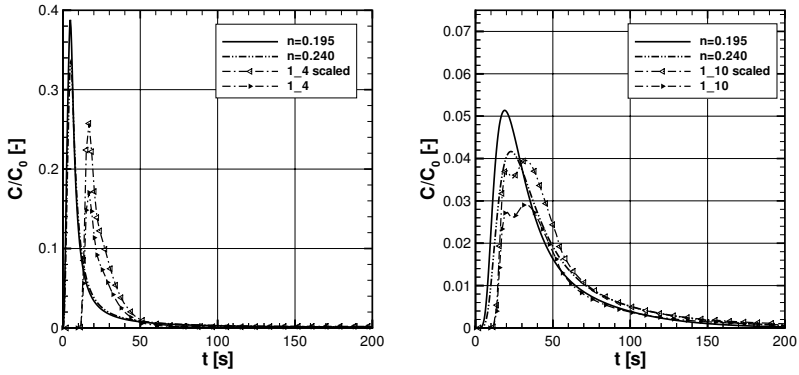
Fig. 4.64. Tracer-breakthrough curves for port-to-port connections 1_4 (left) and 1_10 (right), measured curves scaled and unchanged.
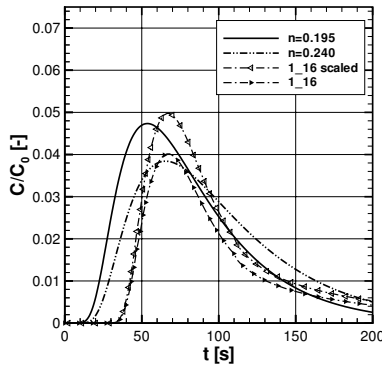
Fig. 4.65. Tracer-breakthrough curves for port-to-port connection 1_16, measured curves scaled and unchanged.

is assumed to be equal to k_{yy}. Furthermore, it is presumed that the z-axis corresponds to a principal axis of the permeability tensor, so that the additional entries on the secondary diagonals are equal to zero.

For the simulation of the flow, Fig. 4.66 contrasts the pressure distribution of the three-dimensional model with the results for two configurations of the two-dimensional model. For the given discharge and inlet pressure, a minimal pressure of 113 086 Pa is reached at the outlet of the two-dimensional model, for which a thickness of $dz = 5$ cm has been assumed. For the three-dimensional model, a pressure of 115 177 Pa is determined.

Thus, in the three-dimensional model the thickness of the region used by the flow is bigger than assumed for the two-dimensional model. To verify this, a second two-dimensional calculation is conducted, and the thickness is assumed to be $dz = 15$ cm. For this second configuration, a minimum pressure of 115229 Pa is determined for the outlet of the two-dimensional model (cf. Figs. 4.66 b and d). In addition to the pressure distributions, Figs. 4.66 a-d present streamlines to illustrate the flow paths. The differences between the three-dimensional model and the two-dimensional model are due to the illustration, as Fig. 4.66 b is a top view of the three-dimensional diagram.
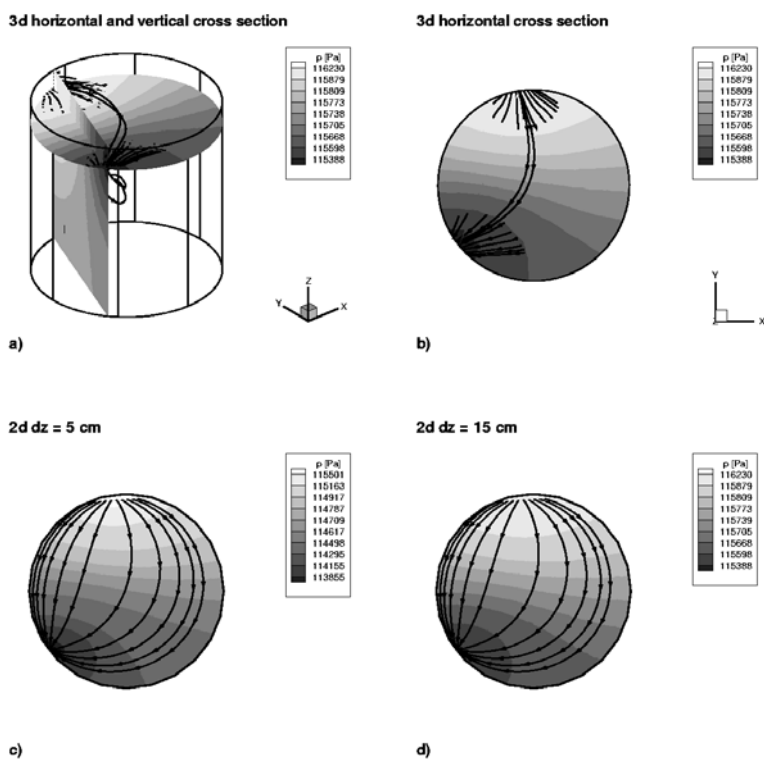
Fig. 4.66. Pressure distributions and stream lines for the 3d-model, compared to the 2d-model.

The results of the three-dimensional transport simulations for the cylinder are compared to those of the two-dimensional model with a thickness of $dz = 5$ cm. Increasing the thickness for the two-dimensional model would, in conjunction with a present amount of injected tracer, imply an injection distributed over the height, which would lead to an unrealistic test arrange-

ment. This model set-up would correspond to the line-to-line measurements (cf. Sect. 4.2).

The results of the transport calculations for port connections 1_4 and 1_10 conducted with the three-dimensional model are illustrated in Fig. 4.67. In contrast to the previous breakthrough curves, a logarithmic scale is chosen for the time axis of these figures in order to enable a definite differentiation. The influence of dimensionality is less evident for the short distance between ports 1 and 4 than for the longer connection 1_10. For configuration 1_10, the point in time in the experiments at which the maximum occurs is reproduced better by the three-dimensional model. However, the intermediate storage of tracer is overestimated, so that the maximum is too small and the following tailing is longer than observed in the experiment.
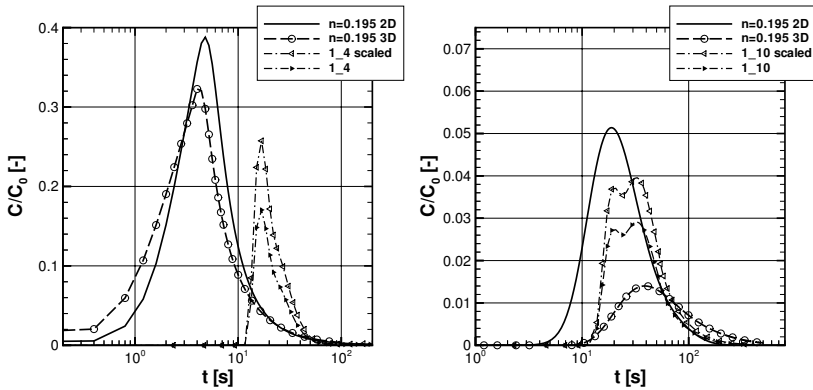
Fig. 4.67. Tracer-breakthrough curves for port-to-port connections 1_4 (left) and 1_10 (right), 3d-calculations with circle, measured curves scaled and unchanged, t logarithmic.

In addition to the determination of the equivalent permeabilities by means of the discrete model (cf. Sect. 4.3.3), one set of parameters is calculated directly from the series of permeability measurements in McDermott (1999) and is referred to as He2MS44. The values of the tensors employed are presented in Table 4.10, and the resulting ellipsoids are illustrated in Fig. 4.68.

The order of magnitude of the permeabilities determined using the two-dimensional discrete model corresponds well with the directional permeabilities obtained from the experiments. The assumption that the vertical axis is a principal axis of the permeability tensor is not confirmed by the experiments. However, a comparison of the results of the transport calculations (cf. Fig. 4.69) shows that the "incorrect" assumption has only a minor influence on the experimental set-up orientated horizontally.
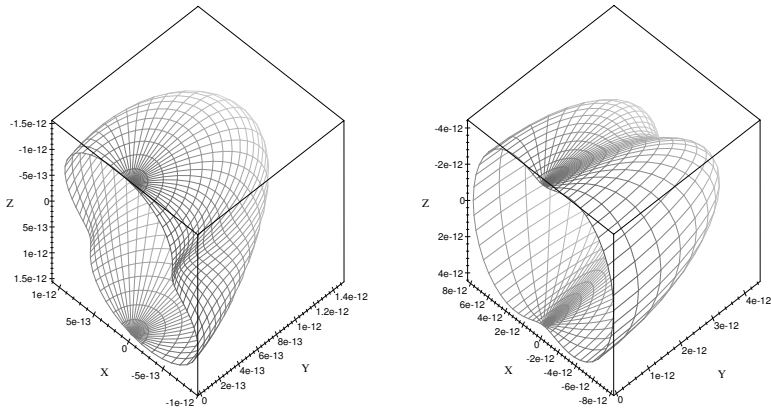
Fig. 4.68. Optimized K-tensors from the experiments (left) and from the discrete modeling with assumptions for the vertical direction (right).
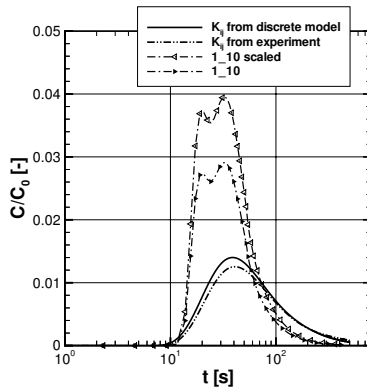

Fig. 4.69. Breakthrough curves for port-to-port connection 1_10; measured curves scaled and unchanged.

Table 4.10. Comparison of the equivalent permeabilities.

	Series He2MS44	Discrete model
k_{xx} (m^2)	$6.98 \cdot 10^{-13}$	$8.02 \cdot 10^{-12}$
k_{xy} (m^2)	$-2.95 \cdot 10^{-13}$	$1.31 \cdot 10^{-13}$
k_{xz} (m^2)	$-2.41 \cdot 10^{-13}$	0.00
k_{yy} (m^2)	$1.42 \cdot 10^{-12}$	$3.87 \cdot 10^{-12}$
k_{yz} (m^2)	$1.50 \cdot 10^{-14}$	0.00
k_{zz} (m^2)	$1.46 \cdot 10^{-12}$	$3.87 \cdot 10^{-12}$

4.3.4.6 Summary

The selection of an appropriate multi-continuum model is complicated by the fact that the experimental data does not allow for a separation of possible continua (e.g. macro-fractures, micro-fractures and host matrix). However, in conjunction with discrete modeling, parameter sets may be determined that allow the development of a multi-continuum model. This model is based on experimental data, discrete modeling and conceptual studies. Thus, a qualitatively good model of the cylindrical core is obtained. The investigations show that local effects may not be reproduced, as the scale of investigation is too small for a multi-continuum model.

Effects of dimensionality are discussed, emphasizing the importance of determining an adequate model thickness when using only a two-dimensional approach.

4.4 Flow and Transport Experiments Conducted on Laboratory Blocks

C. Leven, R. Brauchler, M. Sauter, G. Teutsch, P. Dietrich

4.4.1 Integral Measuring Configuration

The *integral* measuring configuration is set up to obtain information on the integral system response, i.e., flow and transport parameters are averaged over the matrix and the fracture network. Figure 4.70 shows the measuring set-up used in the laboratory to conduct flow and transport experiments in a one-dimensional flow field. For this set-up all ports on one side are used for injection and all ports on the opposite side for extraction.
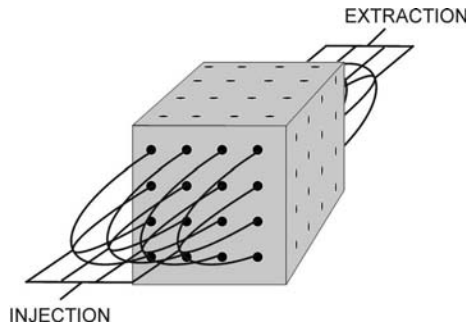
Fig. 4.70. Measuring set-up for the integral flow and transport measurements.

4.4.1.1 The $90 \times 90 \times 80 \, cm^3$-Block

Flow Experiments

Within the laboratory block a steady state flow field is established by ap-
plying a constant injection (p_{in}) and extraction pressure (p_{out} = atmospheric
pressure) and using the experimental setup shown in Fig. 4.25. The pressure
difference between the injection and the extraction side and the flow rate at
the extraction side are measured for each experiment. The data recorded for
this experimental series can be seen in Table 4.11.

On the basis of DARCY's law, a ratio of flow rate Q to pressure difference
Δp scaled by the measuring distance r is used to define a measure for the
conductivity of the block with respect to gas flow. With this ratio, low val-
ues of $Qr/\Delta p$ will indicate low permeabilities since the potential gradient
will be high and the resulting flow rate low for low permeabilities. In turn,
for high permeabilities, like for a single fracture, low pressure gradients and
high flow rates can be expected. In Table 4.11, the ratios are listed for the
three *integral* flow experiments. It is evident that the connection from *bottom*
to *top* has the highest pressure difference and the lowest $Qr/\Delta p$ ratio. In turn,
the lowest pressure difference and highest ratio is found for the connection
from side *III* to *I*.

On the assumption of compressible flow of an ideal gas and the cross-
sectional area of the block as an effective flow-through area A, the perme-

Table 4.11. $90 \times 90 \times 80 \, cm^3$-block: Data from the *integral* pneumatic flow experi-
ments (r - distance, Δp - pressure difference, Q - flow rate).

from	to	r (m)	Δp (mbar)	Q (m^3/s)	$Qr/\Delta p$
III	*I*	0.8	63.8	$8.22 \cdot 10^{-5}$	$1.03 \cdot 10^{-6}$
II	*IV*	0.9	105.9	$6.74 \cdot 10^{-5}$	$5.73 \cdot 10^{-7}$
bottom	*top*	0.9	225.1	$8.57 \cdot 10^{-5}$	$3.43 \cdot 10^{-7}$

ability k for the *integral* measurements can be calculated following Carman (1956):

$$k = \frac{Q}{A} \, \mu_g \left(\frac{2 \, p_{out} \, r}{p_{in}^2 - p_{out}^2} \right) \tag{4.2}$$

with μ_g for the dynamic viscosity, p_{in} for the pressure at inlet, and p_{out} for the pressure at outlet, leading to the permeability values listed in Table 4.12. Due to cross bedding, the highest values of permeability and conductivity can be expected in horizontal direction and the highest resistivity to flow in vertical direction. This is indicated by the highest values of permeability for the connections in the horizontal direction (*III-I* and *II-IV*) and the lowest values in the vertical direction (*bottom-top*). Because of the orientation of the main fractures (Sect. 4.1.2.3) the connection *III-I* indicates the best conductance.

Table 4.12. $90 \times 90 \times 80 \, \text{cm}^3$-block: Permeability and conductivity values derived from the one-dimensional flow experiments (K_g - pneumatic conductivity, K_f - hydraulic conductivity).

from	to	k (m^2)	K_g (m/s)	K_f (m/s)
III	I	$2.25 \cdot 10^{-13}$	$1.57 \cdot 10^{-7}$	$2.21 \cdot 10^{-6}$
II	IV	$1.38 \cdot 10^{-13}$	$9.67 \cdot 10^{-8}$	$1.36 \cdot 10^{-6}$
bottom	*top*	$7.92 \cdot 10^{-14}$	$5.54 \cdot 10^{-8}$	$7.78 \cdot 10^{-7}$

Transport Experiments

After the flow field reaches steady state, a volume of 105 ml helium is injected into the system at the injection side via a bypass loop and the tracer breakthrough is recorded at the extraction side as described in Sect. (4.2.1). In Fig. 4.71 the recorded breakthrough curves are shown. The first initial breakthrough is detected for connections *III-I* and *II-IV* after the same time with a slightly stronger concentration increase for connection *II-IV*. The initial breakthrough for the *bottom-top* connection occurs significantly later. Although the highest hydraulic conductivity can be observed for connection *III-I*, the dominant breakthrough, i.e. the time t_{peak} when the maximum concentration is reached, occurs first for connection *II-IV* even though the transport distance is longer. The lowest breakthrough concentrations and velocities are observed for the connection *bottom-top*. The seepage velocities (Fig. 4.71) derived from the dominant breakthrough (t_{peak}) times show corresponding estimates.

Discussion

The *integral* flow and transport investigations described indicate that, for integral measurements, the contribution of the matrix tends to become negligi-
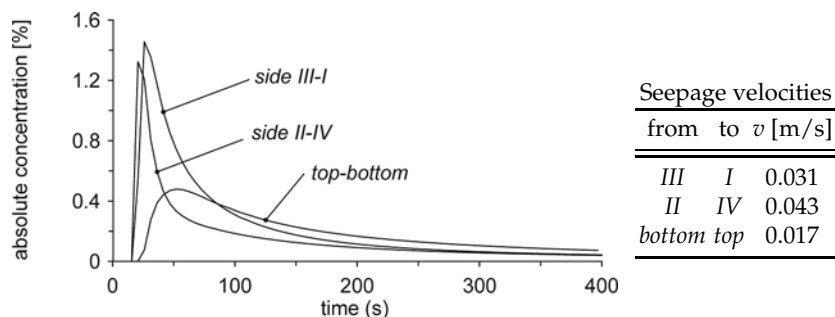
Fig. 4.71. $90 \times 90 \times 80\,\mathrm{cm^3}$-block: Breakthrough curves recorded for the *integral* gas tracer experiments (left). Seepage velocities v derived from the *integral* transport experiments (right).

ble if the integral connections include fractures with high apertures (connections *III-I* and *II-IV*). As described in Sect. 3 (Table 3.8) similar results were found for integral flow experiments with fractured sandstone cores where the contribution of the matrix to the overall conductivity is less than 20% for fracture apertures of less than 40 μm.

The results of the *integral* transport experiments indicate fracture-dominated transport for the connections that include fractures with high apertures. However, a significant influence of the matrix can be observed as indicated by the tailing of the breakthrough curves. The direct injection of tracer into the matrix as well as matrix diffusion processes within the fracture network may be the cause for these observations with integral measuring configurations.

4.4.1.2 The $60 \times 60 \times 60\,\mathrm{cm^3}$-Block

Flow Experiments

As in the case of the experiments described in the previous section (4.4.1.1: 90 x 90 x 80 cm³-block), the *integral* measuring configuration is applied to characterize the $60 \times 60 \times 60\,\mathrm{cm^3}$-block in terms of an integral system response. In Table 4.13, the data recorded for this experimental series are given. The ratio $Qr/\Delta p$ listed in Table 4.13 for all three connections reveals the least resistance to gas flow in the direction *I-III* and the highest resistance in the vertical direction *bottom-top* which is due to the sedimentological cross bedding (cf. Sect. 4.1). Following eq. (4.2), permeability and conductivity values are given for the *integral* measuring configuration in Table 4.14.

Transport Experiments

For this experimental series of transport experiments, the same set-up is used as described above: 105 ml helium is injected via a by-pass loop into the system and the helium breakthrough is recorded at the outlet. The resulting

Table 4.13. $60 \times 60 \times 60\,cm^3$-block: Data from the *integral* pneumatic flow experiments (r - distance, Δp - pressure difference, Q - flow rate).

from	to	r (m)	Δp (mbar)	Q (m³/s)	$Qr/\Delta p$
I	III	0.6	490.0	$4.00 \cdot 10^{-5}$	$4.90 \cdot 10^{-8}$
II	IV	0.6	490.5	$3.23 \cdot 10^{-5}$	$3.94 \cdot 10^{-8}$
bottom	top	0.6	489.5	$1.05 \cdot 10^{-5}$	$1.29 \cdot 10^{-8}$

Table 4.14. $60 \times 60 \times 60\,cm^3$-block: Permeability and hydraulic conductivity values derived from the one-dimensional flow experiments.

from side	to side	intrinsic permeability k (m²)	pneumatic conductivity K_g (m/s)	hydraulic conductivity K_f (m/s)
III	I	$1.99 \cdot 10^{-14}$	$1.10 \cdot 10^{-9}$	$1.95 \cdot 10^{-7}$
II	IV	$1.60 \cdot 10^{-14}$	$8.82 \cdot 10^{-10}$	$1.57 \cdot 10^{-7}$
bottom	top	$5.21 \cdot 10^{-15}$	$2.87 \cdot 10^{-10}$	$5.12 \cdot 10^{-8}$

breakthrough curves are shown in Fig. 4.72. Except for the breakthrough curve of connection *bottom-top*, the breakthrough curves show double peaks and strong tailing. This behavior is assumed to reflect the response of particular parts of the system (e.g. coarse-grain matrix vs. fine-grain matrix, cf. Fig. 4.13). In terms of seepage velocities (Fig. 4.72), the transport behavior is consistent with the derived flow parameters (Table 4.13 and 4.14) with the highest values in horizontal directions (connections *I-III* and *II-IV*).

Seepage velocities		
from	to	v_i (m/s)
I	III	$2.45 \cdot 10^{-3}$
II	IV	$1.15 \cdot 10^{-3}$
top	bottom	$1.71 \cdot 10^{-4}$
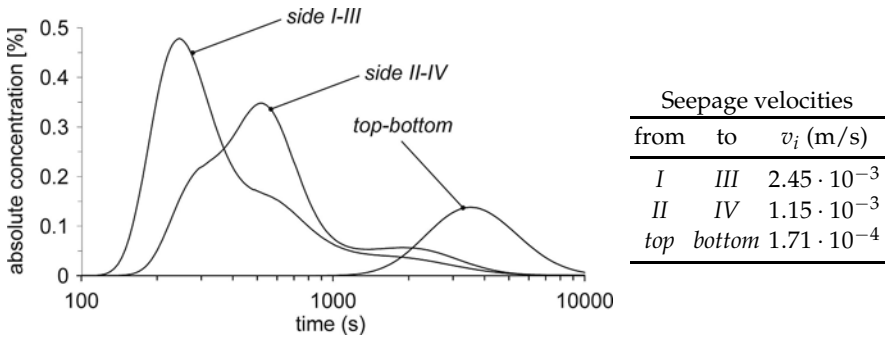
Fig. 4.72. $60 \times 60 \times 60\,cm^3$-block: Breakthrough curves recorded for the *integral* gas tracer experiments (left). Seepage velocities v derived from the *integral* transport experiments (right).

Discussion

The *integral* flow and transport investigations described clearly show the anisotropic flow and transport behavior within the $60 \times 60 \times 60\,cm^3$-block. The *integral* flow experiments clearly indicate the relation between the direction of the experiment with respect to the main axis of the permeability tensor (Fig. 4.73). For the $60 \times 60 \times 60\,cm^3$-block, the permeability vector K_B from Fig. 4.73 corresponds to the direction of connection *I-III* which results in the highest permeability (cf. Table 4.13). In contrast, the lowest permeability is detected by the flow experiments for connection *top-bottom*. This connection would correspond to a direction with an inclination to the permeability vector K_C in Fig. 4.73.
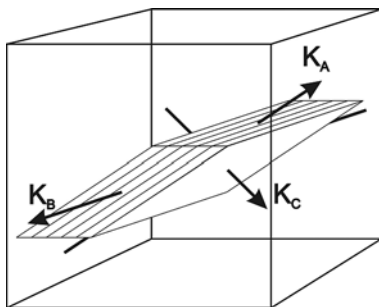
Fig. 4.73. Principle sketch of the $60 \times 60 \times 60\,cm^3$-block oriented with respect to the cross bedding foresets and approximate definition of the three mutually perpendicular permeability components K_A, K_B, and K_C (after Fondeur (1964)).

The results from the *integral* transport experiments yield a more detailed picture of the hydraulic properties. As indicated by the seepage velocities, the same situation as that described for the flow experiments can be concluded if it is assumed that the three determined seepage velocities v are parallel to the principal permeability components. Furthermore, the breakthrough curves with the observed double peaks represent the response of different parts of the systems. A fast response can be interpreted as resulting from flow and transport parallel to the inclination of the cross bedding foresets (connection *I-III* corresponding to the direction of K_B in Fig. 4.73) and the coarse grained matrix located at the top of the $60 \times 60 \times 60\,cm^3$-block (connection *II-IV*). Secondary peaks in the breakthrough curves are interpreted as due to the finer matrix components within the block.

4.4.2 Port-Port Measuring Configuration

For the measuring configuration *port-port*, gas and tracer is injected and extracted at single ports (cf. Sect. 4.1) positioned on opposite block faces. This

configuration allows for a permutation of different port connections and a change in flow-field orientation, thus enabling a tomographical hydraulic investigation of the fractured sandstone block with a very high resolution. By these means, the anisotropy and heterogeneity of parameters relevant to flow and transport relevant parameters can be estimated. The *port-port* configuration is employed to generate three-dimensional flow fields. Figure 4.74 shows an example of one possible port-to-port connection.
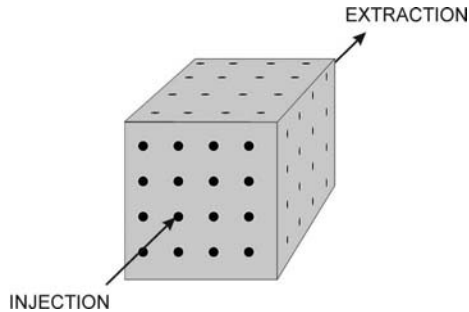

Fig. 4.74. Measuring set-up for the *port-port* measurements.

4.4.2.1 The $90 \times 90 \times 80 \, cm^3$-Block

Flow Experiments

For this type of experiment, the same set-up is used as that shown in Fig. 4.25. From the 47 conducted flow experiments, 26 measurements are connected to matrix-dominated ports while the injection and extraction ports are connected to the matrix on one side and directly to a fracture on the opposite side during a further 8 measurements (Table 4.15). For the remaining measurements, at least one of the ports is connected to a matrix port in the direct vicinity of a fracture (at a distance of less than 20 mm).

To establish a steady state flow field, a constant injection (p_{in}) and extraction pressure (p_{out} = atmospheric pressure) are applied and resulting the flow rate and the pressure difference between injection and extraction port are recorded. The recorded data for these experimental series can be gathered from Table 4.15. According to Sect. 4.4.1.1, a ratio of $Q/\Delta p$ is calculated, providing a measure of the conductivity of the system with respect to gas flow. Low values of $Q/\Delta p$ will indicate low conductivities and vice versa. In Table 4.15, the ratios are given corrected for the measuring distance.

A comparison of the ratios to the type of connection (matrix (*m*), fracture (*f*), or matrix connection in the direct vicinity to a fracture (*fm*)) shows that the lowest ratios arise from *m* connections and highest ratios from *f* or *fm* connections. However, in some cases, unexpected observations are made:

connections that include a direct fracture connection or a connection in the direct vicinity of a fracture reveal small ratios of $Q/\Delta p$ (e.g. connections *316-113*, *t16-b16*, *t13-b13*, *t11-b11*, *210-411*, and *211-410*; cf. Fig. 4.18). This reduction in $Q/\Delta p$ is mainly due to limited fracture lengths. Since the probability of fracture intersections decreases with decreasing fracture length (Long and Witherspoon, 1985), the influence of the fracture system on the resulting flow field will also decrease. In particular, for connections from ports on the *top* to ports on the *bottom* side, the limited length in a vertical direction of the main fracture (Sect. 4.1.2.3) and the restraining function of the horizontal bedding planes come into play.

Generally, as stated by Streltsova (1988), "it is fracture continuity and inter-connectivity, however, not the characteristics of individual fractures that are responsible for the particulars of a fractured reservoir". In Figs. 4.75 and 4.76 the spatial distribution of the ratio $Q/\Delta p$ corrected for the measuring distance is given for sides *I* and *II*. It is evident that the conductivity with respect to gas flow increases in regions in the vicinity of the main fractures (e.g. ports on the far right of side *I* in Fig. 4.75). On the other hand, matrix-dominated regions within the block are indicated by lower values of the ratio $Qr/\Delta p$ (e.g. central region on side *I*).
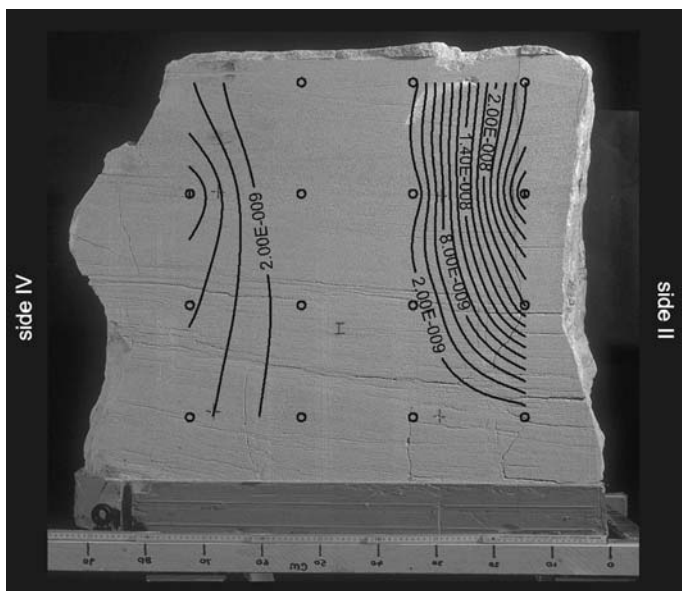

Fig. 4.75. $90 \times 90 \times 80\,\text{cm}^3$-block: Example of spatial distribution of ratio $Qr/\Delta p$ for side *I*.
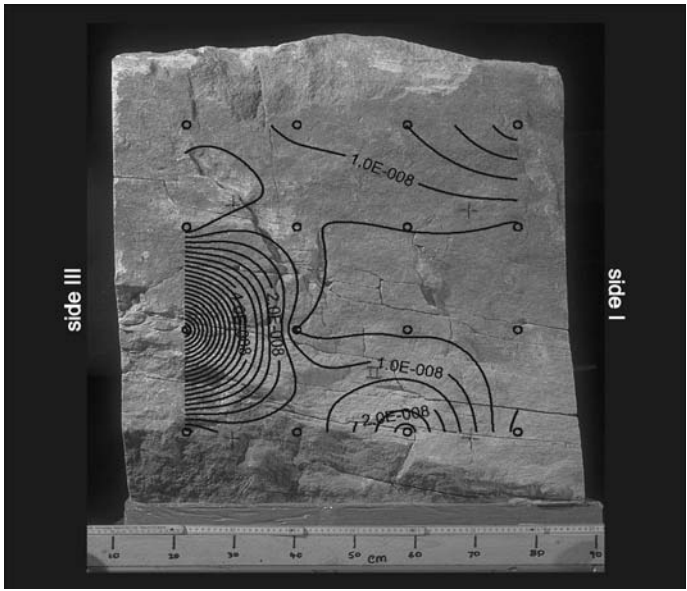
Fig. 4.76. $90 \times 90 \times 80\,\mathrm{cm}^3$-block: Example of spatial distribution of ratio $Qr/\Delta p$ for side *II*.

Table 4.15. $90 \times 90 \times 80\,cm^3$-block: Data from *port-port* flow experiments (m: matrix, f: fracture, fm: fracture in direct vicinity to matrix port). The exact position of the ports can be gathered from Fig. 4.18.

injection - extraction port number	port type (f, m, fm)	pressure difference Δp (mbar)	flow rate Q (m³/s)	distance r (m)	ratio $Qr/\Delta p$
201-404	m-m	302	$3.3 \cdot 10^{-6}$	0.9	$9.8 \cdot 10^{-9}$
202-403	m-m	302	$3.4 \cdot 10^{-6}$	0.9	$1.0 \cdot 10^{-8}$
203-402	m-fm	299	$4.0 \cdot 10^{-6}$	0.9	$1.2 \cdot 10^{-8}$
204-401	f-fm	295	$9.7 \cdot 10^{-6}$	0.9	$3.0 \cdot 10^{-8}$
205-408	m-m	301	$7.1 \cdot 10^{-7}$	0.9	$2.1 \cdot 10^{-9}$
206-407	f-fm	313	$2.3 \cdot 10^{-6}$	0.9	$6.6 \cdot 10^{-9}$
207-406	f-m	303	$1.2 \cdot 10^{-6}$	0.9	$3.6 \cdot 10^{-9}$
208-405	m-m	306	$1.7 \cdot 10^{-6}$	0.9	$4.9 \cdot 10^{-9}$
209-412	fm-fm	300	$3.8 \cdot 10^{-5}$	0.9	$1.1 \cdot 10^{-7}$
210-411	fm-m	300	$6.0 \cdot 10^{-7}$	0.9	$1.8 \cdot 10^{-9}$
211-410	f-m	516	$1.1 \cdot 10^{-6}$	0.9	$2.0 \cdot 10^{-9}$
212-409	m-fm	301	$9.9 \cdot 10^{-7}$	0.9	$3.0 \cdot 10^{-9}$
213-416	m-m	302	$8.1 \cdot 10^{-7}$	0.9	$2.4 \cdot 10^{-9}$
214-415	fm-m	298	$3.2 \cdot 10^{-6}$	0.9	$9.6 \cdot 10^{-9}$
215-414	f-m	303	$1.1 \cdot 10^{-5}$	0.9	$3.1 \cdot 10^{-8}$
216-413	m-m	301	$3.0 \cdot 10^{-7}$	0.9	$9.0 \cdot 10^{-10}$
301-104	m-m	304	$1.4 \cdot 10^{-6}$	0.8	$3.7 \cdot 10^{-9}$
302-103	m-m	300	$5.0 \cdot 10^{-7}$	0.8	$1.3 \cdot 10^{-9}$
303-102	m-m	300	$1.1 \cdot 10^{-6}$	0.8	$3.0 \cdot 10^{-9}$
304-101	f-fm	300	$7.8 \cdot 10^{-6}$	0.8	$2.1 \cdot 10^{-8}$
305-108	m-m	297	$3.4 \cdot 10^{-6}$	0.8	$9.1 \cdot 10^{-9}$
306-107	m-m	306	$4.5 \cdot 10^{-7}$	0.8	$1.2 \cdot 10^{-9}$
307-106	m-m	300	$3.3 \cdot 10^{-8}$	0.8	$8.9 \cdot 10^{-11}$
308-105	f-fm	300	$1.1 \cdot 10^{-5}$	0.8	$3.0 \cdot 10^{-8}$
309-112	m-m	306	$1.6 \cdot 10^{-7}$	0.8	$4.2 \cdot 10^{-10}$
310-111	fm-f	300	$1.1 \cdot 10^{-6}$	0.8	$3.0 \cdot 10^{-9}$
311-110	m-fm	300	$4.8 \cdot 10^{-7}$	0.8	$1.3 \cdot 10^{-9}$
312-109	fm-f	300	$7.4 \cdot 10^{-6}$	0.8	$2.0 \cdot 10^{-8}$
313-116	m-m	306	$8.0 \cdot 10^{-8}$	0.8	$2.1 \cdot 10^{-10}$
314-115	fm-m	307	$2.8 \cdot 10^{-7}$	0.8	$7.3 \cdot 10^{-10}$
315-114	m-f	300	$1.7 \cdot 10^{-6}$	0.8	$4.4 \cdot 10^{-9}$
316-113	m-f	300	$5.0 \cdot 10^{-8}$	0.8	$1.3 \cdot 10^{-10}$

Table 4.15. continued.

| port number	port type	Δp	Q	r	$Qr/\Delta p$
t02-b02	m-m	299	$9.3 \cdot 10^{-7}$	0.9	$2.8 \cdot 10^{-9}$
t03-b03	f-m	296	$4.4 \cdot 10^{-6}$	0.9	$1.4 \cdot 10^{-8}$
t04-b04	m-m	299	$1.6 \cdot 10^{-6}$	0.9	$4.8 \cdot 10^{-9}$
t05-b05	m-m	298	$3.7 \cdot 10^{-6}$	0.9	$1.1 \cdot 10^{-8}$
t06-b06	m-m	300	$2.5 \cdot 10^{-7}$	0.9	$7.4 \cdot 10^{-10}$
t07-b07	m-m	300	$5.8 \cdot 10^{-7}$	0.9	$1.7 \cdot 10^{-9}$
t08-b08	m-m	300	$3.4 \cdot 10^{-7}$	0.9	$1.0 \cdot 10^{-9}$
t09-b09	m-m	295	$1.8 \cdot 10^{-6}$	0.9	$5.5 \cdot 10^{-9}$
t10-b10	m-m	299	$7.9 \cdot 10^{-7}$	0.9	$2.4 \cdot 10^{-9}$
t11-b11	m-f	300	$3.9 \cdot 10^{-7}$	0.9	$1.2 \cdot 10^{-9}$
t12-b12	m-m	301	$2.2 \cdot 10^{-7}$	0.9	$6.5 \cdot 10^{-10}$
t13-b13	f-m	323	$4.0 \cdot 10^{-7}$	0.9	$1.1 \cdot 10^{-9}$
t14-b14	m-m	297	$1.6 \cdot 10^{-7}$	0.9	$4.9 \cdot 10^{-10}$
t15-b15	m-m	299	$4.3 \cdot 10^{-8}$	0.9	$1.3 \cdot 10^{-10}$
t16-b16	f-m	301	$1.4 \cdot 10^{-7}$	0.9	$4.3 \cdot 10^{-10}$

Transport Experiments

As described in Sect. 4.2.4, a certain volume of helium (in this case 105 ml) is injected into the system at the injection port via a bypass loop after the flow field has reached steady state. The tracer breakthrough is recorded at the outlet of the extraction port (Fig. 4.77) using a mass spectrometer. In Fig. 4.77a, the recorded breakthrough curves of all 28 transport experiments are shown. In Fig. 4.77b, the cumulative concentration is given for the same set of breakthrough curves.

Breakthrough curves detected at matrix-dominated port connections are indicated by mainly broad and flat curves in contrast to breakthrough curves recorded at the outlet of direct fracture connections. In this latter case, the initial and dominant breakthrough passes at significantly earlier times with a sharp concentration increase up to the highest maxima. Figure 4.78a gives two examples of tracer breakthrough curves for a fracture- and a matrix-dominated measuring connection. It is obvious that transport experiments with fracture-dominated connections result in much sharper and steeper concentration increases and higher peak concentrations than experiments with matrix-dominated connections. From the absolute values of tracer recovery (Fig. 4.78b) for the given examples, it becomes evident that the tracer recovery of the fracture-dominated connection occurs much faster and with higher absolute values than that of the matrix-dominated connection (in this case, 68% vs. 28%).
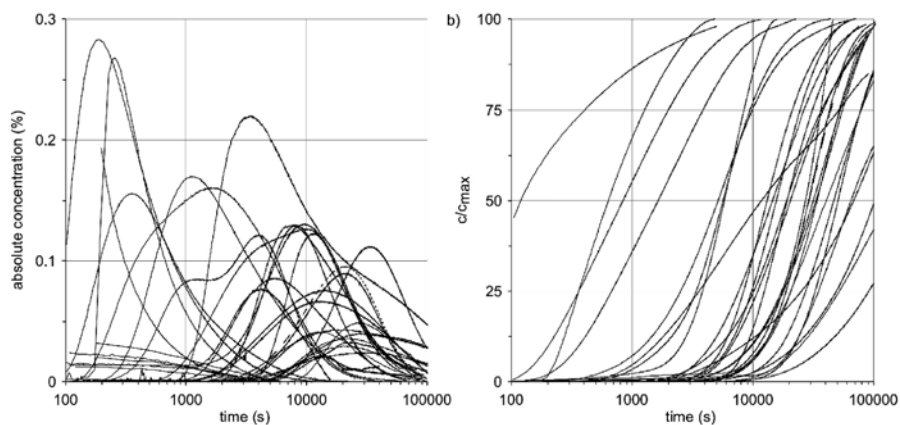
Fig. 4.77. $90 \times 90 \times 80\,cm^3$-block: Breakthrough curves of gas tracer experiments for all *port-port* configurations. a) Breakthrough curves [%]. b) Cumulative concentrations.
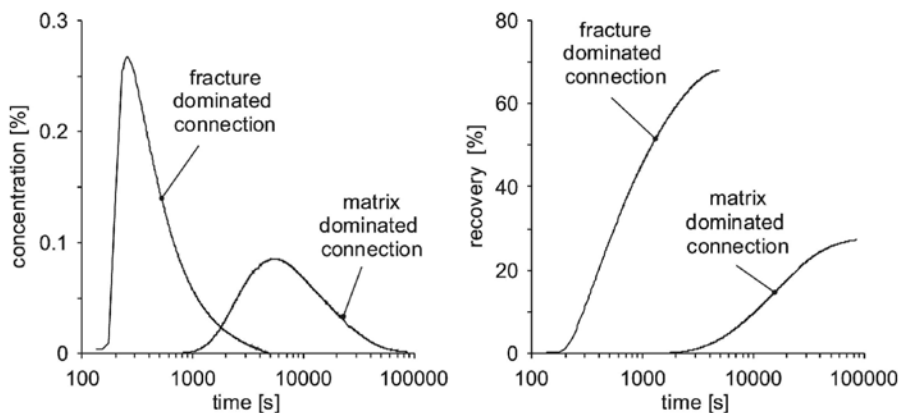
Fig. 4.78. $90 \times 90 \times 80\,cm^3$-block: Comparison of fracture- (connection *308-105*) and matrix-dominated transport (connection *208-405*). a) Tracer breakthrough curves. b) Tracer recovery curves.

However, as Fig. 4.79 shows, there is no clear correlation between the type of connection (e.g. matrix, fracture) and the recovery rate. For mainly matrix-dominated connections, a wide range of recovery rates can be detected (Fig. 4.79b, columns '*m*' and '*f-m*'). It should also be mentioned that the recovery was greater than 100% for 20% of the transport experiments conducted (Fig. 4.79a). This is mainly because of tracer remaining from previous experiments. Therefore, for comparable tracer experiments, the flushing period between consecutive experiments must be long enough to ensure that the amount of remaining tracer is negligible and the initial background concentration has been reached.

a)

Tracer recovery	Relative number [%]
< 25 %	13
25 - 50 %	17
50 - 75 %	23
75 - 100 %	27
> 100 %	20

b)
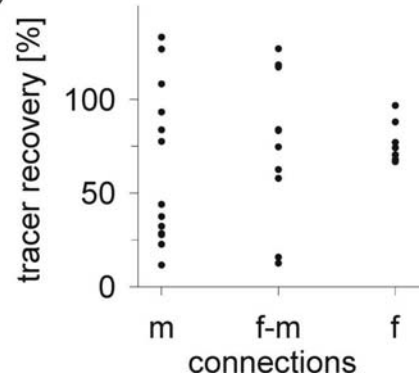
Fig. 4.79. $90 \times 90 \times 80 \, \text{cm}^3$-block: Tracer recovery: a) Relative number of the *port-port* transport experiments with corresponding tracer recovery rates. b) Type of connection versus recovery rates (matrix (m), fracture and matrix (f-m), fracture (f) dominated connections.

An inspection of the breakthrough curves in Fig. 4.77 reveals some other transport phenomena:

- some curves with dominant breakthrough times between $t_{peak} = 1000$ and 10,000 seconds show double peaks with very broad curves.
- some curves show a smooth concentration decrease which can be described as "tailing".
- the plot in Fig. 4.77b indicates an "accumulation" of breakthrough curves at later times.

Table 4.16 lists different breakthrough times ($t_{initial}$, t_{peak}, and t_{median}) and seepage velocities calculated on the basis of the dominant breakthrough time (t_{peak}) for all transport experiments conducted. However, because of limitations of the mass spectrometer, only *port-port* connections are used for the transport experiments with flow rates greater than 50 ml/min.
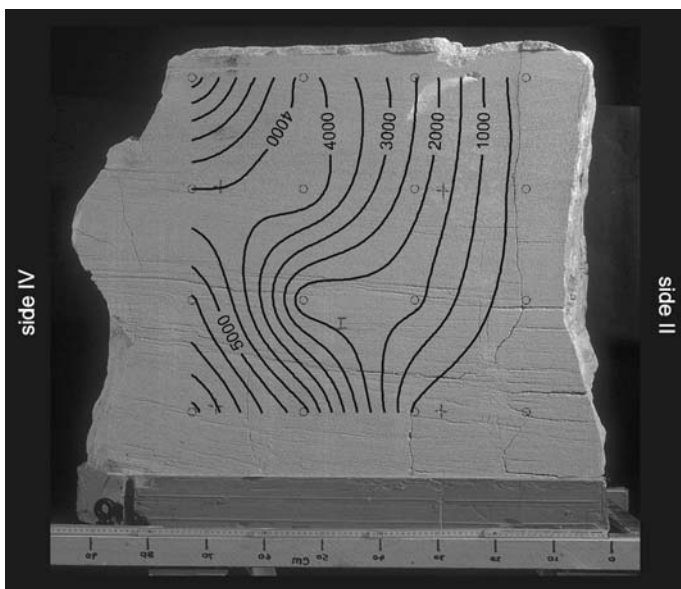
Fig. 4.80. $90 \times 90 \times 80\,\text{cm}^3$-block: Plot of initial tracer breakthrough times recorded for *port-port* connections from side *I* to *III*. The plot shows side *I*.
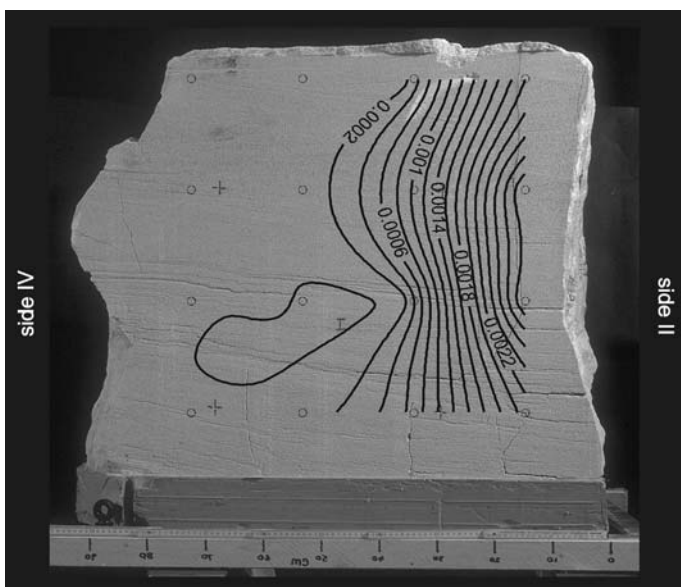
Fig. 4.81. $90 \times 90 \times 80\,\text{cm}^3$-block: Plot of the seepage velocity v recorded for *port-port* connections from side *I* to *III*. The plot shows side *I*.

Fig. 4.82. $90 \times 90 \times 80\,\text{cm}^3$-block: Plot of initial tracer breakthrough times recorded for *port-port* connections from side *II* to *IV*. The plot shows side *II*.
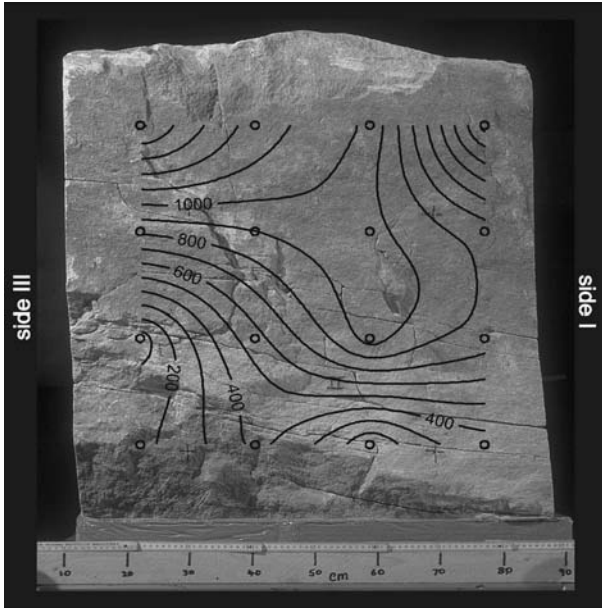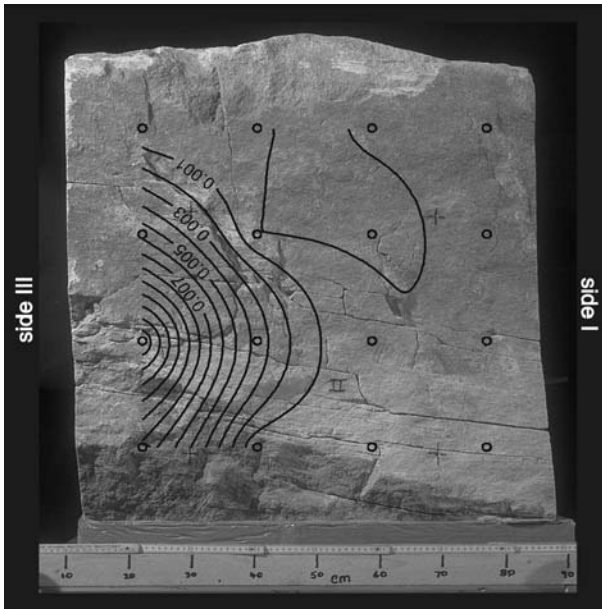

Fig. 4.83. $90 \times 90 \times 80\,\text{cm}^3$-block: Plot of the seepage velocity v recorded for *port-port* connections from side *II* to *IV*. The plot shows side *II*.

Table 4.16. $90 \times 90 \times 80\,\mathrm{cm}^3$-block: Data from *port-port* transport experiments (m: matrix, f: fracture, fm: fracture in direct vicinity to matrix port). The exact position of the ports can be gathered from Fig. 4.18.

injection and extraction port number	port type (f, m, fm)	$t_{initial}$ (s)	t_{peak} (s)	seepage velocity v (m/s)	t_{median} (s)
201-404	m-m	1521	7702	$1.2 \cdot 10^{-4}$	20411
202-403	m-m	1150	9592	$9.4 \cdot 10^{-5}$	15615
203-402	m-fm	975	8207	$1.1 \cdot 10^{-4}$	13084
204-401	f-fm	156	3907	$2.3 \cdot 10^{-4}$	5661
205-408	m-m	1)	1)	1)	1)
206-407	f-fm	900	14387	$6.3 \cdot 10^{-5}$	31620
207-406	f-m	1)	1)	1)	1)
208-405	m-m	751	5550	$1.6 \cdot 10^{-4}$	68221
209-412	fm-fm	52	63	$1.4 \cdot 10^{-2}$	117
210-411	fm-m	1)	1)	1)	1)
211-410	f-m	950	12819	$7.0 \cdot 10^{-5}$	33293
212-409	m-fm	752	3406	$2.6 \cdot 10^{-4}$	68221
213-416	m-m	1)	1)	1)	1)
214-415	fm-m	428	9675	$9.3 \cdot 10^{-5}$	19021
215-414	f-m	104	1608	$5.6 \cdot 10^{-4}$	5145
216-413	m-m	1)	1)	1)	1)
301-104	m-m	1168	4135	$1.9 \cdot 10^{-4}$	5801
302-103	m-m	4184	21871	$3.7 \cdot 10^{-5}$	130614
303-102	m-m	2520	14567	$5.5 \cdot 10^{-5}$	40665
304-101	f-fm	84	362	$2.2 \cdot 10^{-3}$	4040
305-108	m-m	4005	13455	$5.9 \cdot 10^{-5}$	40632
306-107	m-m	4502	22318	$3.6 \cdot 10^{-5}$	46767
307-106	m-m	1)	1)	1)	1)
308-105	f-fm	154	253	$3.2 \cdot 10^{-3}$	635
309-112	m-m	5608	20651	$3.9 \cdot 10^{-5}$	2)
310-111	fm-f	1594	33416	$2.4 \cdot 10^{-5}$	27240
311-110	m-fm	1641	18619	$4.3 \cdot 10^{-5}$	101984
312-109	fm-f	125	247	$3.2 \cdot 10^{-3}$	839
313-116	m-m	7200	26098	$3.1 \cdot 10^{-5}$	64885
314-115	fm-m	4719	18753	$4.3 \cdot 10^{-5}$	33927
315-114	m-f	360	1499	$5.3 \cdot 10^{-4}$	9531
316-113	m-f	1)	1)	1)	1)

Table 4.16. continued.

port number	port type	$t_{initial}$	v	t_{peak}	t_{median}
t02-b02	m-m	1)	1)	1)	1)
t03-b03	f-m	3324	11254	$8.0 \cdot 10^{-5}$	19177
t04-b04	m-m	1)	1)	1)	1)
t05-b05	m-m	1312	20416	$4.4 \cdot 10^{-5}$	29212
t06-b06	m-m	1)	1)	1)	1)
t07-b07	m-m	1)	1)	1)	1)
t08-b08	m-m	1)	1)	1)	1)
t09-b09	m-m	3927	34255	$2.6 \cdot 10^{-5}$	50599
t10-b10	m-m	1)	1)	1)	1)
t11-b11	m-f	1)	1)	1)	1)
t12-b12	m-m	1)	1)	1)	1)
t13-b13	f-m	1)	1)	1)	1)
t14-b14	m-m	1)	1)	1)	1)
t15-b15	m-m	1)	1)	1)	1)
t16-b16	f-m	1)	1)	1)	1)

1) - no breakthrough curve measured

2) - estimation not possible.

Discussion

The phenomena observed in the *port-port* experiments can be interpreted as follows:

- Relatively short breakthrough times with high concentration maxima correspond to a fast transport of the tracer through the fracture system with less pronounced interaction with the porous sandstone matrix.
- The broad and flat breakthrough of tracer reflects transport mainly through the matrix with dominant diffusive and/or dispersive transport mechanisms.
- Several reasons can be given for the tailing in the breakthrough curves:
  - <u>Matrix diffusion</u>: Due to the injection of tracer directly into the fracture network, a concentration gradient between fracture network (higher concentration) and matrix (lower concentration) is established. Following FICK's law, a tracer flux from regions of higher concentration to regions of lower concentration occurs, i.e. from the fracture network to the matrix. After the main tracer mass passes through the fracture network, the concentration within the fractures decreases again. After a certain time, a gradient in the opposite direction is established, i.e. from the matrix to the fracture, and the tracer is released into the

fractures. This process leads to a retarded tracer breakthrough at the observation point, and is typically observed as tailing in the breakthrough curve.

– Differential advection: The dimensionality of the flow field which is assumed to be three-dimensional for the *port-port* connections. As described by McDermott (1999), such tailing can be due to pathways of varying length which are established through the dimensionality of the flow field.

• The occurrence of the double peaks can be due to transport through two or more fractures or combined transport through matrix and fracture network.

4.4.2.2 The $60 \times 60 \times 60\,\mathrm{cm}^3$-Block

Flow Experiments

With the experimental set-up shown in Fig. 4.25, flow experiments are conducted using *port-port* connections as described in Sect. 4.4.2.1. In Table 4.17, the flow rate information recorded during the experiments is presented for all *port-port* connections as well as the ratio $Qr/\Delta p$ which provides a measure for the conductivity of the system with respect to gas flow. In Fig. 4.84, the ratio is plotted for side *II*.

In comparison to the $90 \times 90 \times 80\,\mathrm{cm}^3$-block, the spatial distribution of the ratio reflects the bedding and the matrix composition of the sandstone block in particular. Beyond this, the differences of the absolute values of the ratio are much smaller. Both, indicates that the influence of the fractures is not dominating the system but the structural composition of the matrix plays an important role. The matrix of the sandstone block can be separated in two parts. The upper part consists of a coarser grained matrix while the lower part consists of a finer grained matrix. This classification agrees with the conducted flow experiments. From the 51 flow experiments, 8 measurements were conducted in the upper part of the sandstone block. The recorded flow rates in this region of the sandstone block are up to four times higher than in the finer grained matrix. An influence of the fractures on the flow experiments can not be determined.

Table 4.17. $60 \times 60 \times 60\,\mathrm{cm}^3$-block: Data from *port-port* flow experiments (m: matrix, f′: fissure).

injection extraction port number	port type (f′, m)	pressure difference Δp (mbar)	flow rate Q (m^3/s)	distance r (m)	ratio $Qr/\Delta p$
101-304	m-m	505	$1.40 \cdot 10^{-5}$	0.6	$1.66 \cdot 10^{-8}$

Table 4.17. continued.

port number	port type	Δp	Q	r	$Qr/\Delta p$
102-303	m-m	500	$1.14 \cdot 10^{-5}$	0.6	$1.37 \cdot 10^{-8}$
103-302	m-f′	502	$7.92 \cdot 10^{-6}$	0.6	$9.47 \cdot 10^{-9}$
104-301	m-m	505	$3.65 \cdot 10^{-6}$	0.6	$4.34 \cdot 10^{-9}$
105-308	m-m	502	$7.48 \cdot 10^{-7}$	0.6	$8.94 \cdot 10^{-10}$
106-307	m-m	502	$1.07 \cdot 10^{-6}$	0.6	$1.28 \cdot 10^{-9}$
107-306	m-m	502	$6.77 \cdot 10^{-7}$	0.6	$8.09 \cdot 10^{-10}$
108-305	f′-f′	502	$5.33 \cdot 10^{-7}$	0.6	$6.38 \cdot 10^{-10}$
109-312	m-m	501	$2.83 \cdot 10^{-6}$	0.6	$3.39 \cdot 10^{-9}$
110-311	m-f′	501	$2.17 \cdot 10^{-6}$	0.6	$2.60 \cdot 10^{-9}$
111-310	f′-f′	500	$1.03 \cdot 10^{-6}$	0.6	$1.23 \cdot 10^{-9}$
112-309	f′-m	499	$1.14 \cdot 10^{-6}$	0.6	$1.37 \cdot 10^{-9}$
113-316	m-m	500	$1.92 \cdot 10^{-6}$	0.6	$2.30 \cdot 10^{-9}$
114-315	m-m	499	$2.12 \cdot 10^{-6}$	0.6	$2.54 \cdot 10^{-9}$
115-314	m-m	501	$1.30 \cdot 10^{-6}$	0.6	$1.55 \cdot 10^{-9}$
116-313	m-m	502	$1.03 \cdot 10^{-6}$	0.6	$1.23 \cdot 10^{-9}$
117-317	m-m	490	$1.75 \cdot 10^{-7}$	0.6	$2.14 \cdot 10^{-10}$
201-404	f′-m	506	$5.83 \cdot 10^{-6}$	0.6	$6.92 \cdot 10^{-9}$
202-403	m-m	499	$7.95 \cdot 10^{-6}$	0.6	$9.57 \cdot 10^{-9}$
203-402	m-m	500	$8.75 \cdot 10^{-6}$	0.6	$1.05 \cdot 10^{-8}$
204-401	m-m	500	$6.37 \cdot 10^{-6}$	0.6	$7.65 \cdot 10^{-9}$
205-408	m-m	501	$4.27 \cdot 10^{-7}$	0.6	$5.11 \cdot 10^{-10}$
206-407	m-m	498	$1.11 \cdot 10^{-6}$	0.6	$1.33 \cdot 10^{-9}$
207-406	f′-m	508	$1.10 \cdot 10^{-6}$	0.6	$1.29 \cdot 10^{-9}$
208-405	f′-m	508	$1.17 \cdot 10^{-6}$	0.6	$1.38 \cdot 10^{-9}$
209-412	m-m	504	$1.05 \cdot 10^{-6}$	0.6	$1.25 \cdot 10^{-9}$
210-411	m-m	504	$1.75 \cdot 10^{-6}$	0.6	$2.08 \cdot 10^{-9}$
211-410	m-m	504	$1.75 \cdot 10^{-6}$	0.6	$2.08 \cdot 10^{-9}$
212-409	f′-m	502	$1.06 \cdot 10^{-6}$	0.6	$1.26 \cdot 10^{-9}$
213-416	m-m	500	$1.92 \cdot 10^{-6}$	0.6	$2.30 \cdot 10^{-9}$
214-415	f′-m	500	$1.20 \cdot 10^{-6}$	0.6	$1.44 \cdot 10^{-9}$
215-414	m-m	500	$1.12 \cdot 10^{-6}$	0.6	$1.34 \cdot 10^{-9}$
216-413	m-m	500	$6.83 \cdot 10^{-7}$	0.6	$8.21 \cdot 10^{-10}$
217-417	m-m	503	$4.02 \cdot 10^{-7}$	0.6	$4.79 \cdot 10^{-10}$
b01-t01	m-m	503	$3.42 \cdot 10^{-6}$	0.6	$4.07 \cdot 10^{-9}$
b02-t02	m-f′	502	$2.83 \cdot 10^{-6}$	0.6	$3.39 \cdot 10^{-9}$
b03-t03	m-m	501	$2.13 \cdot 10^{-6}$	0.6	$2.55 \cdot 10^{-9}$
b04-t04	m-m	501	$2.33 \cdot 10^{-6}$	0.6	$2.79 \cdot 10^{-9}$
b05-t05	m-m	500	$2.83 \cdot 10^{-6}$	0.6	$3.40 \cdot 10^{-9}$

Table 4.17. continued.

port number	port type	Δp	Q	r	$Qr/\Delta p$
b06-t06	m-f′	502	$2.08 \cdot 10^{-6}$	0.6	$2.49 \cdot 10^{-9}$
b07-t07	m-m	501	$1.33 \cdot 10^{-6}$	0.6	$1.60 \cdot 10^{-9}$
b08-t08	m-m	502	$1.68 \cdot 10^{-6}$	0.6	$2.01 \cdot 10^{-9}$
b09-t09	m-m	500	$1.57 \cdot 10^{-6}$	0.6	$1.88 \cdot 10^{-9}$
b10-t10	m-m	498	$2.17 \cdot 10^{-6}$	0.6	$2.61 \cdot 10^{-9}$
b11-t11	m-m	497	$2.25 \cdot 10^{-6}$	0.6	$2.71 \cdot 10^{-9}$
b12-t12	m-m	496	$2.92 \cdot 10^{-6}$	0.6	$3.53 \cdot 10^{-9}$
b13-t13	m-m	498	$1.48 \cdot 10^{-6}$	0.6	$1.78 \cdot 10^{-9}$
b14-t14	m-m	497	$1.48 \cdot 10^{-6}$	0.6	$1.78 \cdot 10^{-9}$
b15-t15	m-m	497	$1.40 \cdot 10^{-6}$	0.6	$1.69 \cdot 10^{-9}$
b16-t16	m-m	496	$1.27 \cdot 10^{-6}$	0.6	$1.54 \cdot 10^{-9}$
b17-t17	m-m	495	$1.87 \cdot 10^{-6}$	0.6	$2.26 \cdot 10^{-9}$

Transport Experiments

For the experimental series of transport experiments conducted on the $60 \times 60 \times 60\,cm^3$-block, 105 ml helium is injected into the system and the tracer breakthrough is recorded as described in Sect. 4.2.4. Fig. 4.85a shows breakthrough curves recorded for all 28 transport experiments. In Fig. 4.85b, the cumulative concentration is given for the same set of breakthrough curves. Table 4.18 lists the different breakthrough times ($t_{initial}$, t_{peak}, and t_{median}) and seepage velocities calculated on the basis of the dominant breakthrough time (t_{peak}) for all conducted transport experiments. In Figs. 4.86 and 4.87 plots of the initial breakthrough times and the seepage velocities respectively are given for side *II*.

Breakthrough curves recorded in the coarse grained matrix of the sandstone block are characterized by an initial and dominant breakthrough occurring at significantly earlier times with a sharp concentration increase up to the peak, while the remaining curves are characterized by a more or less broad and flat shape and later initial and dominant breakthrough times. A more detailed investigation of the remaining breakthrough curves indicates that it is not possible alone by means of the shape of the breakthrough curves and the different breakthrough times ($t_{initial}$, t_{peak}, and t_{median}) to determine if the breakthrough is recorded parallel or orthogonal to the bedding. One reason for this is the influence of the boundary condition on the transport behavior. In Sect. 10 a multivariate statistical approach is proposed that allows to distinguish breakthrough curves recorded parallel or orthogonal to the bedding.
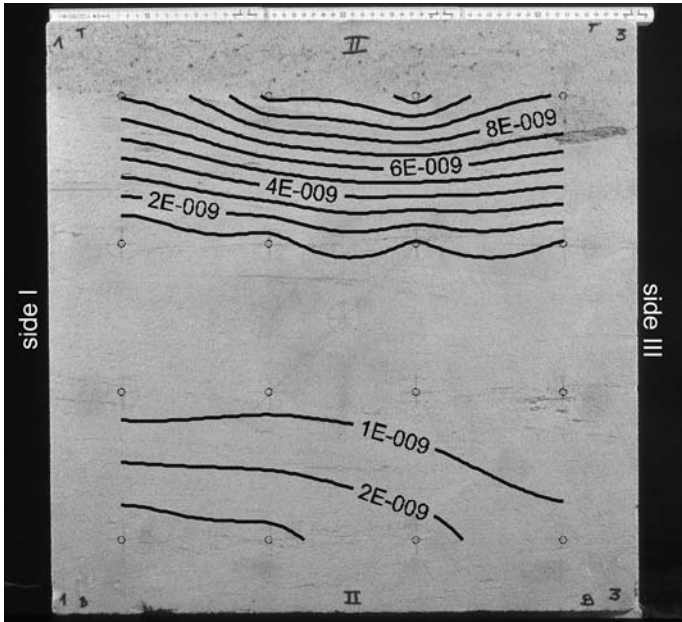
Fig. 4.84. $60 \times 60 \times 60\,\text{cm}^3$-block: Spatial distribution of ratio $Qr/\Delta p$ for side *II*.
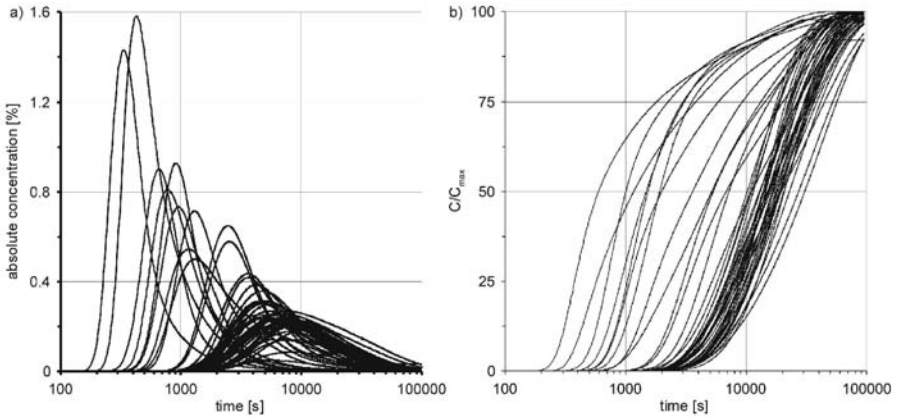

Fig. 4.85. $60 \times 60 \times 60\,\text{cm}^3$-block: Breakthrough curves of gas tracer experiments for all *port-port* configurations. a) Breakthrough curves [%]. b) Cumulative concentrations.
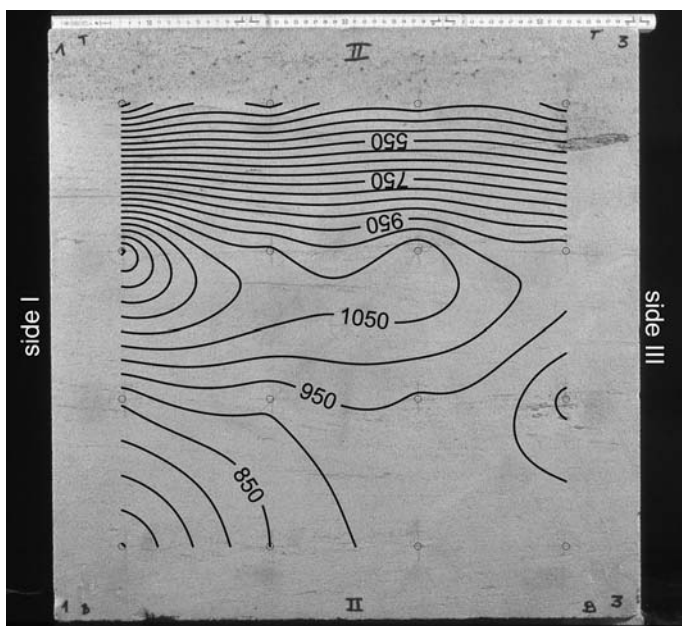
Fig. 4.86. $60 \times 60 \times 60 \,\text{cm}^3$-block: Plot of initial tracer breakthrough times recorded for *port-port* connections from side *II* to *IV*. The plot shows side *II*.
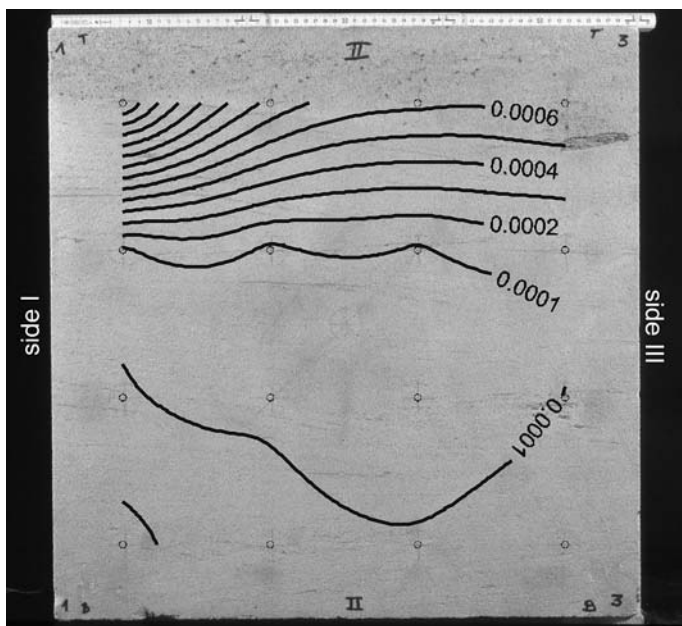

Fig. 4.87. $60 \times 60 \times 60 \,\text{cm}^3$-block: Plot of the seepage velocity v recorded for *port-port* connections from side *II* to *IV*. The plot shows side *II*.

Table 4.18. $60 \times 60 \times 60\,\mathrm{cm}^3$-block: Data from *port-port* transport experiments (m: matrix, f': fissure).

injection and extraction port number	port type (f, m, fm)	$t_{initial}$ (s)	t_{peak} (s)	seepage velocity v (m/s)	t_{median} (s)
101-304	m-m	146	335	$1.79 \cdot 10^{-3}$	594
102-303	m-m	228	654	$9.18 \cdot 10^{-4}$	1007
103-302	m-k	463	1140	$5.26 \cdot 10^{-4}$	1918
104-301	m-m	401	1296	$4.63 \cdot 10^{-4}$	3599
105-308	m-m	872	4373	$1.37 \cdot 10^{-4}$	15195
106-307	m-m	1018	6535	$9.18 \cdot 10^{-5}$	16981
107-306	m-m	991	9279	$6.47 \cdot 10^{-5}$	22825
108-305	k-k	1100	6833	$8.78 \cdot 10^{-5}$	27183
109-312	m-m	400	1316	$4.56 \cdot 10^{-4}$	5176
110-311	m-k	704	4598	$1.30 \cdot 10^{-4}$	10194
111-310	k-k	1188	8783	$6.83 \cdot 10^{-5}$	19320
112-309	k-m	957	5462	$1.10 \cdot 10^{-4}$	15864
113-316	m-m	645	2446	$2.45 \cdot 10^{-4}$	5314
114-315	m-m	834	3573	$1.68 \cdot 10^{-4}$	7183
115-314	m-m	929	4953	$1.21 \cdot 10^{-4}$	12904
116-313	m-m	913	3657	$1.64 \cdot 10^{-4}$	11148
201-404	k-m	180	428	$1.40 \cdot 10^{-3}$	1168
202-404	m-m	280	778	$7.71 \cdot 10^{-4}$	1481
203-402	m-m	365	961	$6.24 \cdot 10^{-4}$	1531
204-401	m-m	315	904	$6.64 \cdot 10^{-4}$	1993
205-408b	m-m	1361	7728	$7.76 \cdot 10^{-5}$	30524
206-407	m-m	1065	8118	$7.39 \cdot 10^{-5}$	18862
207-406	k-m	1100	7037	$8.53 \cdot 10^{-5}$	18705
208-405	k-m	990	4750	$1.26 \cdot 10^{-4}$	17954
209-412	m-m	860	4969	$1.21 \cdot 10^{-4}$	19286
210-411	m-m	910	6438	$9.32 \cdot 10^{-5}$	14067
211-410	m-m	941	7273	$8.25 \cdot 10^{-5}$	15104
212-409	k-m	833	5894	$1.02 \cdot 10^{-4}$	15324
213-416	m-m	646	2561	$2.34 \cdot 10^{-4}$	6818
214-415	k-m	850	4775	$1.26 \cdot 10^{-4}$	14947
215-414	k-k	930	5781	$1.04 \cdot 10^{-4}$	15485
216-413	m-m	950	4264	$1.41 \cdot 10^{-4}$	19576
b01-t01	m-m	840	4430	$1.35 \cdot 10^{-4}$	14100
b02-t02	m-k	840	4974	$1.21 \cdot 10^{-4}$	11071
b03-t03	m-m	910	5915	$1.01 \cdot 10^{-4}$	13756
b04-t04	m-m	940	4336	$1.38 \cdot 10^{-4}$	13066

Table 4.18. continued.

port number	port type	$t_{initial}$	v	t_{peak}	t_{median}
b05-t05	m-m	910	4703	$1.28 \cdot 10^{-4}$	10705
b06-t06	m-k	1200	7910	$7.58 \cdot 10^{-5}$	14488
b07-t07	m-m	1360	10993	$5.46 \cdot 10^{-5}$	20699
b08-t08	m-m	973	6939	$8.65 \cdot 10^{-5}$	17586
b09-t09	m-m	1220	8672	$6.92 \cdot 10^{-5}$	18854
b10-t10	m-m	1150	9185	$6.53 \cdot 10^{-5}$	14415
b11-t11	m-m	1170	8756	$6.85 \cdot 10^{-5}$	13787
b12-t12	m-m	1140	5737	$1.05 \cdot 10^{-4}$	11468
b13-t13	m-m	1143	6572	$9.13 \cdot 10^{-5}$	16347
b14-t14	m-m	1263	8506	$7.05 \cdot 10^{-5}$	16729
b15-t15	m-m	1420	8401	$7.14 \cdot 10^{-5}$	18114
b16-t16	m-m	1252	6503	$9.23 \cdot 10^{-5}$	20538

Discussion

From the *port-port* experiments conducted on the $60 \times 60 \times 60 \, \text{cm}^3$-block, it becomes evident that the flow and transport behavior is mainly dominated by the particulars of the matrix. The plots shown in Figs. 4.84, 4.86 and 4.87 make it obvious that the flow and transport behavior is dominated by a layer of coarse-grained matrix at the top of the $60 \times 60 \times 60 \, \text{cm}^3$-block and that the fissures have no evident influence on the flow and transport. Further information can be gathered by performing a multivariate statistical evaluation of the experiments (Sect. 10).

4.5 Interpretation of Flow and Transport Experiments Conducted on Laboratory Block

The following section of this chapter focuses on the interpretation of experimental data of the laboratory block by means of numerical modeling and apparent parameters.

4.5.1 Interpretation of Flow and Transport Experiments Based on Apparent Parameters

C. Leven,T. Vogel,V. Lagendijk

To interpret the experiments conducted on the $90 \times 90 \times 80 \, \text{cm}^3$-block and to quantify the relevant parameters, a numerical finite element model was employed (Sect. 2.5.4). Table 4.19 lists the input parameters of the model.

With the numerical model, a standard response for a homogeneous, isotropic block was generated, taking into account the geometry of the block and the spatial position of the ports connected during the experiments.

With a procedure described in McDermott (1999) and Chap. 6, the variation in the hydraulic conductivity of the block is given by a comparison of the flow rates from the experiments and the numerical model. In this interpretation it is assumed that any difference in measured and modeled flow rates can be assigned to the heterogeneous nature of the block since the model solely assumes homogeneity. However, this linear relationship is only valid for DARCY-type flow. Therefore, we will refer to the hydraulic conductivity of the fractured sandstone block in the following as *apparent* hydraulic conductivity K', which is derived from

$$K'_{measure} = K_{model} \frac{Q_{measure}}{Q_{model}} \tag{4.3}$$

with $K'_{measure}$ resulting apparent hydraulic conductivity,
      K_{model} hydraulic conductivity used as model input parameter,
      $Q_{measure}$ flow rate estimated for particular flow experiment,
      Q_{model} flow rate resulting from numerical model.

Table 4.19. Model input parameters to provide a standard flow and transport signal with which the experimental data are compared.

Intrinsic permeability [m^2]	$4.0 \cdot 10^{-14}$
Total porosity [-]	0.15
Longitudinal dispersivity [m]	$6.7 \cdot 10^{-2}$
Transverse dispersivity [m]	$1.3 \cdot 10^{-2}$
Molecular diffusion coefficient [m^2 s^{-1}]	$4.4 \cdot 10^{-6}$

Figure 4.88 shows the distribution of the hydraulic conductivity derived from (4.3) projected on the block faces of sides *II* and *III*. The heterogeneity of the sandstone block can easily be seen, with the highest values near the dominating fractures (e.g. right part of *III* in Fig. 4.88 b). The analysis of the hydraulic conductivity of Figure 4.88 indicates that fracture dominated flow occurs only in cases of direct fracture connections. At connections to the matrix, the influence of the fracture network decreases strongly.

In a quantitative interpretation of the transport experiments, the variation in the transport signal is presented as a percentage of the modelled standard signal.

Figure 4.89 illustrates the comparison of the simulated and measured transport signals for one particular   port-to-port connection. The breakthrough curve represented by a dashed line in Figure 4.89 (a) shows the
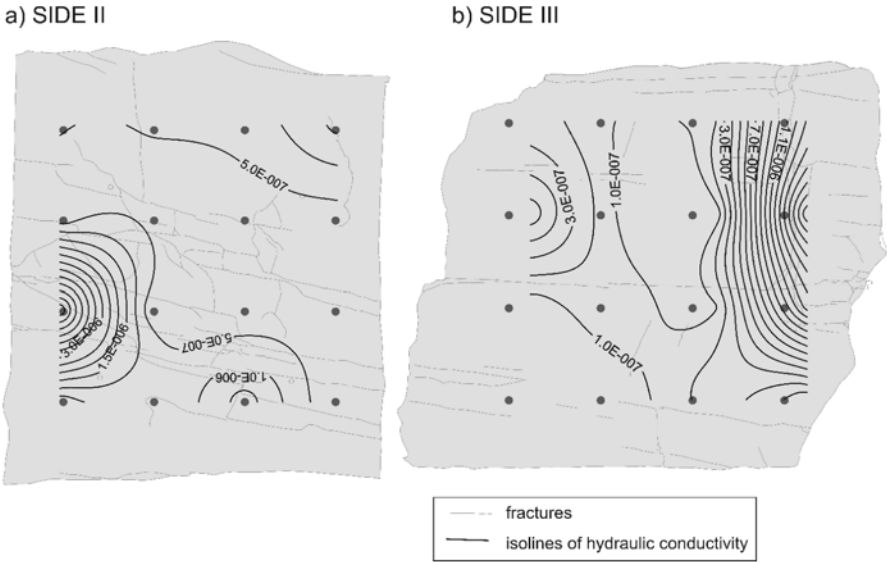
Fig. 4.88. $90 \times 90 \times 80\,\mathrm{cm}^3$-block: Isolines of apparent hydraulic conductivity in (m/s) for side *II* (a) and side *III* (b). The circles indicate the spatial position of the ports.

transport signal which would be recorded for port connection *211-410* if the sandstone block were a homogeneous, isotropic medium with the parameters listed in Table 4.19. The tracer breakthrough in the experiment (solid curve in Fig. 4.89) occurs slightly earlier than in the numerical simulation. This can be due to preferential flow ("channeling"), as is also indicated by the slightly earlier dominant breakthrough time in the experiment. The tailing indicated by the observed transport signal is most likely due to the tracer spreadig more slowly in the sandstone matrix than along the pathways of the fracture network.

Figure 4.90 gives the results of the comparison between the transport signals gained from the simulations of the homogeneous, isotropic medium and the gas-transport experiments. It should be noted that effects due to different boundary conditions are eliminated by comparing each experimental result with the corresponding numerical simulation of the particular *port-port* connection.
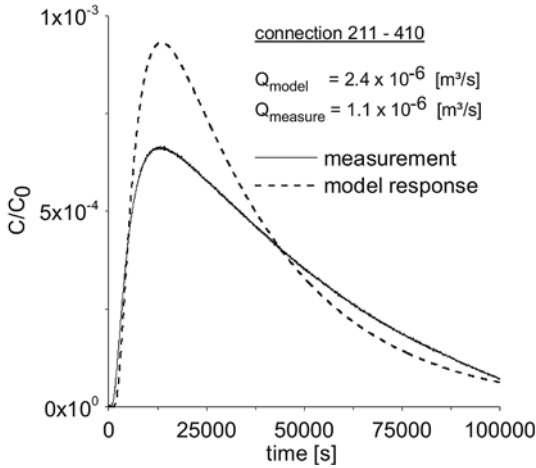
Fig. 4.89. $90 \times 90 \times 80\,\text{cm}^3$-block: Comparison of the breakthrough curves gained from the numerical simulation and from the tracer experiments for the connection between ports 211 and 410. The initial breakthrough time of the numerical simulation occurred after 1380 s, in the experiments it occurred after 950 s.
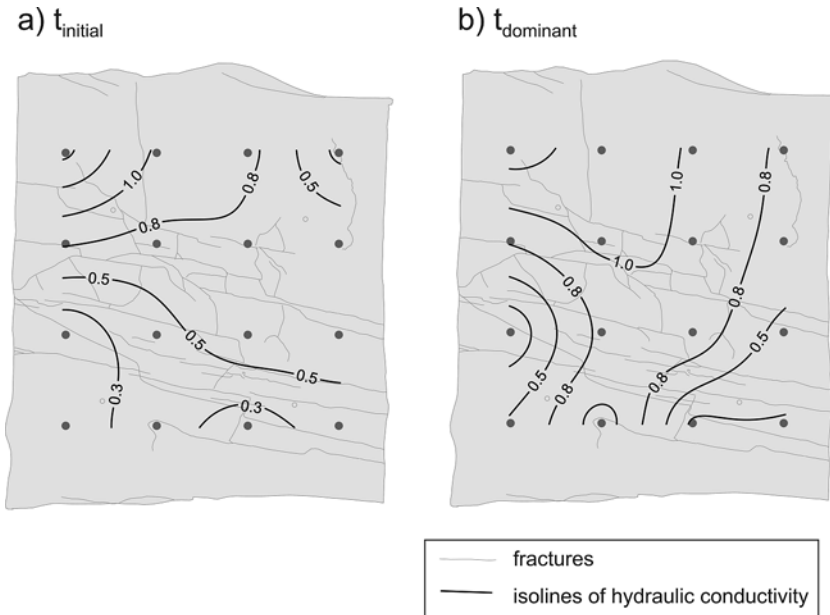

Fig. 4.90. $90 \times 90 \times 80\,\text{cm}^3$-block: Quotient of initial (a) and dominant (b) breakthrough times derived from the experiment and the numerical simulation for a homogeneous, isotropic medium. Values less than one indicate earlier breakthrough times for the experiment than those calculated with the numerical model.

4.5.2 Multi-continuum Modeling: Methodology and Approach

T. Vogel, V. Lagendijk, J. Köngeter

In the following discussion, a brief outline of the approach and methodology used for developing a multi-continuum model is presented, along with the implementation of experimental data in the model.

The following studies carried out on the scale of the $90 \times 90 \times 80\,cm^3$-block, were similar to those conducted on the scale of the cylinder. First, numerical investigations were performed. The parameters were obtained directly from the experiments (Sect. 4.4). For this configuration, the measured concentrations were very low, which caused problems concerning the recovery rate within the experiments.

Figures 4.91 and 4.92 illustrate the simplified block for the FE calculations and the open and filled fractures detected on the block surface. A more detailed description of the different sides of the block can be found in Sect. 4.4. The grid illustrated in Figs. 4.91 and 4.92 corresponds to the measurement port grid. The dimensions of the model block are 0.9 m in the direction of the x- and the z-axes and 0.8 m in the direction of the y-axis, based on the coordinate system as shown.

4.5.2.1 Laboratory-Block Simulations

In the following discussion, the simulations conducted on the bench scale of the $90 \times 90 \times 80\,cm^3$-block are described and the assumptions are explained. The bench-scale block approach differs from the one performed on the cylinder scale as the simulations are based on different sets of data and no discrete model is available. For the numerical investigations, only the data of the tracer experiments between sides II and IV are taken into account as these are the most reliable.

The array of pictures illustrated in Fig. 4.93 within a 4x4 matrix corresponds to side II of the laboratory block. Each picture illustrates the connection between the ports by the intersection of the planes. Tracer is injected at the positions indicated by the black colour. The empty positions within the 4x4 matrix indicate configurations without experimental data.

Figure 4.94 shows the original breakthrough curves and the modified breakthrough curves for two configurations studied. The modified curves have been shifted by the initial value of concentration at the beginning of the measurements (background concentration). The absolute value of the background concentration varies between the experimental configurations and must be taken into account in the interpretation of the data. All of the breakthrough curves in this section have been shifted according to their value of background concentration.
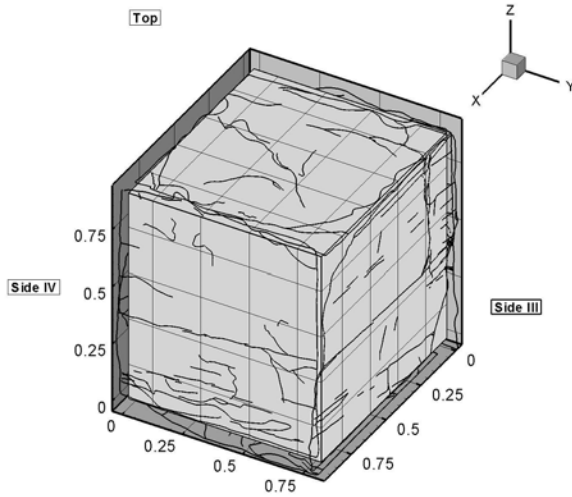
Fig. 4.91. View of the laboratory block from above with a grid of the ports.
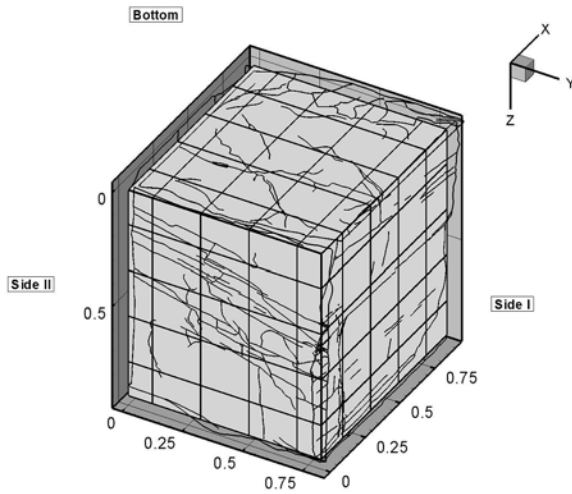

Fig. 4.92. View of the laboratory block from below with a grid of the ports.

4.5.2.2 Determination of Characteristic Model Parameters

The equivalent parameters for the laboratory block can only be determined by analyzing the experimental data because a discrete model of the block
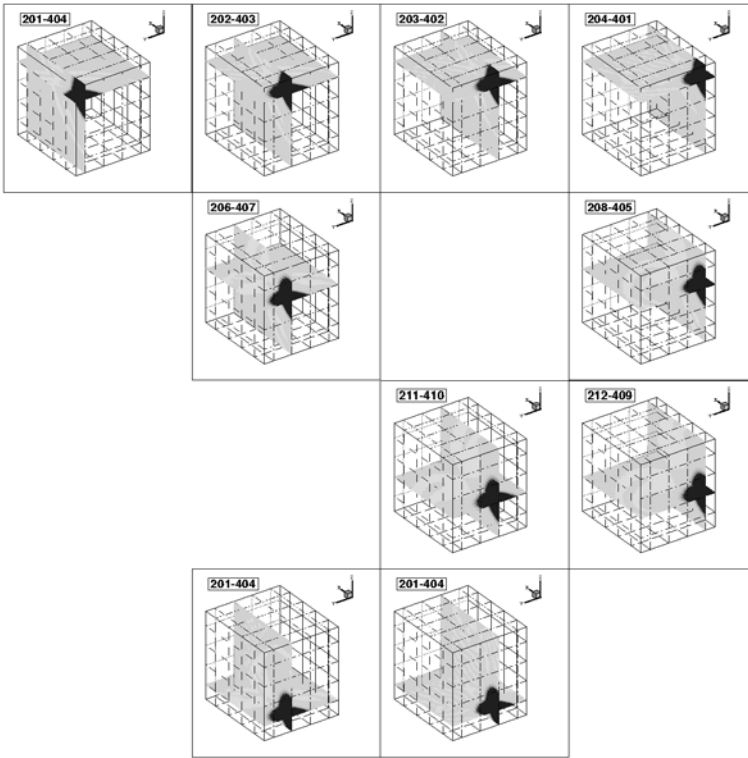
Fig. 4.93. Position of selected ports of sides II and IV.
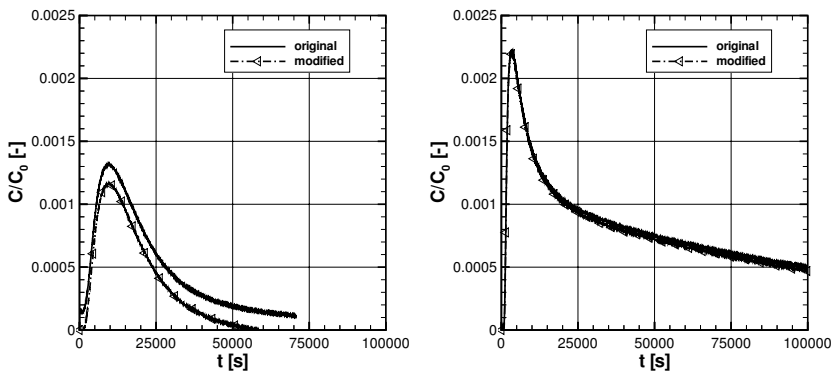

Fig. 4.94. Background concentrations of the experimental data of the laboratory block: Ports 202_403 (left side), Ports 212_409 (right side).

Table 4.20. Characteristic parameters for the single-continuum model.

Equivalent parameters			Continuum
Permeability	k_{xx}	(m^2)	$2.08 \cdot 10^{-12}$
	k_{xy}		0.00
	k_{xz}	(m^2)	0.00
	k_{yy}	(m^2)	$4.37 \cdot 10^{-13}$
	k_{yz}	(m^2)	0.00
	k_{zz}	(m^2)	$7.15 \cdot 10^{-13}$
Porosity	n_e	(-)	0.25
Dispersivity			
-longitudinal	α_l	(m)	$6.67 \cdot 10^{-2}$
-transversal horizontal	α_{th}	(m)	$1.32 \cdot 10^{-2}$
-transversal vertical	α_{tv}	(m)	$1.32 \cdot 10^{-2}$
Molecular			
diffusivity coefficient	D_m	(m^{2}s^{-1})	$4.40 \cdot 10^{-6}$

does not exist. Based on the investigations on the cylinder, a single-continuum model is used.

The equivalent permeabilities are determined by averaging the permeability measurements in the direction of the coordinate axes. The values of porosity, dispersivity and molecular diffusion are taken from McDermott (1999). The parameters are summarized in Table 4.20.

4.5.2.3 Boundary Conditions

A total of 105 ml of tracer is injected into the system. The boundary conditions at the input and output ports are chosen to ensure a constant pressure of 101 300 Pa at the input port, and the experimental flow rate is taken at the output port.

4.5.2.4 Transport Simulation

The results for a representative selection of simulations are illustrated in Fig. 4.95 and Table 4.21. Input and output ports are connected to a fracture, to the matrix or to both. The recovery rates ascertained in experiments and numerical simulations after certain periods of time are also presented in Table 4.21. Some of the experimental rates - time-integrated concentration at the output over infiltrated amount of tracer - are above 100 %. A possible explanation could be the low concentrations detected at the output port, which are of the
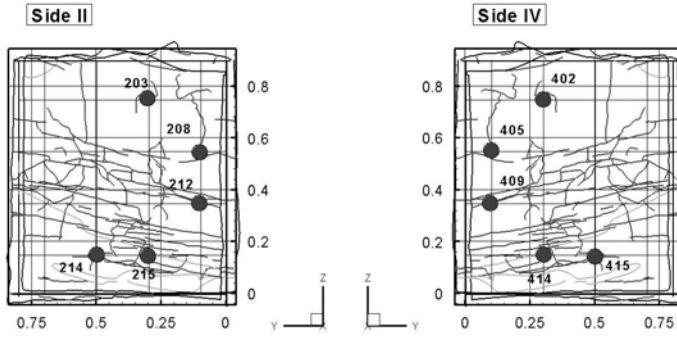
Fig. 4.95. Position of ports for a representative selection of results.

Table 4.21. Ports and recovery rates of representative configurations.

Configuration	Input port	Output port	Rate experiment (%)	Rate model (%)	Time (s)
203_402	Matrix	Fracture	83.53	95.01	$1.50 \cdot 10^{+5}$
208_405	Fracture	Matrix	26.96	79.84	$1.50 \cdot 10^{+5}$
212_409	Fracture	Fracture	113.36	66.56	$1.50 \cdot 10^{+5}$
215_414	Matrix	Matrix	132.58	99.81	$1.50 \cdot 10^{+5}$
214_415	Fracture/Matrix	Fracture/Matrix	111.49	76.93	$7.50 \cdot 10^{+4}$

same order of magnitude as the background concentration (cf. Fig. 4.94). Additionally, it is possible that this effect is due to tracer remaining in the block from a previous experiment.

Figs. 4.96 to 4.98 show that the transport behaviour of the laboratory block may be reproduced qualitatively with the determined equivalent parameters and the chosen model concept. As regards detecting the maximum concentration, the best results are obtained by simulations with matrix ports or mixed ports (215 414 and 214 415). For the model configuration 203 402, where the input port is connected to the matrix and the output is attached to a fracture, the arrival of the maximum relative concentration is too early. On the other hand, for an inverse configuration (208 405), the peak of concentration is predicted too late and the tailing of the breakthrough curve is more distinct. The model underestimates the maximum for configurations with
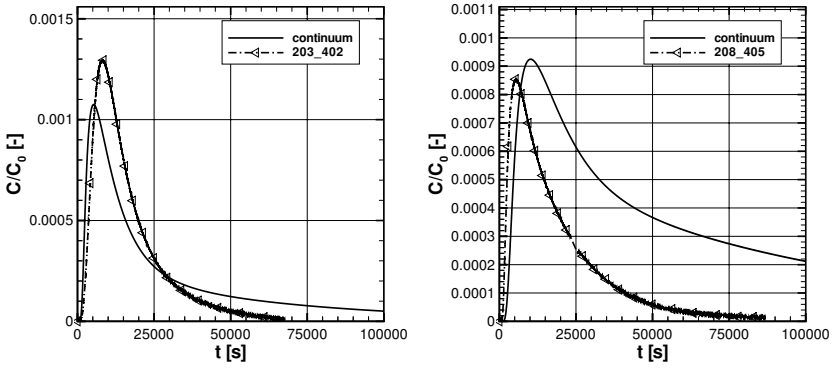
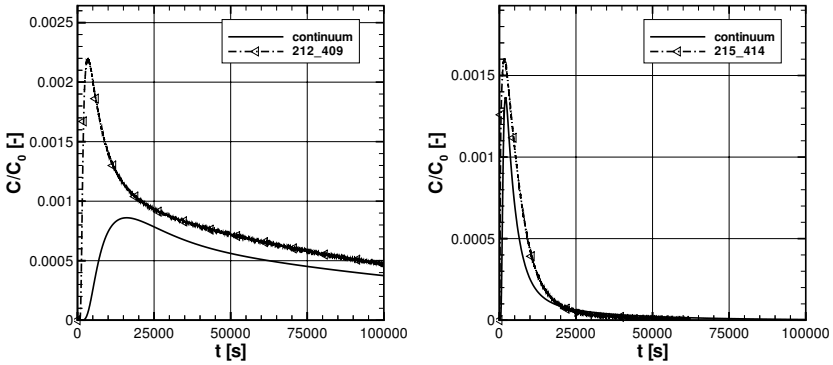**Fig. 4.96.** Breakthrough curves for a pulse injection; ports 203_402 and 208_405.

Fig. 4.97. Breakthrough curves for a pulse injection; ports 212_409 and 215_414.

fracture-fracture connections (212_409) and the recovery rate after 15 000 seconds is low compared to the experimental results.

Thus, it can be shown that the single-continuum model of the laboratory block, with the equivalent parameters determined directly from the experiments, reproduces the transport behaviour well for configurations with significant matrix involvement. For configurations with direct fracture connections, the results underline that there are local effects within the experiment that cannot be represented by a single-continuum model.
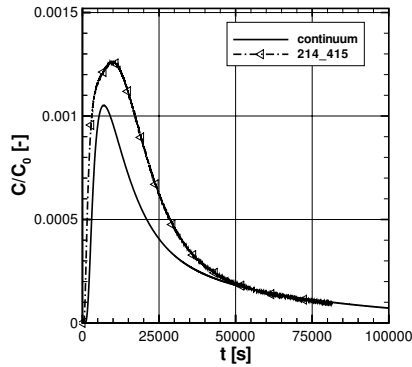
Fig. 4.98. Breakthrough curves for a pulse injection; Ports 214_415.

4.5.2.5 Summary

A continuum model developed for the $90 \times 90 \times 80\,\mathrm{cm}^3$-block on the basis of the experimental data emphasizes the importance of interpreting experimental data in order to ensure the quality of the numerical model.

Configurations that are mainly influenced by the matrix may be modeled qualitatively by applying the equivalent parameters determined directly from experimental data. Simulations of configurations with a direct fracture connection indicate that local effects exist that may not be reproduced by a single-continuum model.